PERMITTIVITY-ENGINEERED TRANSPARENT CONDUCTING TIN OXIDE THIN FILMS: FROM DEPOSITION TO PHOTOVOLTAIC APPLICATIONS

By

James M. Burst

Dissertation

Submitted to the Faculty of the

Graduate School of Vanderbilt University

in partial fulfillment of the requirements

for the degree of

DOCTOR OF PHILOSOPHY

in

Interdisciplinary Materials Science

August, 2010

Nashville, TN

Approved:

Prof. Bridget R. Rogers

Prof. Sharon M. Weiss

Prof. G. Kane Jennings

Prof. Sandra J. Rosenthal

Prof. Timothy A. Gessert

To Jaelyn, Cam and Zoe

ACKNOWLEDGEMENTS

My advisor, Dr. Bridget Rogers, provided years of support, encouragement, mentorship, direction, and a lot of patience. I am grateful to have had the good fortune of being one of her graduate students. She has taught me not only how to approach scientific problems or plot data in meaningful ways, but more importantly she demonstrates what it means to be a good scientist-citizen. My co-advisor, Dr. Sharon Weiss, provided critical input and support to this research: her fantastic balance of encouragement and criticism is much appreciated. Her input has helped transform my results and ideas into coherent manuscripts. I sincerely thank both for being my advisors.

At the National Renewable Energy Laboratory, I worked under the direction of Dr. Xiaonan Li, Dr. Tim Gessert and Dr. Timothy Coutts. I am grateful to Xiaonan for taking me in as a student, helping me develop this project and for letting me have free reign of her equipment. Her expert input and guidance helped this project "see the success." I wish her all the best in her new career.

Dr. Tim Gessert serves as our group manager at NREL, and I am grateful for him serving on this committee. I appreciate Tim's input and accessibility, whether for input on a small problem or helping me see the bigger picture. Tim was intimately involved in developing the "permittivity idea" for this research, together with Dr. Timothy Coutts, Research Fellow at NREL. I thank them both for helping me form the hyothesis, experiments and conclusions in this research. Together they mentored, instructed, criticized, and ultimately provided the encouragement I needed. I especially thank Dr. Coutts for his critical, and humorously pedantic, reading and review of this document.

I also wish to thank Dr. Sandy Rosenthal and Dr. Kane Jennings for serving on my committee. Their questions, suggestions and input during my proposal helped me identify strengths and weaknesses in my research and presentation of results.

No project this big could be done without the help of friends and colleagues. I wish to acknowledge Ben Schmidt, Nirav Vora and Bob Geil (all PhDs now!) for their friendship and support. Together we turned a lot of wrenches in the lab, and those are memories I won't forget. Ben provided me with XPS expertise and long distance technical support; I am fortunate to have had his help and encouragement.

I am fortunate to work with Marty Scott, Master Research Technician at NREL. Marty helped with the nuts and bolts (literally) and support of several tools we used in this research. I thank Dr. Tim Peshek for his friendship and scientific input for the last couple years. I wish him success in his new career. Thank you to Dr. Ina Martin for countless times telling me, "You can do it." I also wish to thank Dr. Teresa Barnes. From my first weeks at NREL, she helped guide me through roadblocks. I also thank her for her input with CVD experiments and research tools.

My graduate school career and interest in experimental research is largely due to Carl Ventrice, my M.S. Physics advisor at UNO. He taught me to machine, weld and understand UHV equipment, surface science and homebrewing. I also thank Dr. R.M.A. Azzam, my M.S. EE advisor, for spurring my interest in ellipsometry. I thank the National Science Foundation and the Department of Energy for financial support.

Lastly, I thank my wife, Jaelyn, for (many!) years of support and love throughout this lengthy career as a student. I couldn't and wouldn't have done it without her.

TABLE OF CONTENTS

LIST OF TABLES

LIST OF FIGURES

CHAPTER I

INTRODUCTION

Transparent conductive oxides (TCOs), a so-called compromise material, find use as an optically transparent electrical contact in a variety of electro-optical systems. This combination of optical transparency and electrical conductivity is required in several applications such as architectural glass with thermal or solar control, flat panel displays, and solar photovoltaic cells. However, TCO films are neither 100% transparent nor is their conductivity as high as "good" metals such as copper or silver. In each of the above applications, a thin solid film of the oxide material is applied, usually to glass, and a compromise between the electrical and optical properties allow a typical visible transmittance of greater than 80% while retaining direct current electrical conductivity on the order of 1-10 $(\mathrm{m}\Omega\cdot\mathrm{cm})^{-1}$. TCOs are used in all thin-film solar cells to admit light and to collect photogenerated charge. For this purpose, they need as high a conductivity as possible while absorbing as little of the incident light as possible. This dissertation focuses on minimizing the deleterious effects of the TCO's losses in a photovoltaic application.

In this first chapter, the objectives and motivation for the current study is discussed in the context of the scope of this dissertation. An overview of the history of and fundamental properties exhibited by transparent conducting oxides (TCOs) is presented. The particular application of TCOs to thin film photovoltaics (PV) is outlined and the issues pertaining to the necessary properties and subsequent materials selection is discussed. Important properties of tin oxide (the host TCO) and zirconium oxide (a means of increasing permittivity) are discussed in detail, with particular emphasis on electro-optical properties, dopant incorporation and the correlation with electronic and crystal structure.

The remainder of this dissertation is outlined as follows. Chapter II discusses details of film synthesis and presents a brief review of chemical vapor deposition (CVD) of tin oxide. The characterization techniques and methods used to evaluate the films in this study are explained in Chapter III. Chapters IV-VI comprise the main findings of this study. Chapter IV presents the key results pertaining to the chemical vapor deposition of tin oxide, zirconium oxide, and tin oxide alloyed with up to approximately ten percent zirconium. In Chapter V, a key discovery in this study is presented, namely evidence for the increase in permittivity due to zirconia addition to tin oxide. Data which indicates that carrier mobility may increase due to permittivity-engineering (via addition of zirconia) is given in Chapter VI, along with arguments to substantiate these findings. The dissertation concludes with a summary of the results that provide some guidance for future research on tin oxide thin films and TCOs in general.

Motivation

A resurgence of interest, and subsequent market expansion, in renewable energy has caused solar energy conversion to become a viable, competitive electricity source. As a consequence of research, consumer demand and political policy, investment in and production of solar PV have seen unprecedented increases in the last several years [1]. While crystalline (*bulk*) Si PV still represents the largest market share, the *thin film* photovoltaics industry is experiencing the highest and most accelerated growth in the solar cell market. Thin film technologies based on amorphous Si (α-Si), microcrystalline Si (μ-Si), Cu(In,Ga)Se_2 (CIGS), or CdTe absorber layers are currently in manufacturing production. Figure 1.1 is a schematic of a typical CdTe-based photovoltaic cell. The TCO provides an electrical contact to the device while allowing photons to pass to the active layers in the cell.

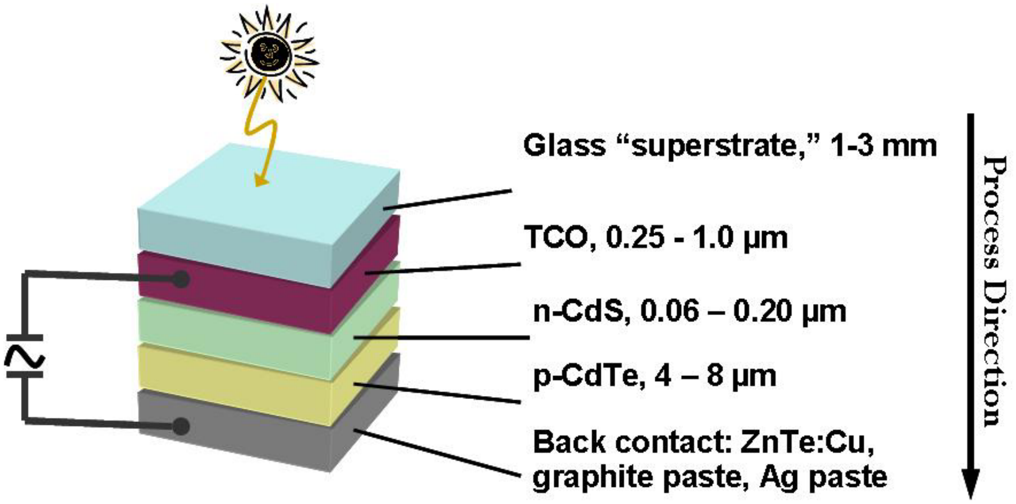

Figure 1.1. Schematic of the "superstrate" configuration for a CdTe PV device, and the corresponding thickness value ranges [2].

This thesis outlines the steps to optimize the optical properties of transparent conducting oxides (TCOs) while maintaining or improving the electrical conductivity, environmental stability and reliability. Gessert, *et al* have recently proposed that increasing the permittivity in indium oxide-based TCOs decreases optical absorption in the IR [3]. This hypothesis is tested for the tin oxide-based TCO system by adding a high permittivity material (ZrO_2) to the SnO_2 host TCO. Using ellipsometry to estimate permittivity and spectrophotometry for optical measurements, the hypothesis that zirconia addition increases the permittivity is tested and it is shown that such addition benefits the optical properties of TCO films.

A low cost, reliable and industrially scaleable method for producing high quality transparent conductive films on glass is crucial to the success of thin film photovoltaics (PV), particularly those based on CdTe/CdS [4, 5]. Low pressure chemical vapor deposition (LP-CVD) meets these requirements. The methods and materials used in this study are consistent with the infrastructure already employed by major glass and coatings manufacturers, as well as for those solar cell companies wishing to process the TCO layer. Fluorine-doped tin oxide (FTO) is the most utilized TCO material (e.g. First Solar, the largest thin film PV manufacturer, uses an industry-standard FTO/glass superstrate). Up to now, the supplied TCO film on glass is not optimized for PV use, rather it has been carried over from that used as architectural glass [6, 7]. Commercial FTO on glass has low electrical resistivity (~ 6×10^{-4} Ω·cm) and has approximately 75-80% optical transmittance in the visible region of the electromagnetic spectrum. However, FTO has low transmission in the near infrared (NIR), which accounts for about 10% loss in current density for a finished cell [5]. Eliminating this loss at low cost could drive down the price-per-watt (or, equivalently, increase the profit potential) for thin film PV because it would lead to a corresponding increase in efficiency and a reduction in price-per-watt. The study uses an interdisciplinary approach, combining both a fundamental consideration and an application-driven perspective, to research the materials science of thin transparent conducting oxide (TCO) films. SnO_2 thin films doped with F and alloyed with ZrO_2 are deposited by LPCVD on glass substrates in a cold-wall reactor. Multiple analysis techniques are used to understand the basic process-property-performance relationships. This fundamental understanding will then lead to the end goals of developing an improved process and ultimately transfer this knowledge to the U.S. PV industry.

TCO-coated glass is used to fabricate α-Si, μ-Si and CdTe based devices with either indium-tin oxide (tin-doped indium oxide, ITO) or fluorine-doped tin oxide (FTO) coated on the starting superstrate. FTO-based materials are more attractive than ITO-based films for several reasons. Tin is 400 times more abundant in the earth's crust than indium (40 ppm and 0.1 ppm respectively), making its availability and cost more stable in the long-term [8]. In addition, the rapid expansion in flat panel display production, which currently uses ITO exclusively, has dramatically driven up indium costs. Therefore, a PV technology with a Sn-based TCO would be more attractive from a cost-of-manufacturing and raw material point of view.

Most thin film PV manufacturers purchase their superstrate glass with the transparent conductive coating already applied by the glass producer. Tin oxide is typically applied by chemical vapor deposition (CVD) while the glass is still hot from the float glass process [7]. The resulting film has low resistivity, high visible wavelength transmission, and typically low transmission in the infrared. The IR absorption and reflection in these films is due to the interaction of the free-carriers with light and it accounts an approximate 10% current density loss in a CdTe PV cell [5]. A TCO that increases IR transmission would potentially increase the PV cell current density (J_{sc}) resulting in a finished module with overall higher efficiency and a reduction in levelized cost of electricity.

Project Objectives

A primary objective of this work is to investigate the hypothesis that increasing the permittivity of a TCO decreases its absorption in the near-infrared. As stated previously, increased transmission in the near-infrared is likely to lead to more efficient solar PV cells. A high permittivity material (ZrO_2) is alloyed with the host TCO, SnO_2 to test this hypothesis. The effects of adding up to approximately 30% ZrO_2 into SnO_2 and SnO_2:F on the electrical and optical properties of the films is presented in detail. Films are synthesized by low pressure chemical vapor deposition. The ZrO_2-SnO_2 alloy is a promising system with respect to structure, oxidation state and chemical stability of the individual component cations and their oxides. Tin oxide condenses in the tetragonal (rutile) structure; zirconium oxide thin films can be monoclinic or tetragonal under certain conditions [8, 9]. Both cations are in the 4^+ state. Therefore, these experiments directly probe the effect of the addition of zirconia on permittivity without any expected addition of free carriers (as would be the case for an aliovalent cation). The ionic radius for zirconia is 0.072 nm (sixfold-coordinated) which is slightly larger than that for tin oxide at 0.069 nm [10]. Both oxide systems are chemically and environmentally stable, with respect to the conditions typical for PV use [11-13]. Since the bandgap for ZrO_2 (5.8eV) is much larger than for tin oxide (3.6-3.8 eV), the studies focus on the films with 0-10% Zr (at.%) in order to maintain conductivity (i.e. the donor energy level, E_D remains close to conduction band minimum, CBM). Fluorine incorporation into ZrO_2 is investigated and relationships to the effects of film deposition, structure, optical properties and film morphology are presented.

The targeted criteria outlined in Table 1.1 are considered in designing the experiments. Film thicknesses are targeted to be on the order of 350-600 nm based on published figures and previous experience [5, 14]. To separate the effects of differences in carrier concentration and thickness, parameters are sought such that a direct comparison of the NIR response of films with varying Zr:Sn concentration, but comparably similar physical thickness and charge carrier concentrations, is carried out.

CVD processes are developed to simultaneously deposit both ZrO_2 and SnO_2 under similar conditions. The materials properties of the component systems and of the mixed oxide system are characterized, and their electrical and optical performance is measured. The fundamental aspects that determine these properties such as structure, electronic transport and permittivity are investigated.

The following objectives are addressed in this dissertation:

i) Deposition of films

  a) Optically transparent films of ZrO_2, ZrO_2:F, and conductive SnO_2:F

  b) Transparent conductive SnO_2:F films containing ZrO_2

ii) Systematic study of the materials properties and reliability of films containing ZrO_2

iii) Development of permittivity-engineered TCO films: electrical and optical properties as a function of Zr%

Thin Film Photovoltaics: Issues for Transparent Electrodes

The top electrical contact for thin film solar cells is a TCO. This electrode must combine the unusual properties of metallic-like electrical conductivity with transparency across the solar spectrum. These requirements are especially of interest in that optimizing one of them typically degrades the other. This tradeoff between enhancing the optical or electrical properties is weighed by a figure of merit, FOM_{TCO},

$$FOM_{TCO} = \frac{T^{10}}{R_S} \tag{1.1}$$

where T is the average transmittance for the region of interest (360-860 nm for CdTe, 360-1100 nm for Si), and R_S is the sheet resistance [15]. Note: in the literature, T is sometimes chosen at a particular wavelength, say 500 nm. The film must also be compatible with subsequent processing conditions. Additional constraints are more subtle. The TCO material must be chemically inert with materials that it contacts (e.g. soda lime glass, CdS). These properties must be stable over long time frames and must not be degraded with thermal or moisture stresses. Table 1.1 summarizes these properties along with desired benchmark figures.

Table 1.1. Desired criteria for TCOs for use in thin film CdTe PV cells [16].

Sheet Resistance	**Optical Bandgap**	**Visible Transmittance**	**CdS Interface**	**Reliability**	FOM_{TCO}
≤ 15 Ω/□	> 3 eV	> 80%	Insulating, chemically robust	> 25 years	$\geq 5\times10^{-3}$

Overview of Transparent Conducting Oxides

Metal oxides that are both optically transparent and electrically conductive have been realized for some 100 years. The first recorded instance being that of Badecker's report that evaporation-deposited cadmium films became transparent once thermally oxidized [17]. Coatings based on tin oxide and, a few years later, indium oxide, have been used commercially for decades, beginning with military applications in WWII. Together with zinc oxide, these films are utilized in various applications: electrochromic, electroluminescent and liquid crystal displays; window coatings on buildings and aircraft; molecular electronics; and thin film photovoltaics [7, 8, 18].

Most TCOs are n-type wide-bandgap semiconductors, with intrinsic doping due to non-stoichiometric compositions. This intrinsic doping may be due to donor centers or impurity states attributed to oxygen vacancies, H^+ bound on O^- sites, and/or cation interstitials [8, 19-21]. In the case of tin oxide, the conductivity of unintentionally doped materials is argued to be due to the dual valence of tin, Sn^{2+} and Sn^{4+}, easily forming SnO complexes in the SnO_2 lattice [22]. In practice, TCOs are degenerately doped, that is, the Fermi level is in the conduction band. Fluorine and antimony are the familiar anionic and cationic dopants, respectively, in tin oxide, with F-doping yielding the best results [8]. In general, increasing the electrical conductivity via charge carrier concentration (through heavy doping) blue shifts the optical transmittance window, as explained by Burstein and Moss [23, 24]. The increase in carrier concentration, and subsequently the bandgap widening, via conduction band filling may be beneficial in some instances[14]. The carrier concentration also affects the optical properties at longer wavelengths. Absorption and reflection due to free carriers may further reduce transmission in the near infrared by decreasing the free carrier plasma absorption wavelength; this is further compounded by potentially decreased mobility due to impurity scattering.

Tin oxide crystallizes in the tetragonal (rutile) structure, with a unit cell consisting of four oxygen atoms and two tin atoms with a volume of 7.16 x 10^{-2} nm^3, and corresponding lattice parameters a = 0.474 nm and c = 0.319 nm (c/a = 0.673, atomic density is 8.37 x 10^{22} $atoms/cm^3$). The oxygen atoms are three-fold coordinated, while the tin atoms are octahedrally coordinated to the neighboring oxygen atoms. With the exception of zinc oxide, in which Zn is tetrahedrally bound, all other n-type TCOs (i.e. those based on In_2O_3, Cd_2SnO_4, CdO) exhibit this octahedral coordination of cations to oxygen [25].

Electrical Properties of TCOs

The lowest resistivity values reported for TCO films are typically on the order of 10^{-4} Ω·cm. This is two orders of magnitude higher than the resistivity of some metals such as aluminum or copper (2.7×10^{-6} Ω·cm and 1.7×10^{-6} Ω·cm, respectively). Note, however, that the resistivity values for TCOs are 14-20 orders of magnitude less than that of typical insulators. Since most TCO films (and all in the current study) are n-type, all relations to charge and charge carriers are taken to be that of electrons (e and n, respectively). Similar arguments may be made for p-type material. Recalling that the (D.C.) conductivity, σ, is the reciprocal of resistivity, ρ, the definition of conductivity is given by the classical Drude free electron theory by its proportionality to the relation between the current density J induced in the presence of an electric field E [26]:

$$J = \sigma E \ . \tag{1.2}$$

The current quantifies the motion of electrons and the term drift is given to describe the motion of electrons in the direction of the electric field, where their velocity is in turn called the drift velocity, v_D [25]. For a given electron carrier concentration, n, the current density is

$$J = nev_D, \tag{1.3}$$

and solving (1.2) and (1.3) for drift velocity,

$$v_D = \left(\frac{\sigma}{ne}\right)E. \tag{1.4}$$

The proportionality factor is equal to the electron mobility as

$$\mu = \frac{\sigma}{ne}. \tag{1.5}$$

The mobility is related to two fundamental materials properties by

$$\mu = \frac{e\tau}{m*} \tag{1.6}$$

where τ and $m*$ are the relaxation time and effective mass, respectively. The relaxation time is actually the mean time between random scattering events (carrier collisions) [25, 27]. From (1.5) it is evident that to increase the conductivity, either the mobility or concentration of electrons, or both, must be increased. In order for mobility to increase, the scattering time must increase or the effective mass decrease. In general, but with exceptions, the effective mass is considered to be a constant property for a given host TCO material, while the scattering time may be a function of material quality or doping effects [27-30]. The figure of merit given in (1.1) is often chosen for TCOs for PV applications because it weighs heavily the transmittance [15]. However, because the sheet resistance is thickness dependent so is the figure of merit. Other authors have used a figure of merit to compare TCO performance which is not thickness dependent, namely

$$FOM'_{TCO} = \frac{\sigma}{\alpha} \tag{1.7}$$

which is the conductivity divided by the absorption coefficient. Coutts *et al* [27] have shown that since

$$\sigma \propto \tau \text{ and } \alpha \propto \tau^{-1}, \tag{1.8}$$

this figure of merit is particularly illustrative when written as

$$FOM'_{TCO} \propto \tau^2 \text{ or } FOM'_{TCO} \propto \mu^2. \tag{1.9}$$

The importance of increasing mobility is clearly seen in (1.9): it directly shows that increasing mobility necessarily improves both the electrical and optical properties of a TCO (by decreasing resistivity and absorption, respectively).

The effective mass is described by quantum mechanics in its relation to band structure. The band structure of a TCO gives keen insight into its electrical and optical properties. The one-dimensional equation for effective mass is related to the curvature of an isotropic band by

$$\frac{1}{m^*} \equiv \frac{1}{\hbar^2}\frac{d^2E}{dk^2} \tag{1.10}$$

where E is the energy of the band, $\hbar$ is Plank's constant, $h/2\pi$, and k is the band momentum [26]. From (1.10) it is seen that a highly disperse conduction band, for example, will have a tight curvature which gives rise to a small effective electron mass.

Freeman *et* al calculated the band structure for SnO_2 and for the point defects of oxygen vacancies or tin interstitials and is reproduced in Figure 1.2 [31]. The main features, which are relevant for the common n-type TCOs are: a relatively flat and non-disperse valence band made up primarily of O-2p states; the valence band maximum (VBM) and conduction band minimum (CBM) occur at the gamma-point (k=0, reciprocal space) and the energy gap between them is larger than 3.0 eV so that direct optical transitions occur outside of the visible spectrum; the CBM is highly dispersed and the gap between the CBM and the next conduction band is also larger than 3.0 eV, again ensuring that no electron transitions occur in the visible range of wavelengths.

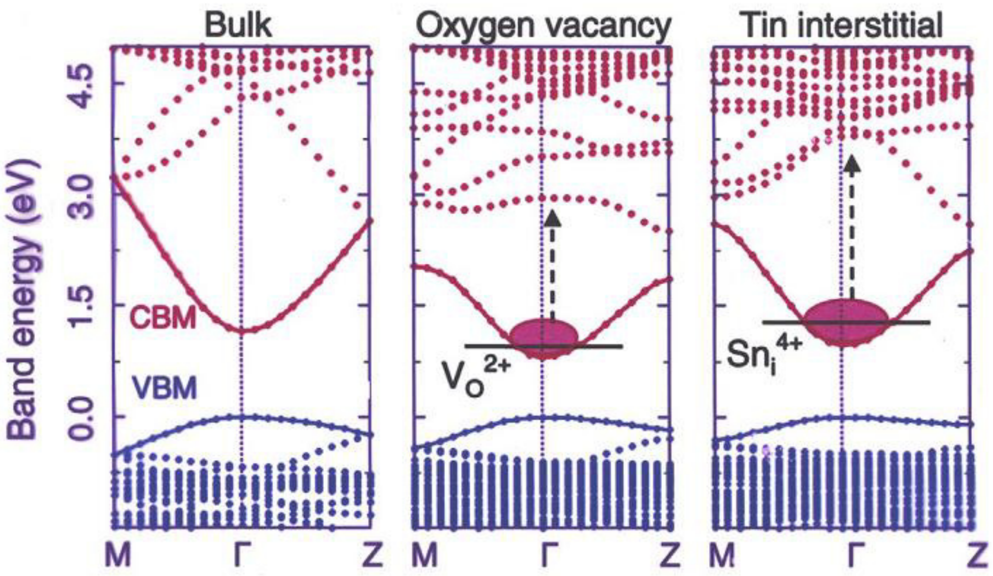

Figure 1.2. Calculated band structure for tin oxide for the cases of (left) stoichiometric, (b) oxygen vacancies and (c) tin occupying interstitial sites [31]. The higher energy conduction bands (dots) above the conduction band minimum (solid) line are separated from the CBM by energies outside of the visible region.

The darkened regions at the CBM for the two defect cases represent impurity bands which exist near, at or in the conduction band. These bands are essentially the free carriers due to the impurities and their occurrence near the CBM is indicative of degeneracy, which occurs when the Fermi level is within 3kT of the CBM. The condition for degeneracy is fulfilled for carrier concentration values at or greater than the critical Mott concentration, n_{Mott}, at which point the impurity levels overlap with the conduction band forming the aforementioned impurity band [29]. The critical Mott concentration is estimated by

$$n_{Mott} = \frac{0.2}{a_{imp}}, \text{ where } a_{imp} = \frac{\varepsilon_r}{m^*/m_0} \frac{a_0}{\Delta Z} \tag{1.11}$$

where a_{imp} is the hydrogenic orbital size for the impurity; ε_r is the relative permittivity of the host; m^* is the effective mass; m_0 is the mass of a free electron; a_0 is the Bohr radius; and ΔZ is the difference in valency between the impurity ion and host ion it replaces [30, 32]. By example, for fluorine-doped tin oxide, F^- substiutes O^{2-}, so $\Delta Z = 1$ and we take $\varepsilon_r = 10$, which gives a critical concentration of 1.46×10^{18} cm^{-3}. Nearly all of the F-doped samples in the current study have carrier concentration greater than 10^{19} cm^{-3} indicating that these films are highly degenerate.

A diagram of the band filling mechanism due to impurity addition (point defects or extrinsic dopants) is shown in Figure 1.3. The dispersion of the conduction band is associated with a relatively small effective mass for electrons. The consequence is that the fundamental bandgap then becomes larger as the conduction band fills (as carrier concentration increases). In Figure 1.3, the increase in bandgap energy, ΔE_G is known as the Burstein-Moss shift, which correlates the blue-shift of the optical absorption band edge in the near ultraviolet with carrier concentration [23, 24].

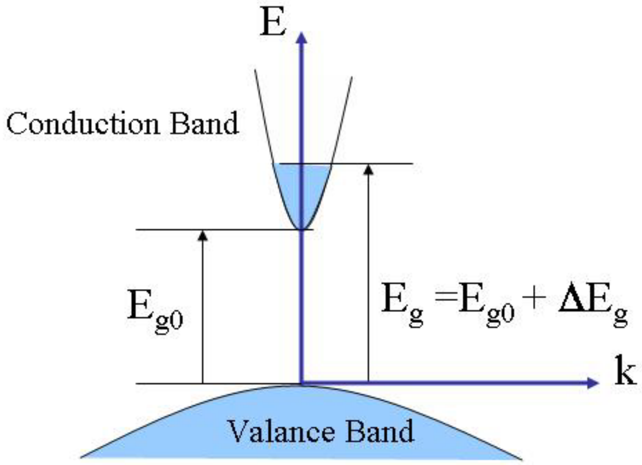

Figure 1.3. Energy band diagram depicting the fundamental bandgap, E_{G0}; the (measured) optical bandgap, E_G; and the change in bandgap energy, ΔE_G due to band filling. This phenomenon of bandgap widening due to conduction band filling is termed the Burstein-Moss shift [23, 24, 27].

Optical Properties of TCOs

The optical properties of transparent conducting films, while intimately tied to the electrical properties, essentially dictate how much light can pass through to the underlying layers (e.g. the photoabsorbing layers in a PV device). Therefore, critical evaluation of the optical properties is essential. In particular, tuning the infrared transparency in TCO films is particularly of interest for certain applications.

The TCO film may be considered as a pass band filter for electromagnetic radiation. For a given application, then, one attempts to tune the pass band to best match the spectral region of interest. For example, in solar or thermal control coatings, the pass band might ideally be only the visible region, with a desired sharp onset of high reflectance for longer wavelengths (infrared) and nearly complete absorption in the ultraviolet (UV). In flat panel displays, the operation can be simplified as electrons in – photons out. Again, only the visible region is of interest for transparency. However, in PV devices, the pass band is optimized by a convolution of the solar spectrum and the quantum efficiency response (the region of solar photo-absorption) for the particular PV technology. For example, CdTe (bandgap = 1.44 eV) absorbs strongly in the wavelength range of 360 – 860 nm, while Cu(In,Ga)SSe (CIGS) absorbs further into the near IR up to ~ 1100 nm. Absorbers based on amorphous or microcrystalline Si (α-Si and μ-Si, respectively), and tandem stacks may have appreciable absorption efficiencies extending to ~ 1800 nm in the NIR.

A typical set of experimental optical response data are presented in Figure 1.4. Shown are the transmittance, reflectance and absorptance (%T, %R, %A, respectively). A characteristic high transmittance (generally > 80%) is observed in the visible region (~ 380-700 nm). The oscillations in the transmittance and reflectance spectra are due to interference effects from the front and rear surfaces of thin films (TCO film thickness ~ 350 nm). The strong absorptance, and corresponding transmittance cutoff, at shorter wavelengths is characteristic of interband transitions. Electrons are photo-excited from the valence band to the conduction band for energies greater than the bandgap energy (typically greater than 3 eV for TCOs). The decreased transmittance at longer wavelengths is due to an increase in absorptance and in reflectance. Note that the absorption is centered about a point near the plasma wavelength, but the peak is quite broad and extends into the visible region thus attenuating the transmittance and reducing cell performance.

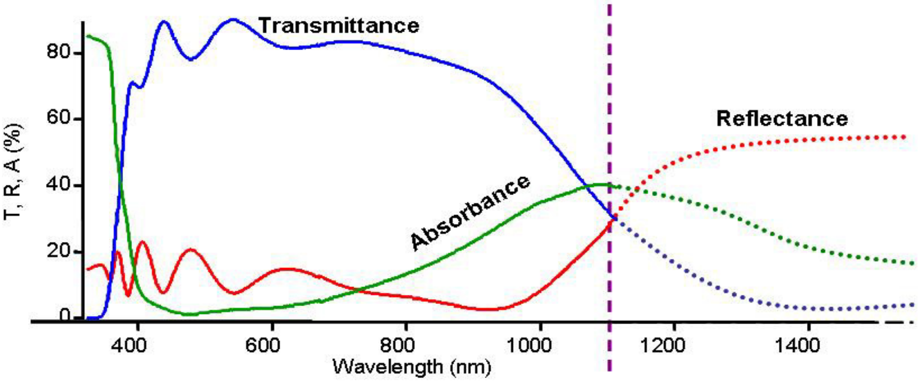

Figure 1.4. Characteristic transmission, reflection and absorption spectra for a TCO film. The vertical dashed line near 1100 nm marks an approximate location for the plasma edge. The data are obtained from spectrophotometry measurements.

Relating the Optical and Electrical Functions

The Drude oscillator model for free electrons is a simplification of the Lorentz oscillator (which describes "bound" electrons via a restoring force). In either case, the equations of motion for the electrons are described by a harmonic oscillator: electrons (with a relatively lower mass) are attached by a "spring" to the ion core (a heavier mass). Because the electrons are free to move about the lattice, there is no associated restoring force in the Drude model (i.e. the resonance frequency, $\omega_0^2 = k/m = 0$). Following the description of Wooten, the equation of motion of free electrons is similar to that of a damped harmonic oscillator and is given by

$$m\frac{\partial^2\vec{r}(t)}{\partial t^2}+m\Gamma\frac{\partial\vec{r}(t)}{\partial t}=-e\vec{E}(t) \tag{1.12}$$

where *m* is mass, $\vec{r}(t)$ is the position vector, *t* is time, *Γ* is the damping term, and $\vec{E}$ *(t)* is the energy [33]. The solution is

$$\vec{r}=\frac{e}{m}\frac{\vec{E}(\omega)}{\left(\omega^2+i\Gamma\omega\right)} \tag{1.13}$$

and the susceptibility, *χ(ω)*, which is a measure of polarizability in response to an electric field, is given by

$$\chi(\omega)=-\frac{\omega_p^2}{\omega^2+i\Gamma\omega} \tag{1.14}$$

where the plasma frequency (wavelength) is

$$\omega_P{}^2=\frac{ne^2}{\varepsilon_\infty\varepsilon_0 m^*},\ \left(\lambda_p=2\pi\cdot c\sqrt{\frac{\varepsilon_0\varepsilon_\infty m^*}{ne^2}}\right) \tag{1.15}$$

where ε_∞ and ε_0 are the high-frequency permittivity and free-space permittivity, respectively [33]. For a free electron material, the damping term *Γ* is the electron collision rate, which is the inverse of the mean electron collision time, τ (i.e. $\Gamma = \tau^{-1}$). Since the susceptibility, *χ(ω)*, is related to the complex permittivity function by

$$\tilde{\varepsilon}(\omega)=\varepsilon_1+i\varepsilon_2=1+\chi(\omega) \tag{1.16}$$

equations (1.14) and (1.15) can be rewritten (assuming $\omega\tau^2$ » 1, see below) in terms of the real and complex parts of the permittivity as given by Maxwell's equations

$$\varepsilon_1(\omega)=\varepsilon_\infty-\frac{ne^2}{\varepsilon_0 m^*\omega^2} \tag{1.17}$$

$$\varepsilon_2(\omega) = \frac{ne^2}{\varepsilon_0 m^* \omega^3 \tau} \tag{1.18}$$

respectively [26, 33, 34].

The time between collisions in metals and TCOs is relatively brief, on the order of tens of femtoseconds. However, compared to optical frequencies (e.g. for $\lambda = 500$ nm, $\omega = 2\pi c/\lambda = 3.7\text{x}10^{15}$ rad/s), $\omega\tau^2$ » 1 [33]. This approximation was already applied to (1.17) and (1.18). The permittivity equations can be written in terms of the plasma frequency as

$$\varepsilon_1(\omega) = \varepsilon_\infty \left[1 - \frac{\omega_p^2}{\omega^2} \right] \tag{1.19}$$

$$\varepsilon_2(\omega) = \varepsilon_\infty \frac{\omega_p^2}{\omega^3 \tau} \tag{1.20}$$

According to Hamberg, the aforementioned approximation may break down in the infrared spectral region since damping may be significant [28]. Note that damping is also in the imaginary part of $\varepsilon(\omega)$ in (1.20).

The permittivity is related to the optical constants by

$$\tilde{\varepsilon} = \varepsilon_1 + i\varepsilon_2 = \tilde{n}^2 = (N + i\,k)^2 \tag{1.21}$$

where $\tilde{n}$, N and k are the complex, real and imaginary parts of the refractive index, respectively. Again, it is noted that the plasma frequency is defined by the frequency at which $\varepsilon_1 = 0$, or equivalently at $N = k$. The Fresnel equations predict the fraction of light reflected (or transmitted) when light is incident on media having interfaces with differing refractive indices. For light incident at near-normal angles at a film-glass substrate structure, the equation for the power reflectance is given by its relation to the refractive indices by

$$R = \frac{(N_F - N_S)^2 + k_F^2}{(N_F + N_S)^2 + k_F^2} \tag{1.22}$$

here N_F, N_S are the real part of the refractive index for the film and substrate, respectively; k_F is the extinction coefficient of the film [35]. The index of air is taken to be unity with an extinction coefficient of zero for air and substrate.

It is instructive to consider the spectral dependence of $\varepsilon(\omega)$, $n(\omega)$, and $R(\omega)$. For the limiting case of no damping: $N = 0$ and $R = 1$ for $0 < \omega < \omega_P$. Above ω_p, k is zero and the reflectance decreases as N increases from zero to unity [33]. A steep reflectance edge near the plasma frequency can be expected as the dominant spectral feature in the optical properties of metals [33]. Hamberg calculated the permittivity functions and compared them to experimental values for ITO films with $n = 6.2 \cdot 10^{20}$ cm^{-3}; the data are shown in Figure 1.5 [28]. O'Neil *et al* used a Drude-Lorentz oscillaror to model the complex refractive indices of ITO using a carrier density of $4 \cdot 10^{20}$ cm^{-3}, which is approximately two-thirds the carriers for Hamberg's films (Figure 1.6) [36]. The difference in carrier density is clearly observed in the plasma edge: $\lambda_P = 1.7$ µm for the lower carrier density film, whereas $\lambda_P \approx 1.5$ µm for the higher carrier density film. These results are exactly what is predicted by the Drude model.

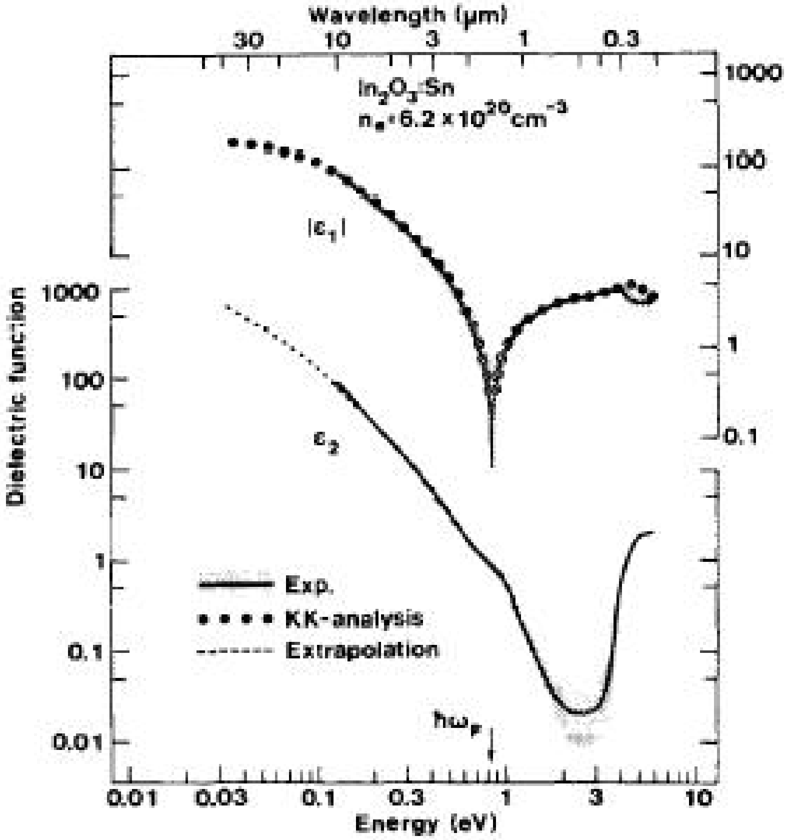

Figure 1.5. The experimental and predicted permittivity functions ITO [28].

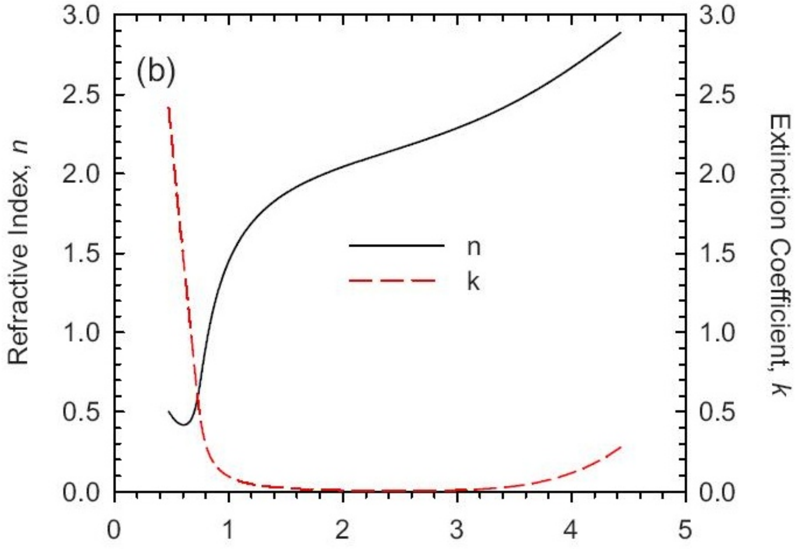

Figure 1.6. The modeled complex indices of refraction for ITO [36].

To recap, the Drude theory of free electrons in metals can accurately describe the optical and electronic properties and their interrelationships of TCOs and is used in developing the hypothesis of the proposed work [27]. The Drude model is a simple one so a physicist should not expect it to perfectly model real systems [37]. The reason it works is that we are dealing with electrons of only a single energy, ie., the Fermi electrons. Such treatment would not be applicable if the materials were not degenerate.

A typical TCO film transmits light at wavelengths between 350-1500nm. The short wavelength absorption is centered at the optical bandgap, λ_g,and is a consequence of exciting electrons from the valence band to the conduction band. The decreased transmission at longer wavelengths, in the visible and IR, is due to absorption and reflection losses. These losses are due to free carriers interacting with incident electromagnetic radiation, and are centered about the plasma wavelength, λ_p (plasma frequency, $\omega_p = 2\pi \cdot c / \lambda_p$). We have stated that there is a trade-off between increasing the conductivity and increasing the transmittance. The basic trend is that increasing charge carrier concentration increases the absorption due to free carriers and shifts the plasma absorption to higher frequencies (shorter wavelengths). In contrast, *increasing* carrier mobility does not shift the plasma frequency, but instead *decreases* the absorption intensity. This is shown pictorially in Figure 1.7, reproduced from Coutts [27] and is exactly in agreement with expectations given by the figure of merit in (1.9).

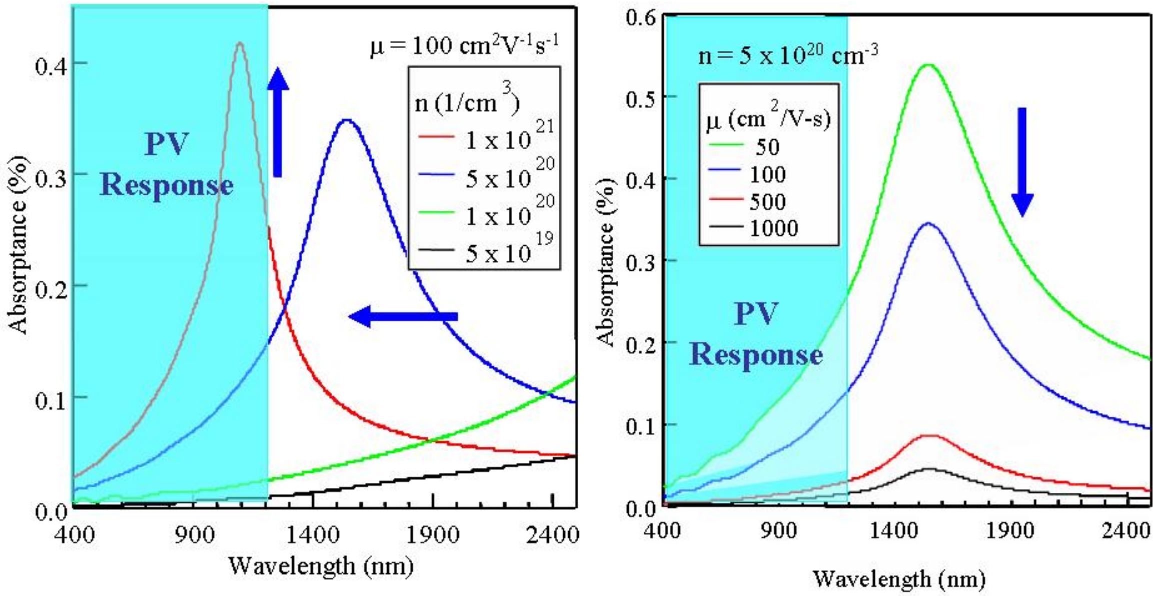

Figure 1.7. (left) The calculated increase in absorptance in the NIR due to increasing carrier concentration at a fixed mobility value, (right) the decrease in absorptance height with increasing mobility at a fixed carrier density [27].

From (1.15), we observe that an increase in the high-frequency permittivity should increase the plasma wavelength. Recently Gessert and Coutts of NREL have developed this idea of increasing permittivity to decrease absorption in TCOs. Surprisingly, this has not been previously addressed in the TCO literature [3].

Literature Review of Zr-added TCO Materials

Many dopants and mixed oxides have been studied including oxides of cadmium, indium, titanium and to a lesser extent zirconium [14, 38-40]. Qadri *et al* have reported on pulsed laser-deposited ZrO_2- mixed oxides of In_2O_3, SnO_2 and ZnO [39]. The reported resistivity values for SnO_2-based films were on the order of 10^{-2} Ω-cm, about 2 orders too high for PV use. The only optical transmittance data these authors report was for 5% ZrO_2 ($R_S = 1799\ \Omega/\square$). No comparison is made to an undoped sample, and there is no reference to the IR absorption edge. To date, there is no report in the literature of enhanced optical properties of SnO_2-based TCOs by zirconia addition (i.e. enhancement via increased permittivity).

Several studies, outside of NREL work, on Zr-doped indium oxide (IO), indium-tin-oxide (ITO) and zinc oxide have been reported [38, 39, 41-46]. In all cases the addition of aliovalent Zr^{4+} is justifiably considered as contributing to the electronic charge carrier concentration, and little is mentioned of a change in optical properties. In particular, there is no attention paid to permittivity affects. The motivation for these studies is to increase the chemical resistance of the host TCO through zirconia addition: however, no testing of this was reported. Interestingly, however, Campet *et al* have reported that Zr-doped IO and ITO ceramics (not films) have decreased *visible* absorption and exhibit higher mobilities when compared to the undoped IO ceramic [38]. The authors attribute this to the higher "Lewis acid strength" of ZrO_2 compared to the host material. These differences can be, at least partially, explained by the differences in charge carrier concentration in their bulk ceramics. Also, no mention of differences in crystallinity or grain size is given. Recently, Gessert *et al* found that additions of Zr in In_2O_3 and ITO sputter targets allowed for a broader window of acceptable oxygen partial pressure during sputter deposition; indeed, they report improved optical transmittance due to the measured permittivity by adding zirconia [47, 48].

The materials properties of the SnO_2-ZrO_2 system has been studied for bulk ceramics [49-52] and thin films [40, 53]. For the bulk ceramics, a miscibility gap is reported in all cases: a maximum of ~20 mol% SnO_2 can be incorporated in ZrO_2, and ~25 mol% ZrO_2 into SnO_2 to form solid solutions or alloys. The applications for these studies are in densification of ceramics, high temperature materials, protective coatings and also in studying the oxidation of the tin-zirconium alloy, Zircalloy. A miscibility gap in the mixed oxide thin films has not been explored. Fang *et al* have reported enhanced gas sensing and wider operating temperature range with 1 mol% ZrO_2 addition into SnO_2 films formed by spin coating [53]. Qadri *et al* reported on the crystallographic phases of e-beam deposited ZrO_2-SnO_2 [40]. For small SnO_2 additions, the monoclinic phase of zirconia is maintained. Interestingly, however, they observe a partial stabilization of the cubic zirconia phase for ZrO_2 films with 3-6 wt.% SnO_2.

References

1. Resch, R., *No Question of Solar Momentum in U.S.*, in *Semiconductor International*. 2008. p. 116.

2. Rose, D.H., F.S. Hasoon, R.G. Dhere, D.S. Albin, R.M. Ribelin, X.S. Li, Y. Mahathongdy, T.A. Gessert, and P. Sheldon, *Fabrication Procedures and Process Sensitivities for CdS/CdTe Solar Cells.* Progress in Photovoltaics, 1999. **7**(5): p. 331-340.

3. Gessert, T.A. and T.J. Coutts, *Transparent Conducting Oxides and Production Thereof*, U.S. Patent, Editor. 2007, NREL: U.S.A.

4. Alamri, S.N. and A.W. Brinkman, *The Effect of the Transparent Conductive Oxide on the Performance of Thin Film CdS/CdTe Solar Cells.* Journal of Physics D-Applied Physics, 2000. **33**(1): p. L1-L4.

5. Li, X., J. Penkow, B. To, and T. Gessert, *Comparison between Research-Grade and Commercially Available SnO_2 for Thin-Film CdTe Solar Cells*, in *33rd IEEE Photovoltaics Specialists Conference,*. 2008: San Diego, CA.

6. Noufi, R. and K. Zweibel. *High-Efficiency CdTe and CIGS Thin-Film Solar Cells: Highlights and Challenges*. in *31st IEEE Photovoltaics Specialists Conference*. 2006.

7. Gerhardinger, P. and D. Strickler, *Fluorine Doped Tin Oxide Coatings - over 50 Years and Going Strong*, in *Innovations in Materials Science*. 2008, Business Wire.

8. Batzill, M. and U. Diebold, *The Surface and Materials Science of Tin Oxide.* Progress in Surface Science, 2005. **79**(2-4): p. 47-154.

9. French, R.H., S.J. Glass, F.S. Ohuchi, Y.N. Xu, and W.Y. Ching, *Experimental and Theoretical Determination of the Electronic-Structure and Optical-Properties of 3 Phases of ZrO_2.* Physical Review B, 1994. **49**(8): p. 5133-5141.

10. Shannon, R.D., *Revised Effective Ionic Radii and Systematic Studies of Interatomic Distances in Halides and Chalcogenides.* Acta Crystallographica, 1976. **A32**: p. 751.

11. Atik, M., J. Zarzycki, and C. Rkha, *Protection of Ferritic Stainless-Steel against Oxidation by Zirconia Coatings.* Journal of Materials Science Letters, 1994. **13**(4): p. 266-269.

12. Izumi, K., H. Tanaka, M. Murakami, T. Deguchi, A. Morita, N. Tohge, and T. Minami, *Coating of Fluorine-Doped ZrO_2 Films on Steel Sheets by Sol-Gel Method.* Journal of Non-Crystalline Solids, 1990. **121**(1-3): p. 344-347.

13. Osterwald, C.R., T.J. McMahon, and J.A.d. Cueto, *Electrochemical Corrosion of SnO_2:F Transparent Conducting Layers in Thin-Film Photovoltaic Modules.* Solar Energy Materials and Solar Cells, 2003. **79**(1).

14. Li, X.A., T.A. Gessert, and T. Coutts, *The Properties of Cadmium Tin Oxide Thin-Film Compounds Prepared by Linear Combinatorial Synthesis.* Applied Surface Science, 2004. **223**(1-3): p. 138-143.

15. Haacke, G., *New Figure of Merit for Transparent Conductors.* Journal of Applied Physics, 1976. **47**(9): p. 4086-4089.

16. Chopra, K.L., P.D. Paulson, and V. Dutta, *Thin-Film Solar Cells: An Overview.* Progress in Photovoltaics, 2004. **12**(2-3): p. 69-92.

17. Badeker, K., *Electrical Conductivity and Thermo-Electromotive Force of Some Metallic Compounds*, Ann. Phys., 1907. **22**(4): p. 749.

18. Minami, T. and T. Miyata, *Present Status and Future Prospects for Development of Non- or Reduced-Indium Transparent Conducting Oxide Thin Films.* Thin Solid Films, 2008. **517**(4): p. 1474-1477.

19. Haacke, G., *Transparent Conducting Coatings.* Annual Review of Materials Science, 1977. **7**: p. 73-93.

20. Kilic, C. and A. Zunger, *N-Type Doping of Oxides by Hydrogen.* Applied Physics Letters, 2002. **81**(1): p. 73-75.

21. Kilic, C. and A. Zunger, *Origins of Coexistence of Conductivity and Transparency in SnO_2.* Physical Review Letters, 2002. **88**(9): p. -.

22. Batzill, M., K. Katsiev, J.M. Burst, U. Diebold, A.M. Chaka, and B. Delley, *Gas-Phase-Dependent Properties of SnO_2 (110), (100), and (101) Single-Crystal Surfaces: Structure, Composition, and Electronic Properties.* Physical Review B, 2005. **72**(16).

23. Burstein, E., *Anomalous Optical Absorption Limit in InSb*, Phys. Rev., 1954. **93**: p. 632.

24. Moss, T., *The Interpretation of the Properties of Indium Antimonide*, Proc. Phys. Soc., 1954. 67B: p. 775.

25. Hartnagel, H.L., A.L. Dawar, A.K. Jain, and C. Jagadish, *Semiconducting Transparent Thin Films*. 1995, Philadelphia: IOP Publishing Ltd.

26. Ashcroft, N.W. and N.D. Mermin, *Solid State Physics*. 1976: Thomson Learning, Inc.

27. Coutts, T.J., D.L. Young, and X. Li, *Characterization of Transparent Conducting Oxides.* MRS Bulletin, 2000. **25**.

28. Hamberg, I. and C.G. Granqvist, *Evaporated Sn-Doped* In_2O_3 *Films: Basic Optical Properties and Applications to Energy-Efficient Windows.* Journal of Applied Physics, 1986. **60**(11): p. R123-R160-R123-R160.

29. Yoshida, Y., *Phd Thesis*. 2004, Colorado School of Mines.

30. Duenow, J.N., *Phd Thesis*. 2008, Colorado School of Mines.

31. Freeman, C.M. and C.R.A. Catlow, *A Computer Modeling Study of Defect and Dopant States in* SnO_2. Journal of Solid State Chemistry, 1990. **85**(1): p. 65-75.

32. Mott, N.F., *Metal-Insulator Transitions*. 1974, London: Taylor and Francis.

33. Wooten, F., *Optical Properties of Solids*. 1972, London: Academic Press, Inc.

34. Pankove, J.I., *Optical Processes in Semiconductors*. 1971: Dover Publications, Inc.

35. Heavens, O.S., *Optical Properties of Thin Solid Films*. 1965, New York: Dover Publications, Inc.

36. O'Neil, D.H., A. Walsh, R.M.J. Jacobs, V.L. Kuznetsov, R.G. Egdell, and P.P. Edwards, *Experimental and Density-Functional Study of the Electronic Structure of* $In_4Sn_3O_{12}$. Physical Review B. **81**(8): p. 085110.

37. Coutts, T.J. (personal communication).

38. Campet, G., S.D. Han, S.J. Wen, J.P. Manaud, J. Portier, Y. Xu, and J. Salardenne, *The Electronic Effect of* Ti^{4+}, Zr^{4+} *and* Ge^{4+} *Dopings Upon the Physical-Properties of* In_2O_3 *and Sn-Doped* In_2O_3 *Ceramics - Application to New Highly-Transparent Conductive Electrodes.* Materials Science and Engineering B-Solid State Materials for Advanced Technology, 1993. **19**(3): p. 285-289.

39. Qadri, S.B., H. Kim, H.R. Khan, A. Pique, J.S. Horwitz, D. Chrisey, W.J. Kim, and E.F. Skelton, *Transparent Conducting Films of* In_2O_3-ZrO_2, SnO_2-ZrO_2 *and* ZnO-ZrO_2. Thin Solid Films, 2000. **377**: p. 750-754.

40. Qadri, S.B., E.F. Skelton, M.Z. Harford, C. Kim, and P. Lubitz, *Electron-Beam Deposition of* ZrO_2-SnO_2 *Films.* Surface & Coatings Technology, 1994. **63**(3): p. 155-157.

41. Asikainen, T., M. Ritala, and M. Leskela, *Atomic Layer Deposition Growth of Zirconium Doped In_2O_3 Films.* Thin Solid Films, 2003. **440**(1-2): p. 152-154.

42. Kim, H., J.S. Horwitz, G.P. Kushto, S.B. Qadri, Z.H. Kafafi, and D.B. Chrisey, *Transparent Conducting Zr-Doped In_2O_3 Thin Films for Organic Light-Emitting Diodes.* Applied Physics Letters, 2001. **78**(8): p. 1050-1052.

43. Qadri, S.B., H.R. Khan, E.F. Skelton, and P. Lubitz, *Indium-Doped Transparent Conducting Oxides of ZrO_2.* Surface & Coatings Technology, 1998. **101**(1-3): p. 94-97.

44. Qadri, S.B., H. Kim, J.S. Horwitz, and D.B. Chrisey, *Transparent Conducting Films of ZnO-ZrO_2: Structure and Properties.* Journal of Applied Physics, 2000. **88**(11): p. 6564-6566.

45. Zhang, B., X.P. Dong, X.F. Xu, X.J. Wang, and J.S. Wu, *Electrical and Optical Properties of ITO and ITO:Zr Transparent Conducting Films.* Materials Science in Semiconductor Processing, 2007. **10**(6): p. 264-269.

46. Zhang, B., X.P. Dong, X.F. Xu, P. Zhao, and J.S. Wu, *Characteristics of Zirconium-Doped Indium Tin Oxide Thin Films Deposited by Magnetron Sputtering.* Solar Energy Materials and Solar Cells, 2008. **92**(10): p. 1224-1229.

47. Gessert, T.A., Y. Yoshida, C.C. Fesenmaier, and T.J. Coutts, *Sputtered IO and ITO Thin Films Containing Zr.* Journal of Applied Physics, accepted 2009.

48. Gessert, T.A., Y. Yoshida, C.C. Fesenmaier, and T.J. Coutts, *Sputtered In_2O_3 and ITO Thin Films Containing Zirconium.* Journal of Applied Physics, 2009. **105**(8): p. 6.

49. Arico, S.F., L.M. Gribaudo, and L.A. Roberti, *Equilibrium Phases Surrounding the Alpha Zr Solid Solution in the Zr-Sn-O System.* Journal of Materials Science, 1996. **31**(21): p. 5587-5591.

50. Dhage, S.R., V. Samuel, R. Pasricha, and V. Ravi, *Studies on SnO_2-ZrO_2 Solid Solution.* Ceramics International, 2006. **32**(8): p. 939-941.

51. Gaillard-Allemand, B., R. Podor, M. Vilasi, C. Rapin, A. Maitre, and P. Steinmetz, *Experimental Study of the SnO_2-ZrO_2 Phase Diagram.* Journal of the European Ceramic Society, 2002. **22**(13): p. 2297-2303.

52. Maitre, A., D. Beyssen, and R. Podor, *Effect of ZrO_2 Additions on Sintering of SnO_2-Based Ceramics.* Journal of the European Ceramic Society, 2004. **24**(10-11): p. 3111-3118.

53. Fang, G.J., Z.L. Liu, Z.C. Zhang, and K.L. Yao, *Preparation of ZrO_2-SnO_2 Thin Films by the Sol-Gel Technique and Their Gas Sensitivity.* Physica Status Solidi a-Applied Research, 1996. **156**(1): p. 81-85.

CHAPTER II

FILM SYNTHESIS BY CHEMICAL VAPOR DEPOSITION

This chapter begins with an explanation of the chemical vapor deposition (CVD) process along with its applications and industrial relevance. The various types of CVD processes are briefly discussed, with a focus on the low-pressure variant. The complexity of the CVD process is explained in terms of the interrelation between gas phase and surface reactions, reactant species and reactor design. A brief review of tin oxide-based TCOs relevant to this work is presented. The chemical vapor deposition of tin oxide and zirconium oxide is discussed and reviewed. Finally, the CVD process, precursors, substrate preparation, and process variables used in this study are fully described.

CVD Process

Chemical vapor deposition (CVD) is a highly controllable and scalable process for uniformly coating large substrates. This technique is widely used in such large and diverse industrial sectors as the integrated circuit (IC) industry, as well as for various functional or protective coatings on glass, containers, structural steel and tool steel.

Tin oxide coated glass is produced at a rate in the hundreds of thousands of square meters annually with the primary production method being CVD [1]. Because of the continued growth of the PV industry which utilizes this material, the production of tin oxide coated glass in 2012 is estimated to be 500M m^2/year [2]. However, these coatings have not been optimized specifically for the needs of the PV industry, and especially not so for the particular properties desired for specific thin film PV technologies , such as CdTe/CdS-based cells. Addressing these issues is a main focus of this work.

The chemical vapor deposition of a thin solid film on a substrate requires the delivery of reactant gases to the deposition zone where the substrate is located. In the deposition zone, the atmosphere is controlled by the pressure and whether other reactant or catalytic species are present. Energy is typically applied in the form of heat. However, variations of the process may include addition of energy in other forms: for example, plasma-enhanced CVD (PECVD) supplies energy via the energetic electrons in the plasma. Given sufficient energy and supply of reactant, reactions occur such that a solid film is deposited on the substrate and volatile reaction byproducts are evacuated from the reactor. A more complete analysis of the CVD process involves the nine steps which are illustrated in Figure 2.1 and are described below [3]:

(1) Reaction gases enter the reactor and then pass into the deposition zone.

(2) Gas phase reactions may occur, which may give off byproducts or supply intermediate reactants. These intermediates may be short-lived and perhaps go undetected (e.g. radicals that quickly react in a step-wise fashion).

(3) Diffusion of the reaction (1) and intermediate (2) gaseous species to the substrate surface.

(4) Reactants adsorb onto the surface of the substrate.

(5) Adsorbed species may diffuse onto the surface of the substrate,

(6) Reactions occur on the surface of the substrate.

(7) By-products of the reaction(s) are desorbed.

(8) By-products (7) diffuse away from the surface.

(9) The by-products are removed from the reactor via convective mass transport.

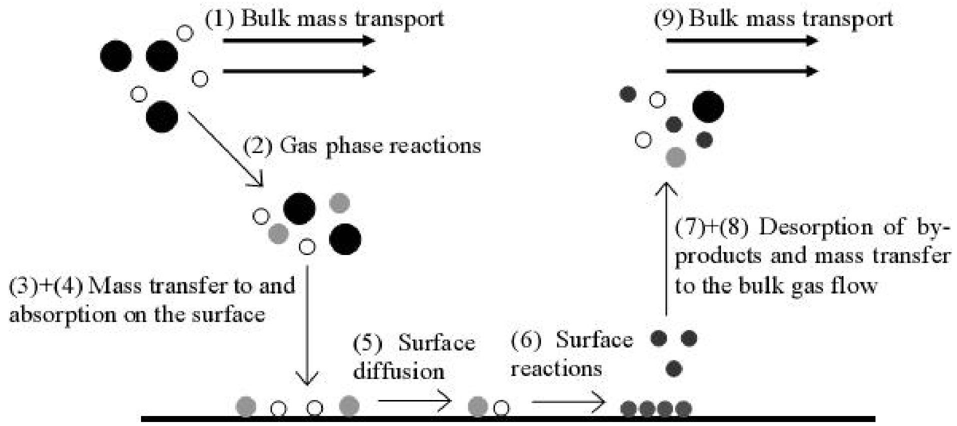

Figure 2.1. An illustration of the central steps in the chemical vapor deposition process [3].

Review of Tin Oxide CVD

SnO_2 thin films and ZrO_2 thin films have been successfully deposited by CVD under various conditions using a variety of precursors [2, 4-7]. Low pressure, LPCVD, systems are compatible with current thin film technologies, and process development gleaned from the coated glass and semiconductor industries may be transferred to large-scale production of new TCOs for PV applications.

Thorough reviews of CVD tin oxide are given in a series of articles by Jarzebski and Marton [8-10]. More recent reviews of tin oxide-based TCOs, their synthesis and properties can be found in [11-13]. A concise review of the history, applications and industrial relevance of fluorine-doped tin oxide is given by Gerhardinger and Strickler [2].

Tin oxide films are prepared on a large scale using mainly one of three precursor chemistries: tin tetrachloride, $SnCl_4$ (TTC); dimethyltin chloride, $(CH_3)_2SnCl_2$ (DMTC); and tetramethyl tin, $Sn(CH_3)_4$ (TMT) [2]. The TTC and DMTC precursors are typically used in an atmospheric pressure CVD (APCVD) setting. Because of the attached chlorine ligands, TTC and DMTC are reacted with H_2O or water and O_2 as the oxidizers in order to form HCl. Li *et al* have determined that tin oxide films formed from precursors with chlorine ligands tend to include both chlorine and carbon in the films [14]. These unintentionally incorporated impurities limit the optical properties and carrier mobility. The chlorine-free TMT precursor is used in this study as it was found to yield films with lower optical absorption when compared to those formed from TTC or DMTC [4]. A thorough review of the CVD process parameters, reaction kinetics and other details on these and other tin precursors can be found in [15].

The reaction of TMT to form tin oxide is described by the following combustion reaction

$$\mathrm{Sn}\left(\mathrm{CH}_3\right)_4\left(\mathrm{g}\right) + 8\ \mathrm{O}_2\left(\mathrm{g}\right) \rightarrow \mathrm{SnO}_2\left(\mathrm{s}\right) + 6\ \mathrm{H}_2\mathrm{O}\ \left(\mathrm{g}\right) + 4\ \mathrm{CO}_2\left(\mathrm{g}\right) \qquad (2.1)$$

where ideally only water and carbon dioxide are the byproducts [16-18]. However, Borman *et al* has proposed that several reaction pathways take place as shown in Figure 2.2 [19]. The initial reactions are the pyrolysis of TMT to form methyl radicals; the radicals are in turn oxidized and attack TMT to further progress this reaction. The remaining organotin radical may then react reversibly with oxygen to form the peroxy species shown in Figure 2.2. These peroxy species are the key intermediates toward further oxidation and β-elimination. Because the films are observed to be typically carbon-free, it is argued that the peroxy species tend to form SnO and SnO_2 as the film precursors just before deposition [15, 20, 21].

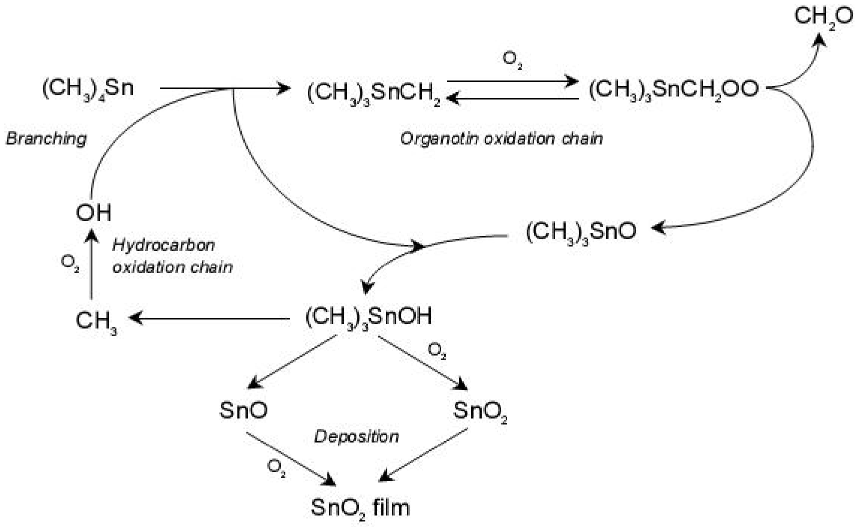

Figure 2.2. Possible major reaction pathways for the combustion of TMT by O_2 [19].

The deposition temperature range for the chemical vapor deposition of tin oxide by TMT falls in the range of approximately 400-800˚C. Activation energies have been reported in the range of 106-174 kJ/mol O_2 [15, 19, 22-25]. In the current study, an apparent activation energy of 110 kJ/mol was found in the temperature range 500-550 ˚C. The deposition rates at various temperatures as reported by several authors are shown in Figure 2.3 [15, 19, 22-25]. A large variation, about two orders, in deposition rates between the sets of data is likely due to the variation in process parameters and reactor design.

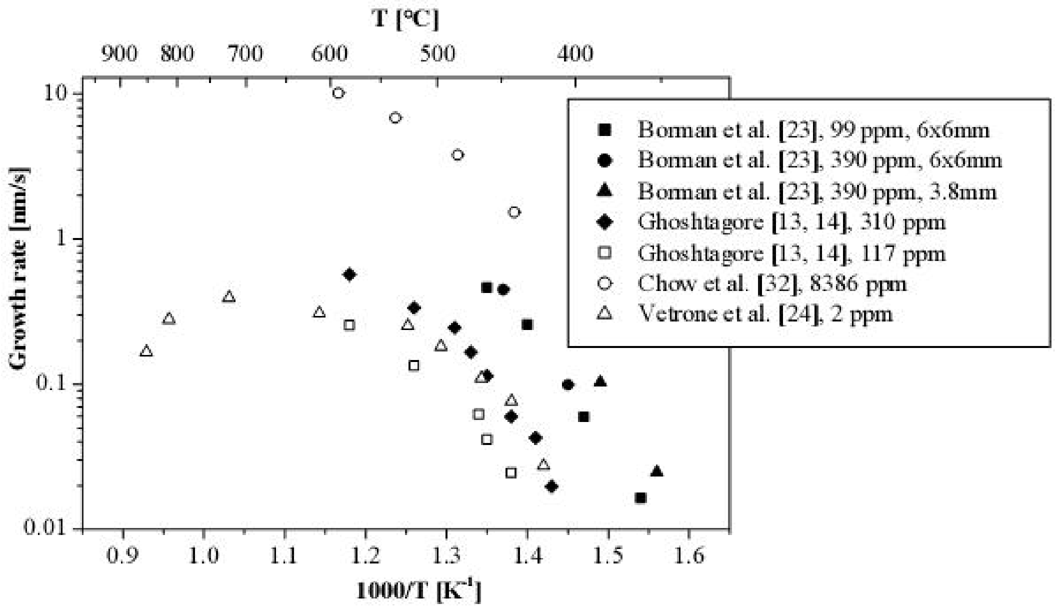

Figure 2.3. Reported growth rates of SnO_2 films formed by CVD of TMT + O_2 [15, 19, 22-25]. The reaction rate limited activation energies are reported in the range of 106-174 kJ/mol. In the current study, the activation energy is found to be 110 kJ/mol in the temperature range 500-550˚C.

The electrical properties of many TCO films are reported to depend on thickness [7, 12, 26]. For zinc oxide-based films, both carrier concentration and mobility were found to increase with thickness in the range of 100-1000 nm [27]. For indium oxide based films, a similar observation is reported over a narrower range of 100-375 nm, indicating that there was not a large change in conductivity for films thicker than about 380 nm [28, 29]. For tin oxide based TCO films formed by CVD, such observations are not typically found [8-10]. However, a critical thickness, which is typically around 100 nm, has been reported [30, 31]. A sharp decrease in resistivity is observed between 50-100 nm film thickness, and films thicker than about 100 nm have similar electrical properties, as can be seen in Figure 2.4 [30]. It could be that films less than approximately 50 nm in thickness are discontinuous leading to the observed increase in measured electrical resistance. Another explanation is that the thicker films are also associated with a longer deposition time, which allows for grain growth and crystallization to occur, both of which would serve to increase the carrier concentration and mobility. The desired sheet resistance values for a TCO film typically require film thicknesses to be in the range of 200-1000 nm. Therefore, the aforementioned thickness dependency is likely not an issue for such applications.

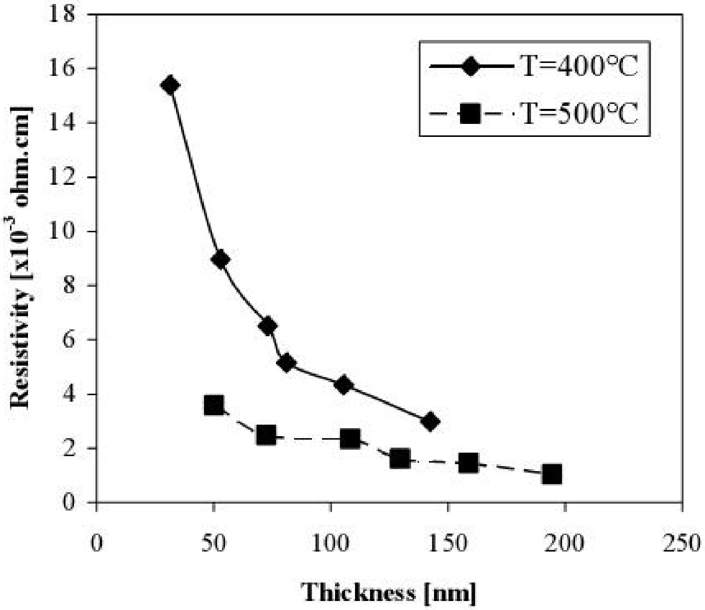

Figure 2.4. Reported thickness dependence of the electrical properties for tin oxide films formed by the oxidation of TMT [30].

Review of the CVD of ZrO_2

Most recent studies of ZrO_2 thin films have focused on their application as the dielectric in integrated circuits (ICs) [6, 32-36]. For reasons such as the desire for contamination control, low deposition rates and ultrathin films (less than 20 nm), the reactions are typically done in a high vacuum (HV) chamber with deposition pressures in the mTorr range [6, 34, 35]. These deposition pressures are 3-4 orders of magnitude lower than the 1-100 Torr pressure range typically utilized in LPCVD. Since no reports on LPCVD of zirconia from ZTB are found in the literature, a short review of relevant HVCVD results is presented here.

In general, the deposition of zirconia from the ZTB precursor is reported to occur for substrate temperatures in the range 300-475˚C [33, 34]. Song *et al* and Cameron *et al* report deposition rates of 1-8 nm/min for the temperature range 350-475˚C [33, 34]. These rates are quite low compared to the 10-50 nm/min rates for tin oxide by TMT, indicating the possibility for forming films with low Zr:Sn ratios in alloyed films. Chang *et al* report activation energies of 29 kcal/mol (121 kJ/mol) and 4 kcal/mol (17 kJ/mol) for the temperature ranges 300-400˚C and 400-450˚C, respectively [37]. Above about 450˚C, the deposition rate is mainly controlled by decomposition and desorption of precursor and byproduct species, respectively.

Song *et al* have studied the optical properties of ZrO_2 using spectroscopic ellipsometry [33]. The variation of the real part of the refractive index, *N*, with deposition temperature is shown in Figure 2.5. The values of ~ 2.0 for the higher temperature values are in agreement with other reports on thin film zirconia, as well as the bulk value of 2.16 [37, 38]. Because there is a correlation between refractive index and permittivity, there is a similar trend that permittivity values of thin film zirconia may also approach that of the bulk [39]. In the current study, the deposition temperatures for the alloyed films are at high temperaure, and as discussed in Chapter I, a high permittivity is desirable.

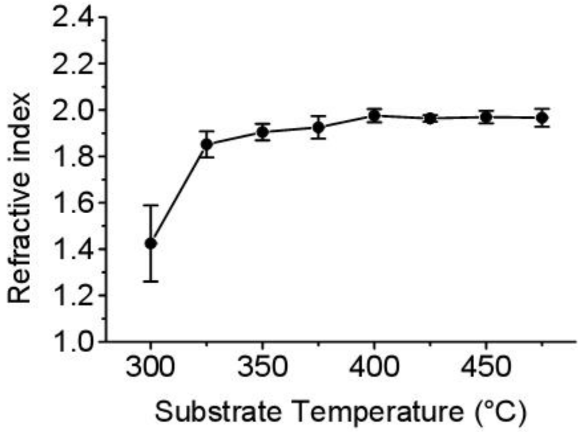

Figure 2.5. Evolution of the refractive index with deposition temperature for HVCVD ZrO_2 on Si [33]. A similar trend is observed in the current work.

Description of the LP-MOCVD Reactor

The LPCVD system at NREL is a modified low pressure metalorganic (MO) CVD reactor (CVD Equipment Co.) [31]. The reactor is a cold wall quartz tube design with 4 gas inlet injectors which allow for precursor gases to be delivered to the reactor separately. Ultra-high purity (UHP) O_2 (99.999% purity) is the oxidant and N_2 (99.95% purity) is used as the carrier and as a diluent gas. Precursor, diluent and reactant gases enter at one end of the chamber through their respective injectors, flow down the length of the chamber and are then pumped out at the other end, as shown in Figure 2.6. Controlled heating and thermal stability of the substrates is achieved by use of a coated graphite susceptor which has a 10 cm wide x 30 cm long x 1.1 mm deep recessed sample pocket . The sample is heated from below by 5-zone independently controlled IR lamps.

Five type K thermocouples, associated with the five heating zones, are in thermal contact with the susceptor in a recess located just below the sample pocket. The graphite susceptor is supported by quartz rods. In this way, only the susceptor, quartz supports and substrates are in the heated deposition zone. The chamber can be pumped to approximately 0.1 Torr by a mechanical pump designed to handle toxic and corrosive gases. Exhaust gases flow through a pyrolizer at 650°C where the exhaust is mixed with air to burn off any unreacted hydrocarbons, reactive precursors and reaction byproducts. The gas mixture exiting the pyrolizer flows through a wet scrubber system to capture any acidic species and is exhausted to atmosphere

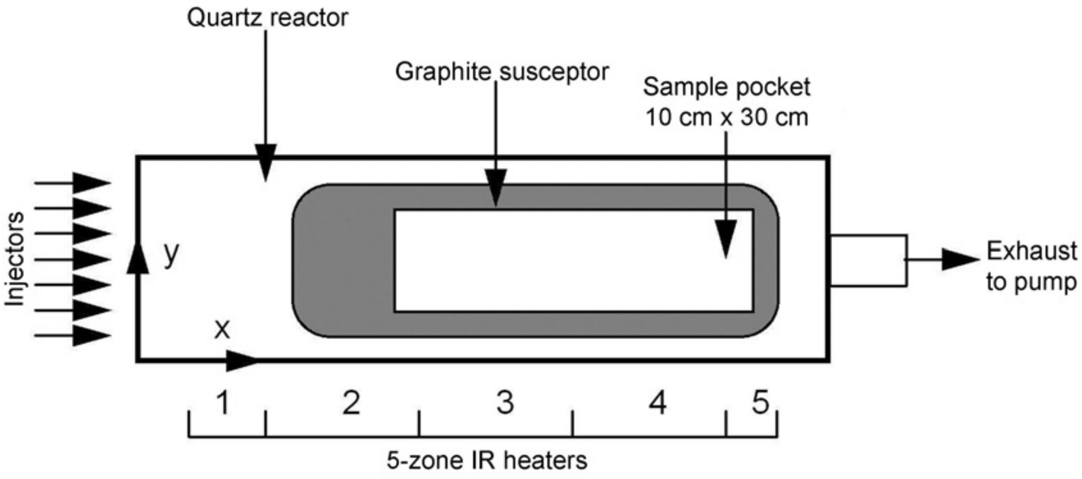

Figure 2.6. Schematic of reactor, showing susceptor and sample pocket with respect to the heating zones.

Substrate Preparation

The substrates used in this study are 1.1 mm thick, 10 cm x 10 cm square, Corning 1737 aluminosilicate glass. The samples were cleaned using the procedure to process NREL's high-efficiency cells [40, 41]. Individual slides are loaded into a Fluoroware spin-rinse-dryer (SRD) compatible carrier. The loaded carriers are soaked in a 1% Liquinox in de-ionized (DI) water solution at 80°C for approximately 2 hours, and then sonicated for 5-10 min. They are manually rinsed and sonicated 5 more times, then rinsed and dried in the cleanroom SRD until an output resistance of 12 MΩ·cm is attained.

Precursor Selection

All precursors in this study are liquid at room temperature. The metal organics are delivered via temperature-controlled bubblers using N_2 as the carrier and diluent gas. Tetramethyltin (TMT), $Sn(CH_3)_4$ (Air Products, 99.999% purity) was used for the tin precursor. Previous studies revealed that tin oxide films deposited with TMT had lower resistivity and higher optical transparency than films deposited from the more common $SnCl_4$ [4, 5, 31]. The fluorine precursor is bromotrifluoromethane, $CBrF_3$ (Mattheson, 99.5 mol% purity). Zirconium tert-butoxide (ZTB) is the zirconia precursor (Air Products, 99.99% purity). The vapor pressure curves for TMT and ZTB indicate that in the pressure regime of interest (20-80 Torr), we should expect films with high Sn:Zr content if the precursors are delivered at the same temperature. To decrease the Sn:Zr ratio the ZTB precursor can be heated to 40-65°C, the TMT can be held to 15-20°C, and a high ZTB:TMT flow rate ratio should be used. The Rogers group has extensive experience with deposition of zirconia films on Si via ultra-high vacuum CVD using the

ZTB precursor [6, 33, 42]. This knowledge base was leveraged to advance our understanding of the current work.

CVD Process Parameters

The CVD reactor design was described in a previous section. Gas delivery to each injector is controlled by dedicated pneumatic valves and precision mass-flow controllers (MKS). The metal-organic (MO) precursor partial pressures are controlled independently from the chamber pressure via feedback-looped piezo valves. Total pressure in the chamber can be controlled in the range of 1-100 Torr by a throttle valve located just in front of the mechanical rotary vane pump. All pressures are monitored by separate capacitance manometer gauges (MKS Baratron).

We identified process variables and formulate the mass balance equations in the following way. The control variables are: flow of N_2 carrier gas into the bubbler, F_{N2}; the bubbler temperature, T_{bub}; and the bubbler pressure, P_{bub}. The dependent variables are: the vapor pressure of the metalorganic precursor, P_{MO}, at T_{bub}; flow of the metalorganic precursor, F_{MO}; and the total flow out of the bubbler, F_O. Assuming saturated flow out of the bubbler, the mass balance equations are given by the precursor mol fraction out of the bubbler, x_{MO}

$$x_{MO} = \frac{P_{MO}}{P_{bub}} = \frac{F_{MO}}{F_O} \tag{2.2}$$

and the total flow out of the bubbler is

$$F_O = F_{N_2} + F_{MO} \tag{2.3}$$

Solving for the metalorganic precursor flow gives

$$F_{MO} = F_{N_2} \frac{P_{MO}}{P_{bub} - P_{MO}} \tag{2.4}$$

The range of initial process parameters for deposition of the individual oxides was defined by gross calculations obtained from the vendor-supplied vapor pressure curves, as well as from empirical data reported in the literature [20, 31, 33, 34]. The vapor pressure curves for the MO precursors are shown in Figure 2.7, while the calculated precursor flow rates are presented in Figure 2.8. For tin oxide, the TMT precursor pressure is set to 200 Torr and the bubbler is held at room temperature; bubbler flow rate is maintained constant at 6 sccm for all data in the present study. Using the vapor pressure curves, and calculations for various partial pressure-flow rates-temperature schemes, the ZTB pressure is maintained at 80 Torr and the ZTB bubbler temperature is controlled in the range of 40-65°C. The ZTB bubbler flow rate is studied in the range of 10-90 sccm and diluent N_2 carrier flow is on the order of 1-2 SLPM which is adjusted to maintain balanced injector flow and total flow. To prevent ZTB condensation, the gas lines from the bubbler to the gas injectors are heated to 85°C. Oxygen and $CBrF_3$ are varied systematically to achieve different O:F, and also to optimize film properties and performance. In general, the O_2 flow rate is typically 450 sccm, while the $CBrF_3$ is varied in the range of 0-900 sccm. Deposition temperatures were varied in the range of 350-600°C. Total pressure in the chamber was in the range of 20-80 Torr.

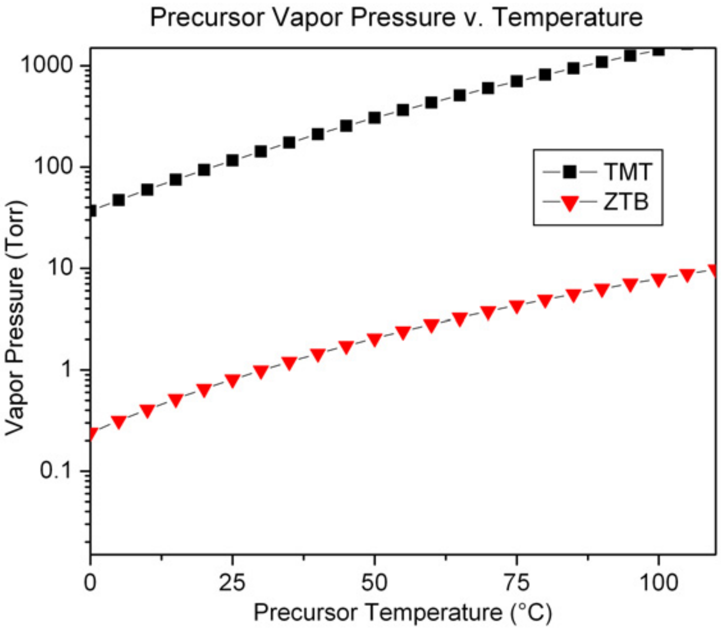

Figure 2.7. Vapor pressure curves for the two MO precusrsors chosen. Here we note the challenge of combining processes involving precursors whose vapor pressures differ by about two orders of magnitude.

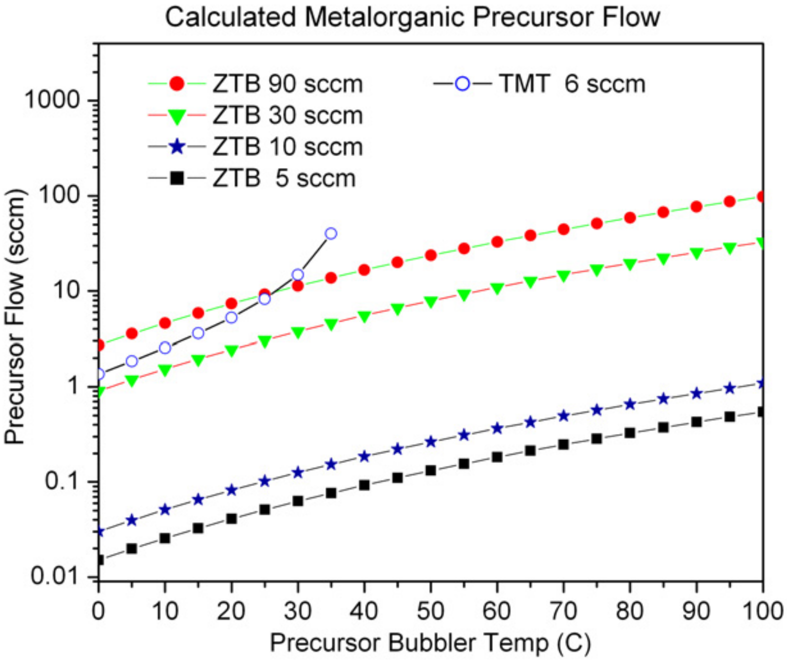

Figure 2.8. The calculated flow of the metalorgainc species based on the calculations shown above.

We have observed that the deposited films' properties depend on the cleanliness of the deposition chamber. In the "clean" process, the quartz reactor chamber, graphite susceptor and accompanying quartz support rods, chamber inserts, etc have all undergone a careful cleaning process involving multiple acid etches to remove all material from previous depositions. Subsequently, three sacrificial tin oxide depositions are performed to "season" the deposition chamber walls and substrate holder susceptor. Under these conditions, the next several depositions yield films which display the highest performance. That is, the carrier mobility is on the order of 40 $cm^2/V{\cdot}s$, and the corresponding optical transmittance is about 85%, including the glass substrate. However, only a few depositions (about ten) can be performed before another cleaning process is required. Further, film properties degrade gradually with each deposition. In the "dirty" process mode, greater than about 12 depositions have taken place since the last full cleaning procedure, and the film properties have stabilized resulting in a carrier mobility of ~ 27 $cm^2/V{\cdot}s$, and these results are highly repeatable for several dozen depositions. The degradation of the films electro-optical properties then occurs very rapidly, and is easily identified as non-uniformity in thickness, electrical properties or visible inclusions of particulates in or darkening of the film. For repeatability reasons, we have chosen to operate in the "dirty" mode for all depositions studied in this current work. In this way, we can more easily identify changes that are directly resultant from changes in processing, dopant addition, or alloying concentration.

References

1. Gray, M.J. and K. Stroble, *Off-Line APCVD Offers Paradigm Shift for TCO Glass End Users*. Photovoltaics World, 2010 (2).

2. Gerhardinger, P. and D. Strickler, *Fluorine Doped Tin Oxide Coatings - over 50 Years and Going Strong*, in *Innovations in Materials Science*. 2008, Business Wire.

3. Smith, D., *Thin-Film Deposition: Principles and Practice*. 1995: McGraw-Hill Professional.

4. Li, X., J. Penkow, B. To, and T. Gessert, *Comparison between Research-Grade and Commercially Available SnO_2 for Thin-Film CdTe Solar Cells*, in *33rd IEEE Photovoltaics Specialists Conference,*. 2008: San Diego, CA.

5. Shanthi, E., A. Banerjee, V. Dutta, and K.L. Chopra, *Electrical and Optical-Properties of Tin Oxide-Films Doped with F and (Sb+F).* Journal of Applied Physics, 1982. **53**(3): p. 1615-1621.

6. Song, Z., L.M. Sullivan, and B.R. Rogers, *Study on the Initial Deposition of ZrO_2 on Hydrogen Terminated Silicon and Native Silicon Oxide Surfaces by High Vacuum Chemical Vapor Deposition.* Journal of Vacuum Science & Technology A, 2005. **23**(1): p. 165-176.

7. Haacke, G., *Transparent Conducting Coatings.* Annual Review of Materials Science, 1977. **7**: p. 73-93.

8. Jarzebski, Z.M. and J.P. Marton, *Physical Properties of SnO_2 Materials*, Journal of the Electrochemical Society, 1976. **123**: p. 199.

9. Jarzebski, Z.M. and J.P. Marton, *Physical Properties of SnO_2 Materials*, Journal of the Electrochemical Society, 1976. **123**: p. 299.

10. Jarzebski, Z.M. and J.P. Marton, *Physical Properties of SnO_2 Materials*, Journal of the Electrochemical Society, 1976. **123**: p. 333.

11. Chopra, K.L., S. Major, and D.K. Pandya, *Transparent Conductors -- A Status Review*, Thin Solid Films, 1983. **102**(1).

12. Hartnagel, H.L., A.L. Dawar, A.K. Jain, and C. Jagadish, *Semiconducting Transparent Thin Films*. 1995, Philadelphia: IOP Publishing Ltd.

13. Chopra, K.L. and V. Dutta, *Electronic and Optical-Properties of Polycrystalline Semiconducting-Films.* Journal De Physique, 1982. **43**(Nc1): p. 141-152.

14. Li, X., J. Pankow, and Y. Yan. *Impurity Study of Optical Properties in Fluorine-Doped Tin Oxide for Thin-Film Solar Cells*. in *Materials Research Society Symposium*. 2009.

15. van Mol, A.M.B., *Phd Thesis*. 2003, TU Eindhoven.

16. Gordon, R.G., *Us Patent 4,187,336*. 1980.

17. Gordon, R.G., *Us Patent Re31,784*. 1984.

18. Strickler, D.A., *Phd Thesis*. 1989, Harvard University.

19. Borman, C.G. and R.G. Gordon, *Reactive Pathways in the Chemical Vapor-Deposition of Tin Oxide-Films by Tetramethyltin Oxidation*. Journal of the Electrochemical Society, 1989. **136**(12): p. 3820-3828.

20. Zawadzki, A.G., C.J. Giunta, and R.G. Gordon, *Kinetic Modeling of the Chemical Vapor Deposition of Tin Oxide from Tetramethyltin*, Journal of Physical Chemistry, 1992. **96**(13): p. 5364.

21. Muranoi, T. and M. Furukoshi, *Properties of Stannic Oxide Thin-Films Produced from* $SnCl_4$-H_2O *and* $SnCl_4$-H_2O_2 *Reaction Systems*. Thin Solid Films, 1978. **48**(3): p. 309-318.

22. Chow, T.P., M. Ghezzo, and B.J. Baliga, *Antimony-Doped Tin Oxide-Films Deposited by the Oxidation of Tetramethyltin and Trimethylantimony*. Journal of the Electrochemical Society, 1982. **129**(5): p. 1040-1045.

23. Ghoshtagore, R.N. in *Proc. Int. Conf. Chem. Vap. Dep.* 1977.

24. Ghoshtagore, R.N., *Mechanism of CVD Thin-Film* SnO_2 *Formation*. Journal of the Electrochemical Society, 1978. **125**(1): p. 110-117.

25. Vetrone, J. and Y.W. Chung, *Organometallic Chemical Vapor-Deposition of* SnO_2 *Single-Crystal and Polycrystalline Films*. Journal of Vacuum Science & Technology a-Vacuum Surfaces and Films, 1991. **9**(6): p. 3041-3047.

26. Minami, T., *Present Status of Transparent Conducting Oxide Thin-Film Development for Indium-Tin-Oxide (ITO) Substitutes*. Thin Solid Films, 2008. **516**(17): p. 5822-5828.

27. Duenow, J.N., *Phd Thesis*. 2008, Colorado School of Mines.

28. Yoshida, Y., *Phd Thesis*. 2004, Colorado School of Mines.

29. Hamberg, I. and C.G. Granqvist, *Evaporated Sn-Doped* In_2O_3 *Films: Basic Optical Properties and Applications to Energy-Efficient Windows*. Journal of Applied Physics, 1986. **60**(11): p. R123-R160-R123-R160.

30. Murty, N.S., G.K. Bhagavat, and S.R. Jawalekar, *Effect of Deposition Parameters on the Microstructure of Chemically Vapour-Deposited SnO_2 Films*, Thin Solid Films, 1983. **102**: p. 283.

31. Li, X.A., T.A. Gessert, and T. Coutts, *The Properties of Cadmium Tin Oxide Thin-Film Compounds Prepared by Linear Combinatorial Synthesis.* Applied Surface Science, 2004. **223**(1-3): p. 138-143.

32. Peacock, P.W. and J. Robertson, *Bonding, Energies, and Band Offsets of Si-ZrO_2 and HfO_2 Gate Oxide Interfaces.* Physical Review Letters, 2004. **92**(5): p. -.

33. Song, Z., B.R. Rogers, and N.D. Theodore, *Spectroscopic Ellipsometry Characterization of ZrO_2 Films on Si(100) Deposited by High-Vacuum-Metalorganic Chemical Vapor Deposition.* Journal of Vacuum Science & Technology A, 2004. **22**(3): p. 711-718.

34. Cameron, M.A. and S.M. George, *ZrO_2 Film Growth by Chemical Vapor Deposition Using Zirconium Tetra-Tert-Butoxide.* Thin Solid Films, 1999. **348**: p. 90-98.

35. Chang, J.P., Y.-S. Lin, and K. Chu, *Rapid Thermal Chemical Vapor Deposition of Zirconium Oxide for Metal-Oxide-Semiconductor Field Effect Transistor Application.* Journal of Vacuum Science & Technology B, 2001. **19**(5): p. 1782-1787.

36. Wallace, R.M. and G. Wilk, *High-Kappa Gate Dielectric Materials.* Mrs Bulletin, 2002. **27**(3): p. 192-197.

37. Chang, J.P., Y.-S. Lin, S. Berger, A. Kepten, R. Bloom, and S. Levy, *Ultrathin Zirconium Oxide Films as Alternative Gate Dielectrics.* Journal of Vacuum Science & Technology B, 2001. **19**(6): p. 2137-2143.

38. French, R.H., S.J. Glass, F.S. Ohuchi, Y.N. Xu, and W.Y. Ching, *Experimental and Theoretical Determination of the Electronic-Structure and Optical-Properties of 3 Phases of ZrO_2.* Physical Review B, 1994. **49**(8): p. 5133-5141.

39. Wilk, G.D., R.M. Wallace, and J.M. Anthony, *High-Kappa Gate Dielectrics: Current Status and Materials Properties Considerations.* Journal of Applied Physics, 2001. **89**(10): p. 5243-5275.

40. Rose, D.H., F.S. Hasoon, R.G. Dhere, D.S. Albin, R.M. Ribelin, X.S. Li, Y. Mahathongdy, T.A. Gessert, and P. Sheldon, *Fabrication Procedures and Process Sensitivities for CdS/CdTe Solar Cells.* Progress in Photovoltaics, 1999. **7**(5): p. 331-340.

41. Wu, X.Z., *High-Efficiency Polycrystalline CdTe Thin-Film Solar Cells.* Solar Energy, 2004. **77**(6): p. 803-814.

42. Geil, R.D., B.R. Rogers, Z. Song, and R.A. Weller, *Interfacial Analysis Using Time-of-Flight Medium Energy Backscattering.* Journal of Vacuum Science & Technology A, 2004. **22**(4): p. 1129-1133.

CHAPTER III

CHARACTERIZATION METHODS

In this section we describe the various methods used to characterize or obtain quantitative information about the samples. For each type of measurement, the general technique as well as the particular instrument is described. When appropriate, typical ranges of values and expected error are given. The advantages and disadvantages of the different approaches are discussed. X-ray photoelectron spectroscopy and atomic force microscopy measurements were performed exclusively at Vanderbilt University in Dr. Rogers' laboratory and the Vanderbilt Institute for Nanoscale Science & Engineering (ViNSE), respectively. Electrical, optical, profilometry and X-ray diffraction measurements were carried out in the laboratories of the National Center for Photovoltaics at the National Renewable Energy Laboratory (NREL), though we note that facilities exist for most of these measurements at Vanderbilt.

Profilometry and Etching

An accurate measurement of a film's thickness is necessary for determination of properties such as the deposition rate, bulk carrier concentration and resistivity. Physical measurements of film thickness were carried out using a stylus profilometer (Veeco Dektak 8). The uncertainty in the measurement is estimated to be ± 20 nm. Since the target thickness for most films studied is in the range of 200-1000 nm, this is not a large fractional error; generally, the obtained thickness agreed well with other techniques, as will be discussed in following sections. Using the built-in optical microscope and camera, the position of a step-edge established by etching is found. The stylus is lowered slowly into contact with the film surface and is rastered laterally over a chosen distance, typically 1-2.5 μm, where the center position is chosen to be near the step edge. An average height of either side of the step is taken; the difference between these two heights is the recorded film thickness. For each sample, at least three measurements are taken at different locations on the sample surface.

The advantages of using profilometry are that the measurements are direct, and therefore do not require a model or any assumptions to be made about the films' properties, as is the case for optical techniques such as ellipsometry or reflectometry. The disadvantages of a profilometer are that the stylus is in physical contact with the film, which could scratch or contaminate softer materials, as well as the aforementioned error. Further, it is required that a fairly sharp interface exists between coated (film) and uncoated substrate (bare glass) in order to facilitate the measurement. In our studies, this requires the film to be etched chemically in order to establish an abrupt step between the film and bare substrate.

To obtain a step edge for the profilometry measurement, it is necessary to remove part of the film to expose the glass substrate. Kapton tape (3M) was used to mask the film, exposing a small strip about 2 mm in width. Tin oxide is difficult to chemically etch. Therefore a reductive etch was utilized, consisting of coating the film surface with a light dusting of zinc powder (100 mesh, Alfa Aesar), then carefully applying small droplets of 38% hydrochloric acid (HCl). The reaction between the Zn and HCl produces free hydrogen which acts to reduce the tin oxide to Sn^{4+}, and the reduced tin reacts with

HCl to form soluble tin chloride. The remaining solution and suspended particles are rinsed away with DI water. Typically, a single process can remove 300-600 nm of tin oxide. The process is repeated as necessary to remove thicker or particularly stubborn films.

Because of the difficulty etching films of zirconia or those containing ZrO_2, some substrates were "masked" with titania powder just prior to deposition. The procedure begins by mixing titania powder (Alfa Aesar) with acetone, into a slurry. This mixture is applied to the glass substrate to form small circular droplets approximately 1 mm in diameter. In this way, the TiO_2 is removed post-deposition by simply blowing with compressed N_2. However, at temperatures higher than about 400˚C, removal of the titania is difficult and, though unlikely, it remains unclear whether chemical reactions with the titania powder and the film or precursors take place during deposition. Therefore, this method has not been used for other than a few low temperature depositions of ZrO_2 to aid in the initial ellipsometer models.

Spectroscopic Ellipsometry

Due to the large number of samples obtained in the combinatorial studies, it was identified early that measuring thickness, using the etch/profilometer method described earlier, was a potential bottleneck (in time) and was also undesirable due to the destructive nature of the etching process. Further, as will be discussed later, it was found that films of ZrO_2 or tin oxide films containing ZrO_2 were much slower (to near impossible) to chemically etch. This prompted a determined effort to establish a quick, repeatable and non-destructive technique with which to ascertain film thicknesses.

Ellipsometry is a non-contact optical technique widely employed in the routine metrology of semiconductor materials, among others [1]. In general, the technique works as follows: light of known (linear) polarization is incident upon the film/substrate surface and is (most generally) polarized elliptically as it is reflected from the sample surface to a detector, as shown in Figure 3.1 below. The shape and orientation of the ellipse depend on the angle of incidence, incident light polarization, and the properties of the surface from which it is reflected. The ellipsometer's detector measures the change in magnitude, ψ, and phase, Δ, of the reflected light, which is extremely accurate because these values are the ratio of the orthogonal polarization reflection coefficients, given by:

$$\tan\left(\Psi\right)e^{i\Delta} = \frac{R_P}{R_S} \tag{3.1}$$

where R_P and R_S are the Fresnel coefficients, and where p and s refer to the parallel and perpendicular (German, "senkrect") reflectivities, respectively [2]. In the current studies, the instruments used are spectroscopic ellipsometers (SE) which measure the polarization change over a range of incident light wavelengths. The fixed angle (70˚) SE instrument (α-SE, JAWoollam Co) has a maximum range of 250-800 nm. A variable-angle instrument (M-2000IR, JAWoollam Co) includes the NIR wavelength range, with the expanded range of 180-1700 nm, as well as the capability for transmission measurements. The obtained ellipsometry measurement is displayed as a plot of ψ and Δ versus wavelength (or equivalently, energy, frequency or wavenumber).

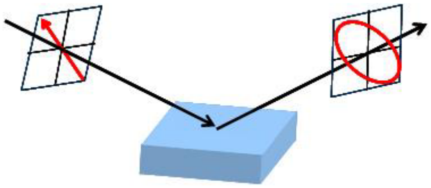

Figure 3.1. Schematic of a typical ellipsometry setup: the incident beam is of fixed linear polarization and the elliptically-polarized reflected beam is detected. The angles of incidence and reflectance are typically ~ 70˚ with respect to sample normal.

Because the raw data gives little physical insight, a model must be employed to fit the experimental data in order to extract physical quantitative information. Once a model is chosen, the supplied software (JAWoollam WVASE or CompleteEASE) then uses an iterative algorithm to minimize the error to arrive at a solution with lowest mean square error (MSE). However, this result may correspond to a local minimum, rather than the global minimum, which could lead to a non-physical solution. A non-physical solution would also result from an incorrect model. Such solutions may be detected by an experienced operator. However, because often several variables are fit simultaneously, coupling between fitting parameters can give solutions which are plausible but not unique.

For a transparent dielectric material with a bandgap outside of the measured spectral range, such as ZrO_2 (E_G ~ 5.8 eV), a dispersion model such as the Cauchy model, may sufficiently describe the behavior of the real part of optical functions and allow for accurate extraction of physical quantities such as film thickness and surface roughness [3]. The real part of the index of refraction as a function of wavelength is given in the Cauchy model by:

$$n(\lambda) = A + \frac{B}{\lambda^2} + \frac{C}{\lambda^4} \tag{3.2}$$

and the terms A, B, and C are iteratively adjusted to fit the experimental data [3]. However, the obtained results from such a fitting routine could be non-physical, since the model does not account for losses, and thus there is no constraint for Kramers-Kronig consistency. A more robust model based on oscillator approximations, however, has been shown to be more quantitatively accurate with regard to extracting the optical functions in particular [4]. The complex permittivity in the Lorentz oscillator model can be written as function of photon energy by:

$$\tilde{\varepsilon}(E) = \frac{A \cdot E_C}{E_C^2 - E^2 - iBr \cdot E} \tag{3.3}$$

where A, Br and E_C are the amplitude, broadening and center energy, as shown in Figure 3.2 below [5].

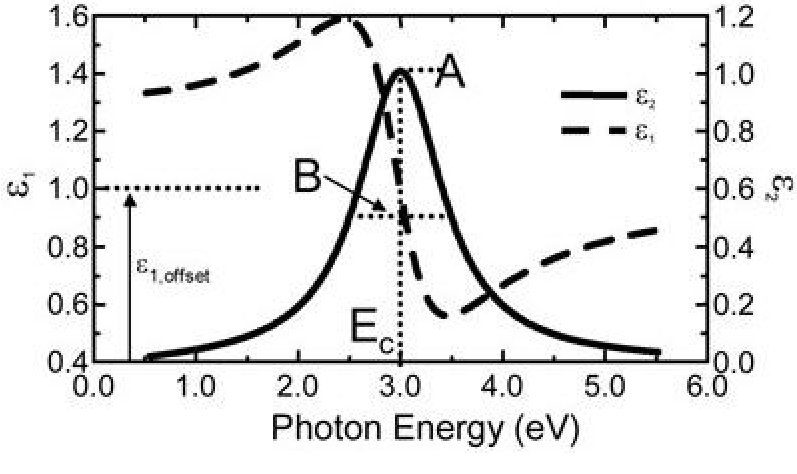

Figure 3.2. The permittivity functions and the terms of interest for an oscillator model; A, B and E_C are the amplitude, broadening and center energy [5].

In the current work, analysis of the data for ZrO_2 films on glass were obtained by fitting a model consisting of: i) a Cauchy dispersion layer for the glass substrate, ii) a Lorentz oscillator for the ZrO_2 film, and iii) an effective medium approximation (EMA) of average surface roughness, R_A. The EMA layer assumes a 50% void fraction at the surface and averages the optical functions with the bulk film properties and that of air (*i.e.* $n_{AIR} = 1$).

As was discussed in Chapter I, a TCO material has a transmittance bandwidth which encompasses all or most of the visible spectral range. The fundamental absorption edge at the shorter wavelength end of the spectrum is typically around 300-400 nm for a TCO film. Near the plasma wavelength, typically > 1000-1500 nm for a TCO, absorption and reflection become dominant. Because both mechanisms occur within the range of our ellipsometry measurements, the model must account for these two fundamentally different absorption mechanisms. Further, TCO materials often exhibit a vertical non-uniformity in their electro-optical properties. For instance, zinc oxide-based materials are often reported as having a large inhomogeneity in the charge carrier concentration and mobility throughout the thickness of the film [6]. For these reasons, it has proven notoriously difficult to model TCO films accurately.

Tin oxide-based films typically have large concentrations of free carriers, resulting in considerable absorption in the longer wavelengths. The absorption is not taken into account by the more standard optical layer models such as the Cauchy model or Lorentz oscillator model. The fact that these films are also optically transparent in the visible precludes using a model for thin metal films, for instance. The model developed in this study consists of: i) a dispersion model for the glass substrate, ii) a graded two-oscillator model for the TCO film made up of a Lorentz + Drude model.; and iii) an EMA surface roughness layer. The Drude model includes allowance for linear inhomogeneity.

The Drude oscillator is similar to the Lorentz oscillator, but the center energy is set to zero. The permittivity relation in the Drude oscillator is given by:

$$\tilde{\varepsilon}_D(E) = -\frac{A \cdot Br}{E^2 + iBr \cdot E}. \tag{3.4}$$

A and *Br* are expressed by

$$A = \frac{\bar{h}^2 e^2 N_{OPT}}{m^* \varepsilon_0} \tag{3.5}$$

and

$$Br = \frac{\bar{h}}{\tau_{OPT}} = \frac{\bar{h} e}{m^* \mu_{OPT}}, \tag{3.6}$$

where N_{OPT}, τ_{OPT}, and μ_{OPT} are the "optical" carrier concentration, scattering time and mobility, respectively and where $\bar{h}$ is Planck's constant, *h*, divided by *2π* [5, 7]. Note: in the literature, the broadening term, *Br*, is sometimes denoted as *B*, *Γ* or Γ_D.

The Drude oscillator can be used to extract the resistivity and mean scattering time. The complex permittivity relates to the free electrons by

$$\tilde{\varepsilon}_D(E) = -\frac{\bar{h}}{\varepsilon_0 \rho (\tau \cdot E^2 + i\bar{h}E)} \tag{3.7}$$

and the remaining terms have their usual meaning [7]. In this way, resistivity and scattering time can be obtained from the fitting routine, as given in equations (3.5) and (3.6).

One of the achievements in this work is building a model to be useful for tin oxide-based films with a wide range of conductivity, bandgap and thickness values. A multi-layer, multi-oscillator model was developed for large sets of films simultaneously.

The extracted parameters such as thickness, surface roughness and resistivity have been corroborated with measurements taken by other techniques. The optical functions have been built by simultaneously fitting the oscillator parameters for more than 50 films. To this end, we expect to have developed a reliable model for degenerate tin oxide based films, which can be used to extract thickness, roughness and electrical ("optical") conductivity quickly, non-invasively and non-destructively. The resulting model has proven reliable for 0-10% Zr in SnO_2:F as well as for CdO-SnO_2 and In_2O_3-based films. Typical mean square error (MSE) values are less than 5, and the measurement error for thickness and roughness is typically less than 1 nm, e.g. for films with $t \sim 500$ nm and $R_A \sim 10$ nm.

The advantages of using SE to obtain thickness measurements are due to its non-invasive nature and speed of measurement (less than 30 s to obtain a thickness value when using a previously developed model). However, as stated above, the need for an accurate model makes some measurements difficult. Further, simultaneous fitting of several parameters, such as the optical conductivity and scattering time, requires some skepticism. Correlations and coupling between fitting parameters may result in non-physical solutions, yet produce a "good fit" and low MSE values.

Hall and 4-probe Electrical Measurements

Accurate, repeatable measurements of the film's electrical properties such as sheet resistance, charge carrier concentration and charge carrier mobility, are essential to understand the effects of dopants, process parameters, film thickness, etc on the electrical properties. Quick measurements of the sheet resistance are routinely obtained using a linear four-point probe (4pp) station (Signatone) equipped with a high impedance current source set to inject 45.3 µA current, and a precision voltmeter which measures the induced voltage drop between the probes as shown in Figure 3.3 (Keithley Instruments). The advantages of the four probe method are that the measurements are quick, accurate to within a few percent, and the equipment is inexpensive and readily available. However, resistance is a function of thickness. Also, four-point probe measurements can not determine carrier type, carrier mobility or carrier density. Another disadvantage of the 4pp method is that the probes must touch the sample surface. In some cases this may be undesirable or even destructive. The use of an eddy current sheet resistance system is attractive in such cases. Eddy current sheet resistance systems are commercially available; some are even configured in conjunction with an ellipsometer for simultaneous non-contact measurement of thickness and sheet resistance.

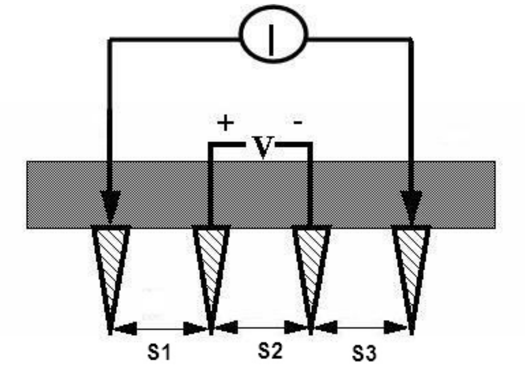

Figure 3.3. Schematic of a typical linear four point probe setup.

The 4pp has the arrangement shown in Figure 3.3. When an electric current is forced, the electric field E is measured (in the form of a voltage). The electric current is quantified by the current density J:

$$J = \sigma E \tag{3.8}$$

where the conductivity σ is the reciprocal of the resistivity ρ ($\sigma = 1/\rho$) [7, 8]. For a rectangular sample with thickness t, length l and width b, the resistance R is

$$R = \rho \frac{l}{bt} . \tag{3.9}$$

If the length and width are equal, $b = l$, this resistance is called the sheet resistance [8]

$$R = \frac{\rho}{t} = R_S . \tag{3.10}$$

The resistance of one square of film is defined as the sheet resistance. R_S is then independent of the size of that square.

In the linear four probe arrangement used, the resistivity is given by

$$\rho = \frac{V}{I} \cdot \frac{2\pi}{1/S1 + 1/S2 - 1/(S1+S2) - 1/(S2+S3)} \tag{3.11}$$

where *V* is the measured voltage (V) and *I* is the source current (A) [9, 10]. As in most linear 4pp setups, the spacings between adjacent probes are equal; that is, *S*=*S1*=*S2*=*S3*. Therefore, (3.11) simplifies to

$$\rho = \frac{V}{I} 2\pi S \tag{3.12}$$

For a thin film on an insulating substrate, (3.12) becomes [10, 11]

$$\rho = \frac{V}{I} \frac{\pi \cdot t}{\ln 2} \tag{3.13}$$

and the corresponding equation for sheet resistance is

$$R_S = \frac{\pi}{\ln 2} \frac{V}{I} \tag{3.14}$$

Equation (3.14) is only valid when the thickness of the probed layer (i.e. the TCO film on insulating glass) is less than half of the probing spacing, *S*, and the sample's lateral dimensions are much greater than *S* [12]. In this work the probe spacing is 1mm, and typical film thickness are about 2-3 orders of magnitude lower than the probe spacing. The sample size is typically 1 cm x 1 cm or greater.

Before each set of measurements, the current source and voltmeter are powered on and allowed to equilibrate for at least 30 minutes. To qualify the instrument, a TCO standard (Pilkington Tec15) was checked before each measurement session. The value of this standard was 13.5 Ω/□ ± 1 Ω/□ over a span of time greater than one year. This 4pp method enables fast, accurate estimates of the sheet resistance, with an estimated error of ± 5%. When compared to resistivity values obtained using a Hall instrument in the van der Pauw configuration (details below), the results from the four-probe measurement typically yield a value of approximately 1 Ω/□ larger than that obtained by the Hall instrument. This may be due to differences in calibration, the more careful nature of the Hall measurement, or to contact resistance between the probes and the film. Effects from contact resistance could result from the fact that for the 4-probe measurement, the 4 pins contact the film surface directly, while in the Hall/van der Pauw arrangement, ohmic contact pads are placed on the film surface (details below). Another possibility is that the measured Hall mobility is different than the actual mobility. Carrier scattering mechanisms which can impact carrier mobility are discussed in Chapter I.

When the thickness of a sample is known, the resistivity can be calculated from sheet resistance. The 2-dimensional sheet resistance [Ω/□] is related to the bulk resistivity [Ω·cm] by

$$R_S = \frac{\rho}{t} \tag{3.15}$$

where ρ is the (bulk) resistivity and t is the film thickness, which is obtained by either profilometer or ellipsometer measurements, or both.

Detailed analyses of the electrical properties were attained using commercial Hall stations at room temperature (BioRad HL5500) and at temperatures between 105K to 435K (Accent HL5550). All measurements were taken in the van der Pauw configuration on nominally 1 cm x 1 cm square samples [13]. A schematic of the Hall measurement is shown in Figure 3.4. The following description of the methods used and the instruments' operations follow the guidelines set by the American Society for Testing and Materials (ASTM) [14]. Ohmic contacts between the Hall probes and film surface were insured by fixing indium pads to the four corners. The measurement conditions are initially set with no applied magnetic field. The induced current was set such that the measured voltage between indium pads was in the range of 5 mV - 20 mV. In this way, the sheet resistance was again measured, and permutations of the applied current and measured voltage were averaged by 90º rotation of the sample. Further, the voltage is measured for current applied in both directions, and again averaged. This averaging eliminates effects due to anisotropy, inhomogeneity or thermoelectric effects.

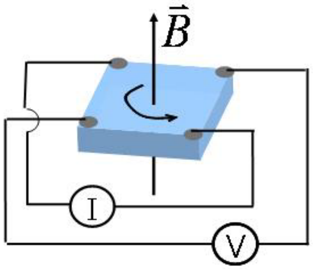

Figure 3.4. Diagram of the Hall effect measurement, illustrating the van der Pauw configuration with ohmic contacts placed at the corners.

In the Hall effect measurement using the van der Pauw configuration, a constant current, I, is applied across two non-adjacent contacts. With a constant magnetic field, B, applied normal to the surface of the sample, the potential difference, the Hall voltage, V_H, is measured across the remaining two contacts, allowing for all vector quantities to be replaced by scalars [15]. The Hall coefficient is calculated from the average of the four potential voltages measured with both directions of current and magnetic field. The charge carrier density is calculated from the Hall coefficient, R_H, by

$$R_H = \frac{V_H \cdot t}{I \cdot B} = \frac{1}{q \cdot n} \cdot S' \tag{3.16}$$

in which q is the elementary charge (*i.e.* $q = e = 1.602 \times 10^{-19}$ C for electrons for n-type material) and n is the carrier density (n_e) [15]. *S'* is the scattering factor which takes into account the mechanisms which scatter the charge carriers as well as the geometry of the scattering surface [13]. In practice, *S'* is close to and greater than unity ($S' \geq 1$) [8, 14, 15]. *S'* is set to unity for all Hall results presented in this dissertation. Thus our extracted carrier concentration is high and our extracted mobility is low, both by the factor *S'*. The sign of the Hall coefficient indicates the majority carrier type: positive for holes and negative for electrons. The Hall mobility, μ, is calculated from the Hall coefficient by

$$\mu = \frac{R_H}{\rho} \tag{3.17}$$

and we note that the calculated mobility is not dependent on sample geometry, nor is knowledge of the layer thickness required. The films produced in this study were all *n*-type, as indicated by the negative Hall coefficient, thus the carrier density is the ionized donor (electron) concentration.

The Hall measurement routine described above resulted in measurements with less than ± 5% deviation. However, straying from some steps may result in large errors [13, 14]. For instance, not using the indium contacts resulted in similar measured sheet resistance values, however, the mobility values obtained would often be a factor of 2 or 3 higher and not repeatable. Further, if the probes are placed closer to the center of the sample (i.e. away from the corners), the carrier concentration would systematically decrease, and could actually change sign for low mobility samples (see [13, 14] for an explanation of systematic error). Such observations have recently been attributed to some *p*-type behavior in TCOs [16].

Spectrophotometry

As discussed in Chapter I, the optical response of a TCO film is highly dependent on the electrical properties (and *vice versa*). As such, analysis of the optical transmittance and absorptance of films is critical to analyzing the doping or alloying effects with respect to, *e.g.*, carrier concentration, mobility, and, as is critical for this study, the permittivity. Further, as was shown earlier, changes in carrier concentration may manifest in a bandgap shift which should be evident by optical measurements [17, 18]. Further, alloying tin oxide with a wide gap material would imply a bandgap widening as well.

Total transmittance and reflectance are measured with the incident beam normal (off normal angle of incidence, $\theta_i = 0^\circ$ for transmittance, $\theta_i \sim 3^\circ$ for reflectance) to the sample surface (Cary Varian 5g or 6i) over a maximum spectral range of 180 nm to 2500 nm (Cary 5g) or 180 nm to 1600 nm (Cary 6i) in a double beam configuration. The light sources are xenon (UV) and tungsten lamps (vis-NIR), while the light is detected by a Si photodiode (UV-Vis) for wavelengths up to ~ 800 nm. The Cary 5g utilizes a PbS detector for wavelengths greater than ~ 800 nm which provides measurements with extended spectral range, but at the expense of relatively larger noise in the data and longer data collection times. The Cary 6i is equipped with InGaN detector for NIR light detection, which allows for relatively quick measurements with low noise, but narrower detection range than a PbS detection system as used in the Cary 5g. Both specular and diffuse light are collected simultaneously by means of an integrating sphere (LabSphere). A NIST-traceable, diffuse reflectance standard is used for baseline correction before each set of measurements (Labsphere Spectralon). All data are referenced to air and not the substrate. That is, the effect of the glass substrate is included in all data reported, unless specified differently.

From the measured transmittance, T, and reflectance, R, the absorptance, A, is calculated by

$$\mathrm{A} = 100 - T - R \tag{3.18}$$

and the absorption coefficient, α, is calculated from

$$\alpha = \frac{1}{t} \ln \frac{(1-R)^2}{T} \tag{3.19}$$

where t is the film thickness [19, 20]. The absorption coefficient is related to the bandgap energy, E_G, by [19]

$$\alpha(hv) \propto \sqrt{E - E_G} \tag{3.20}$$

Hence, the bandgap energy can be obtained by extrapolation to zero α of the linear portion of a plot of $[\alpha(hv) \cdot hv]^2$ versus hv [19]. Note that there is a rigorous distinction between *absorptance* (%A) as defined in (3.18), which is necessarily calculated from *both* transmittance *and* reflectance data, and *absorbance* which is calculated from transmittance (%T) by [20]

$$Absorbance = \log_{10} \frac{1}{T} \tag{3.21}$$

Unfortunately, in the literature, the terms absorptance and absorbance are often used interchangeably, and inevitably, at times incorrectly [21]. The software for many spectrophotometers provide an option for viewing (and exporting) data in “transmittance mode” or “absorbance mode” mode, the latter making use of (3.21).

In the present work, data taken as described above was reproducible to within approximately 1%. However, even when using a “small spot” (~ 1mm x 3mm), it is critical that the sample be uniform in thickness, composition and in electrical properties, in order to obtain a meaningful analysis. In this work, the samples should be fairly uniform over a 1-2 mm length at least, and so were aligned such that any degree of nonuniformity expected would be in the short direction of the beam.

X-ray Photoelectron Spectroscopy

Analysis of the composition of the films is needed to understand the relationships between process parameters and film properties. X-ray photoelectron spectroscopy (XPS) analysis can give detailed insight of the composition and chemical bonding at the near surface region of a film [22, 23]. Since a primary goal of this study is to understand how additions of dopants (fluorine) and cationic alloys (zirconium oxide) affect the films’ electro-optical performance, understanding of compositional data is vital.

XPS is a surface analysis technique useful for quantitative measurements of chemical and electronic state and element composition, though XPS cannot detect hydrogen or helium [24]. From data of electron attenuation length versus photon energy, the escape depth for the photoelectrons in the current setup is estimated at approximately

6 nm [24, 25]. In practice, the sample surface is irradiated with a soft X-ray beam typically with energy on the order of keV. Emitted photoelectrons are collected and their kinetic energy analyzed as shown in Figure 3.5 [26]. Of interest for chemical state analysis is the binding energy, *B.E.*, which is calculated from the incident photon energy and the measured kinetic energy, *K.E.*, by

$$B.E. = h\nu - K.E. - \varphi \tag{3.22}$$

where φ is the work function of the analyzer [27].

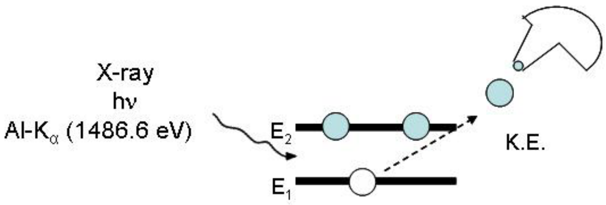

Figure 3.5. Schematic of an XPS setup using Al-*Kα* X-rays and a hemispherical electrostatic energy analyzer.

Compositional and chemical state analysis of the films was determined by XPS (Phi 5000 VersaProbe) using monochromatic Al-*Kα* X-rays. Survey scans were taken with a pass energy of ~ 100 eV, while high resolution scans of individual peaks were taken over several iterations at a pass energy of 23.5 eV, resulting in an overall resolution of ~ 0.5 eV. Electrons were collected at 45˚ from sample normal. XPS determines oxygen and fluorine stoichiometry (anion ratio), as well as Zr and Sn atomic% (cation ratio) down to < 1% [24]. Atomic sensitivity factors from the PHI handbook, listed in Table 3.1, Gaussian/Lorentzian peak fitting and Shirley background subtraction were used for stoichiometry estimation and chemical state analysis [28]. The data are analyzed using commercial software (PHI MultiPak, CasaXPS).

Table 3.1. The atomic sensitivity factors (ASF) for elements of interest [28].

Element	**Orbital**	**ASF**
F	1s	1.00
O	1s	0.63
C	1s	0.21
Sn	3d-5/2	3.20
Zr	3d	0.87

X-ray Diffraction

As discussed in Chapter I, it is often reported that electrical and/or optical performance is intimately linked to structural quality. The effects of doping and alloying may have profound effects on the crystal structure, crystallinity, stress and texture of a film. X-ray diffraction (XRD) is used to identify crystalline phases and structural properties on select groups of samples in this study to ascertain whether trends may be observed between, for example, alloying concentration and crystal properties.

The structure patterns of the films were obtained from XRD (Scintag PTS) in the θ-2θ mode with 0.02° step size. Cu-$K\alpha$ X-rays were emitted from the anode operating at 45 kV at 36 mA. In this configuration, the sourced is fixed, while the sample and detector move along positions θ and 2θ, respectively, as displayed in Figure 3.6. In general, the penetration depth for Cu-$K\alpha$ X-rays into SnO_2 is estimated to be ~ 3-5 µm

[29]. Therefore, for films having thicknesses ranging from 100-2000 nm, it is expected that a contribution from the substrate would be evident in the XRD spectra. However, the data reported here are for films supported on amorphous glass substrates, which only contribute slightly to the background counts, particularly at smaller angles.

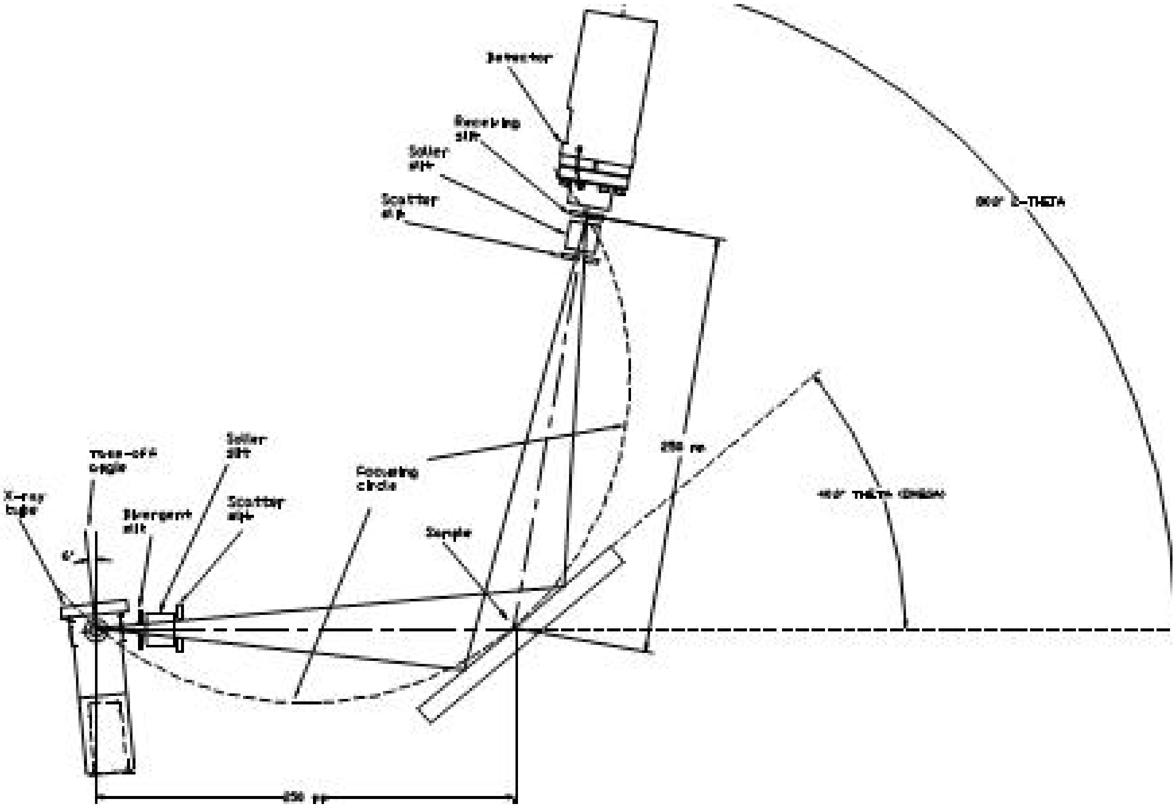

Figure 3.6. The schematic for the Scintag XRD operated in *θ-2θ* mode [30].

Estimates of the crystal structure, texture, stress, grain size and interplanar lattice spacings may be obtained from XRD spectra. The incident X-ray beam is diffracted upon interaction with the sample. Only those beams which interfere constructively are reflected back to the detector. The criteria for constructive interference is given by Bragg's law in the form of

$$n\lambda = 2d\sin\theta \tag{3.23}$$

where n is an integer; the wavelength, $\lambda = 0.15418$ nm for Cu-$K\alpha$ X-rays; d is the interplanar lattice spacing (see Figure 3.7); and θ is the angle determined by the source-sample-detector geometry as shown in Figure 3.7 [7].

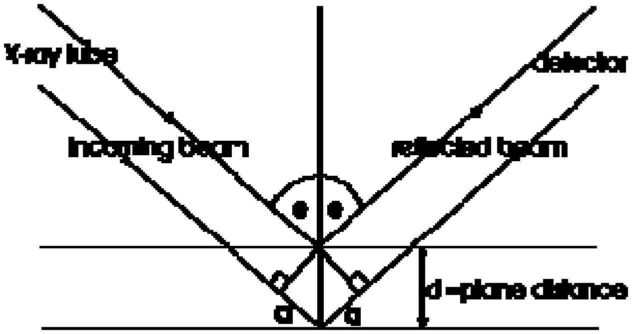

Figure 3.7. Diagram of incident and reflected X-ray beam, defining the lateral interplanar lattice spacing, or *d* spacing [7].

The texture coefficient quantitatively indicates the degree to which a particular orientation is present in a film and is calculated by

$$TC[hkl] = \frac{I[hkl]/I_o[hkl]}{{N_R}^{-1}\sum_{N_R} I[hkl]/I_o[hkl]} \tag{3.24}$$

where *I[hkl]* is measured intensity from the sample and $I_0[hkl]$ is the intensity obtained from standard card files from the Joint Committee on Powder Diffraction Standards (JCPDS) [31]. If *TC[hkl]* is less than 1, the film is randomly orientated in the [hkl] direction. If *TC[hkl]* is larger than 1, the film is preferentially orientated in the [hkl] direction. Presentation of data with pronounced differences in *TC* is presented in later chapters.

The mean crystallite size, *l*, is estimated from the full width at half maximum (FWHM) of dominant peaks in the XRD spectrum using Scherer's equation:

$$l = \frac{K \cdot \lambda}{\cos\theta \cdot \Delta(2\theta)} \tag{3.25}$$

where $\lambda = 0.15418$ nm for Cu-$K\alpha$ X-rays, θ is the angle of incidence and $\Delta(2\theta)$ is the FWHM of the peak at the angle θ [32]. The *K* factor in (3.25) is taken to be 1.05, which assumes a spherical crystallite shape [6, 32]. From (3.25) it is evident that crystallite size decreases as the peak broadens. The mean crystallite size is often indicative of, but may be smaller than, the actual grain size; this ambiguity is not distinguished by XRD analysis alone. Therefore, only qualitative information (e.g. trend of increasing or decreasing "grain size") is reported. Furthermore, broadening of the FWHM is actually a convolution of instrument broadening and sample broadening. The instrumental broadening is accounted for by identifying the instrumental profile through use of standards; further, instrument broadening can be neglected for particle sizes ≤ 100 nm [33]. The broadening of the FWHM from the sample, however, is an additional convolution of broadening due to both crystallite size and microstrain broadening. Both crystallite size and microstrain broadening are most pronounced at large angles.

However, if the broadening of peaks varies with [*hkl*], then the microstrain broadening is likely due to antiphase domain boundaries, also known as crystallographic shear planes [33]. This distinction may be relevant to data presented in later chapters.

Atomic Force Microscopy

Examination of the surface morphology and estimates of surface roughness were carried out using atomic force microscopy (AFM). Important materials properties correlations can be ascertained by comparing trends in, for example, surface roughness and alloying composition. These morphology properties may provide insight into their relation with electro-optical performance, which can be fed back into tuning process parameters.

The AFM data are taken at ambient pressure and room temperature in tapping (AC) mode using a crystalline Si tip (Jeol JSPM-5200). The tip is attached by cantilever and rastered laterally across the film surface. A laser detects reflection from the cantilever to estimate the interaction force between the surface and the AFM tip, which is then used to calculate surface features; in this way a topographical image of the surface is displayed. The roughness reported from data collected by AFM is typically root mean square (*rms*) roughness. Following Song's method, it is noted that the *rms* roughness, R_{rms}, is defined as approximately half that of the surface roughness layer thickness, R_A, as defined by ellipsometry analysis [4, 34]. These definitions are shown pictorially in Figure 3.8, following [34]. The differences in roughness values obtained by AFM and SE are compared in the forthcoming chapters.

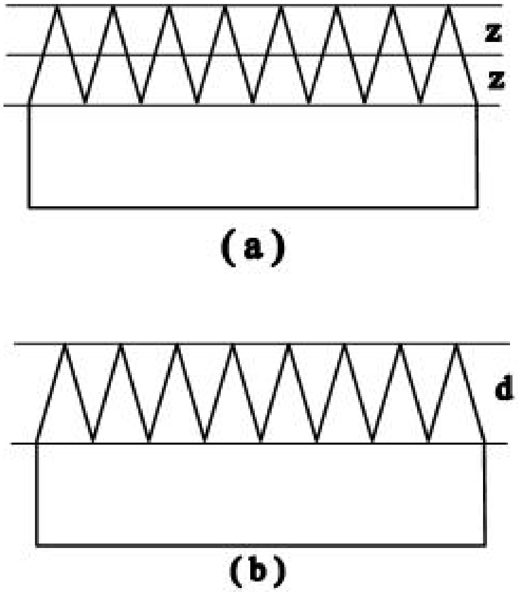

Figure 3.8. Schematic diagram which indicates what defines surface roughness in (a) AFM and (b) SE [34]. Note that the *rms* roughness values (the “z” height) extracted from AFM are approximately half that of the thickness of the roughness layer, as determined by SE.

References

1. Tompkins, H.G., *Spectroscopic Ellipsometry and Reflectometry: A User' Guide*. 1999: Wiley-Interscience.

2. Azzam, R.M.A. and N.M. Bashara, *Ellipsometry and Polarized Light*. 1988: North Holland.

3. Jenkins, F.A. and H.E. White, *Fundamentals of Optics*. 4th ed. ed. 1981: McGraw-Hill.

4. Song, Z., B.R. Rogers, and N.D. Theodore, *Spectroscopic Ellipsometry Characterization of Zro2 Films on Si(100) Deposited by High-Vacuum-Metalorganic Chemical Vapor Deposition.* Journal of Vacuum Science & Technology A, 2004. **22**(3): p. 711-718.

5. JAWoollam, *Wvase Manual.*

6. Duenow, J.N., *Phd Thesis*. 2008, Colorado School of Mines.

7. Ashcroft, N.W. and N.D. Mermin, *Solid State Physics*. 1976: Thomson Learning, Inc.

8. Hartnagel, H.L., A.L. Dawar, A.K. Jain, and C. Jagadish, *Semiconducting Transparent Thin Films*. 1995, Philadelphia: IOP Publishing Ltd.

9. A., U., The Bell System Technical Journal, 1955. **34**: p. 105.

10. Valdes, L.B., Proc. IRE, 1954. **42**: p. 420.

11. Gessert, T.A., *Phd Thesis*. 1996, University of Wales, College of Cardiff.

12. Schroeder, D.K., *Semiconductor Material and Device Characterization*. 1990: Wiley.

13. van der Pauw, L.J., *A Method of Measuring Specific Resistivity and Hall Effect of Discs of Arbitrary Shape.* Philips Research Reports, 1958. **13**: p. 1–9.

14. ASTM, *Standard Test Methods for Measuring Resistivity and Hall Coefficient and Determining Hall Mobility in Single-Crystal Semiconductors*, in *ASTM Designation F76*. 2000: Annual Book of ASTM Standards.

15. BioRad, *Hl5550 Hall System User Manual.*

16. Bierwagen, O., T. Ive, C.G. Van de Walle, and J.S. Speck, *Causes of Incorrect Carrier-Type Identification in Van Der Pauw-Hall Measurements.* Applied Physics Letters, 2008. **93**(24): p. 3.

17. Moss, T., *The Interpretation of the Properties of Indium Antimonide*, Proc. Phys. Soc., 1954. **67B**: p. 775.

18. Burstein, E., *Anomalous Optical Absorption Limit in InSb*, Phys. Rev., 1954. **93**: p. 632.

19. Pankove, J.I., *Optical Processes in Semiconductors*. 1971: Dover Publications, Inc.

20. Williams, C.S. and O.A. Becklund, *Optics for Engineers and Scientists*. 1974, New York: Wiley-Interscience.

21. Kumar, B.S. and V.S. Raja, *Comment On: "Correlation between the Optical and Electrical Properties of CdO Thin Films Deposited by Spray Pyrolysis".* Thin Solid Films, 1996. **274**(1-2): p. 1-2.

22. Henderson, M.A., C.L. Perkins, M.H. Engelhard, S. Thevuthasan, and C.H.F. Peden, *Redox Properties of Water on the Oxidized and Reduced Surfaces of CeO_2(111).* Surface Science, 2003. **526**(1-2): p. 1-18.

23. Batzill, M., J.M. Burst, and U. Diebold, *Pure and Cobalt-Doped SnO_2(101) Films Grown by Molecular Beam Epitaxy on Al_2O_3.* Thin Solid Films, 2005. **484**(1-2): p. 132-139.

24. Briggs, D. and M.P. Seah, *Practical Surface Analysis: Auger and X-Ray Photoelectron Spectroscopy*. 1992: Wiley.

25. Henke, B.L., E.M. Gullikson, and J.C. Davis, *X-Ray Interactions: Photoabsorption, Scattering, Transmission, and Reflection at E=50-30000 Ev, Z=1-92.* Atomic Data and Nuclear Data Tables, 1993. **54**(2): p. 181-342.

26. Woodruff, D.P. and T.A. Delchar, *Modern Techniques of Surface Science*. 1986: Cambridge.

27. Plummer, E.W. and W. Eberhardt, *Advances in Chemical Physics*. 1992: Wiley.

28. Moulder, J.F., W.F. Stickle, P.E. Sobol, and K.D. Bomben, *Phi Handbook of Photoelectron Spectroscopy*. 1992: Perkin-Elmer Corp.

29. NIST, *Http://Physics.Nist.Gov/Physrefdata/Xraymasscoef/Tab3.Html*.

30. Scintag, *Scintag Manual: Ch. 7 - Basics of X-Ray Diffraction*. 1999.

31. Gurumurugan, K., D. Mangalaraj, and S.K. Narayandass, *Structural Characterization of Cadmium-Oxide Thin-Films Deposited by Spray-Pyrolysis.* Journal of Crystal Growth, 1995. **147**(3-4): p. 355-360.

32. Cullity, B.D., *Elements of X-Ray Diffraction*. 1978: Addison Wesley.

33. Guineir, A., *X-Ray Diffraction in Crystals, Imperfect Crystals, and Amorphous Bodies*. 1994, New York: Dover Publications.

34. Song, Z., *Phd Thesis*. 2005, Vanderbilt University.

CHAPTER IV

SYNTHESIS AND PROPERTIES OF CVD SnO_2-ZrO_2 THIN FILMS

SnO_2, ZrO_2 and SnO_2-ZrO_2 thin films were produced by low pressure metal-organic chemical vapor deposition and their properties evaluated in the context for potential use as transparent electrodes in thin film photovoltaic cells. The dense films have high visual transparency, > 80%, good adherence to the glass substrate, and their optoelectronic properties are environmentally stable. The ZrO_2 films are mostly amorphous, while the SnO_2 films are polycrystalline in the rutile (tetragonal) form with no significant texture. Fluorine-doping in the 1-3 at.% level induces a strong preferential [200] texture of the SnO_2 and SnO_2-ZrO_2 (up to 10 at.% Zr) films. Hall measurements show the n-type carrier concentration in the F-doped films is on the order of 10^{20} cm^{-3} with carrier mobility up to 30 $cm^2/V \cdot s$. The optical bandgap and near-infrared transparency of SnO_2 films increase with ZrO_2 addition.

Introduction

All thin film photovoltaic structures incorporate a transparent conductor as the top electrode. This top electrode is typically a transparent conducting oxide (TCO) based on the following oxides: cadmium oxide (CdO); indium oxide (In_2O_3, IO); tin oxide (SnO_2, TO); and zinc oxide (ZnO). Of these, the three latter oxides are most commonly used in research and industrial devices. Indium oxide alloyed with up to about 10% tin oxide, termed ITO, is widely used in the flat panel display (FPD) industry. ITO historically has demonstrated the best compromise between optimal electrical and optical performance, and is thus used in the highly performance driven application of the FPD industry. Tin oxide doped with fluorine (FTO) or antimony (ATO) have long been studied as TCO materials. In particular, FTO coated glass represents a large and growing market for the building trades (fenestration, thermal and solar control coatings), automotive and aerospace windows, and thin film PV. ZnO-based TCOs are typically doped with aluminum (termed AZO) and finds use in PV applications which require near room temperature deposition of the TCO coating. Importantly, however, we note that the ternary alloy cadmium stannate (Cd_2SnO_4) has exceptional optoelectronic properties and was utilized as the TCO contact in the world record efficiency CdTe solar cell [1].

The results from the synthesis and characterization of the constituent, alloyed, and doped films are presented and discussed in this chapter. Tin oxide (undoped, TO) films and their application in thin film PV are discussed. F-doped tin oxide (FTO) films are discussed next and important material properties and optoelectronic performance aspects are detailed. Next, the results for depositions of zirconium oxide are given. Briefly, results from the addition of fluorine-doping of zirconia are discussed. Finally, the combined system of fluorine-doped tin oxide alloyed with zirconium oxide (for Zr concentration up to ~ 10 at.%, termed FTZO) is thoroughly examined.

Experimental Details

The description of the CVD reactor and process parameters are fully described in Chapter II. The characterization tools and techniques are thoroughly presented in Chapter III. A brief overview is given here for completeness.

The CVD system is a modified low pressure metalorganic (MO) CVD reactor (CVD Equipment Corp), as shown in Figure 4.1 [2]. The reactor is a cold wall quartz tube design with 4 gas inlet injectors. Chamber and MO precursor pressures are independently monitored by capacitance manometer gauges (MKS Baratron). Ultra-high purity (UHP) O_2 is the oxidant and N_2 is the carrier and diluent gas. Precursor, diluent and reactant gases enter the chamber through their respective injectors, flowing the length of the chamber and are then pumped at the other end. The graphite susceptor is machined for sample sizes up to 10 cm wide x 30 cm in length and 1.1 mm thickness. The sample is heated from below by 5-zone independently controlled IR lamps. The substrates used in this study are 1 mm thick, 10 cm x 10 cm square, Corning 1737 aluminosilicate glass. The substrates were cleaned as follows. Individual slides are loaded into a Fluoroware spin-rinse-dryer (SRD) compatible carrier. These are soaked in a dilute Liquinox + 20 MΩ de-ionized (DI) water solution at 80°C for approximately 2 hours, then sonicated for 5-10 min. They are manually rinsed and sonicated up to 5 more times, then rinsed and dried in a cleanroom spin-rinse dryer to output resistance of 12 MΩ.

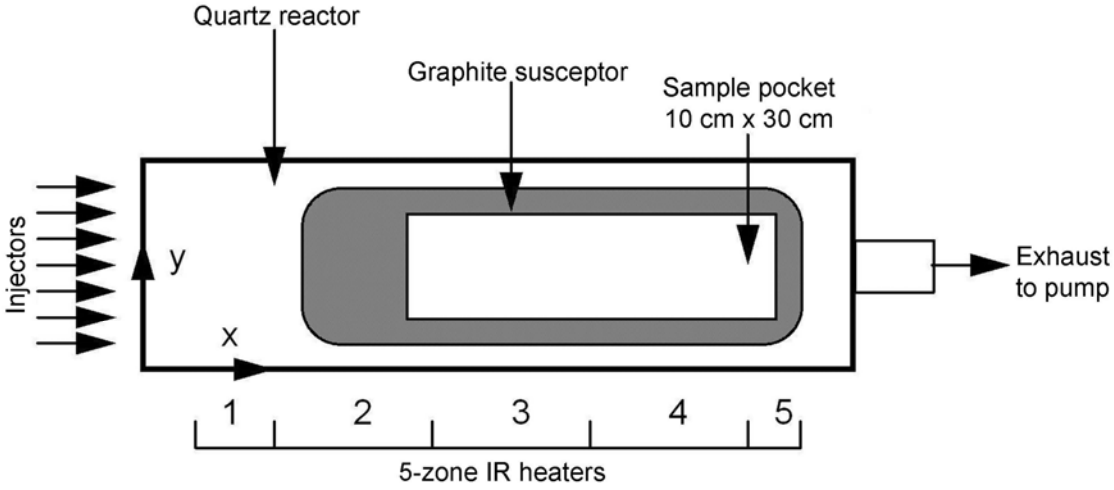

Figure 4.1. Diagram of the CVD reactor showing gas flow direction, sample area and heating zones.

The precursors are liquid at room temperature. The metal organics (MO) used are tetramethyltin (TMT, Air Products) and zirconium tert-butoxide (ZTB, Air Products). Bromotrifluoromethane ($CBrF_3$, Mattheson Tri-Gas) is the fluorine dopant source. Gaseous MO precursors were delivered by controlling N_2 carrier gas with mass flow controllers (MFCs), which was bubbled through the respective sources. The outlet pressures of the bubblers are 200 Torr and 80 Torr for TMT and ZTB, respectively.

Composition and chemical state analysis of the films was determined by x-ray photoelectron spectroscopy (XPS, Phi 5000 VersaProbe) using a monochromated Al-Kα source anode. Survey scans were taken with a pass energy of ~ 100 eV, while high resolution scans of individual peaks were taken over several iterations at a pass energy of 23.5 eV resulting in an overall resolution of ~ 0.5 eV. The data were analyzed using commercial software (Phi MultiPak, CasaXPS). The structure of the films was obtained from x-ray diffraction (XRD, Scintag PTS) in the θ-2θ mode with 0.02º step size.

The film thickness, surface roughness and optical parameters were acquired by modeling the data obtained from spectroscopic ellipsometry (J.A. Woollam M-2000 or α-SE) using Woollam's WVASE and CompleteEASE software, respectively. The 3-layer model consists of: glass substrate with backside reflection, a graded Drude-Lorentz model of the film's bulk properties, and a Bruggeman effective medium approximation (EMA) layer to model the surface roughness. The extracted thicknesses were compared to those obtained using a stylus profilometer (Dektak 8). The surface roughness obtained from SE is evaluated with respect to atomic force microscopy (AFM, Jeol JSPM-5200) measurements.

Spectrophotometer measurements (Cary Varian 6i) are used to obtain transmittance and reflectance spectra in the wavelength range of 250-1600 nm. From these, the calculated absorptance and absorption coefficient is evaluated for select sets of samples. The sheet resistance of conductive samples was routinely checked by a linear four-point probe. Further electrical analysis was performed using a commercial Hall system (Bio-Rad HL-5500) from which the carrier concentration and carrier mobility are ascertained.

Results for CVD of ZrO_2 Films

ZrO_2 films were deposited onto glass substrates at a total pressure of 20 Torr and the ZTB bubbler temperature was varied between 50 and 65ºC. The gas delivery lines were heated to ~ 80ºC to prevent condensation of the precursor between the bubbler and chamber,. The deposited films ranged in thickness of approximately 100-500 nm, associated with a thickness gradient along the length of the reactor. This gradient is evident in Figure 4.2 which plots the deposition rate versus reactor position. The deposition rate ranges from ~ 10 to about 1 nm/min along the length of the reactor. This is likely due to depletion of the precursor along the gas flow direction. Films with thickness values in the range 350-500 nm were selected for optical and structural analysis.

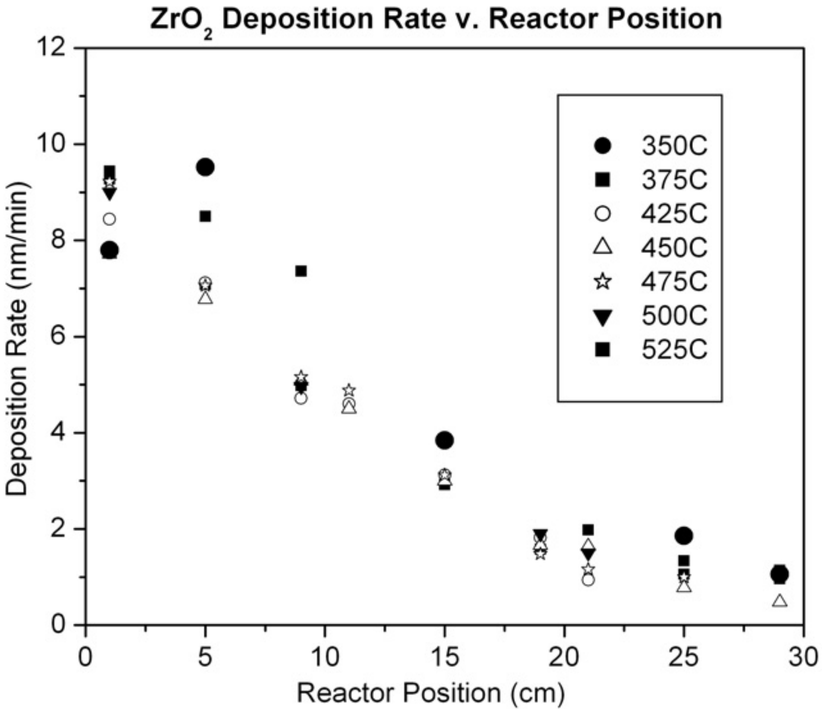

Figure 4.2. Deposition rate of ZrO$_2$ at various positions in the reactor. The decrease in deposition rate is due to depletion of the MO precursor along the gas flow direction.

Note that at 350-375°C the deposition rate is higher than at higher temperatures. However, as seen in Figure 4.3, the refractive index of the 350-375°C films is lower than that of the higher temperature films. The lower refractive index suggests that the films deposited at 350-375°C may be porous or contain impurities due to incomplete decomposition of the precursor. In Figure 4.4, the average optical transmittance in the visible region is 84% and 80% for the films deposited at 525°C and 350°C, respectively.

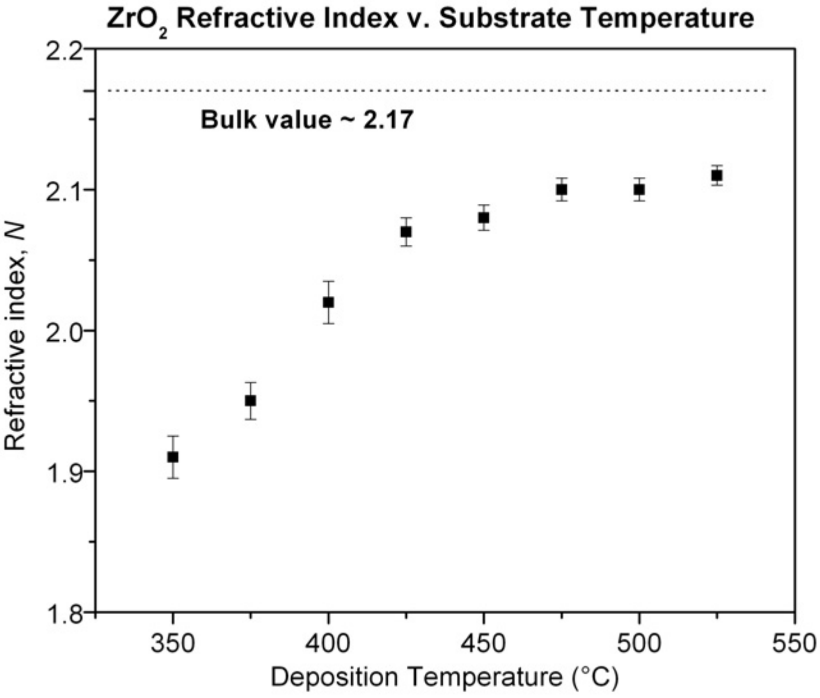

Figure 4.3. The real part of the refractive index, *N*, obtained from SE analysis for ZrO_2 films deposited at several temperatures. The refractive index increases with deposition temperature up to ~ 450˚C and levels off to a value $N \approx 2.1$, which is close to the bulk value of 2.17.

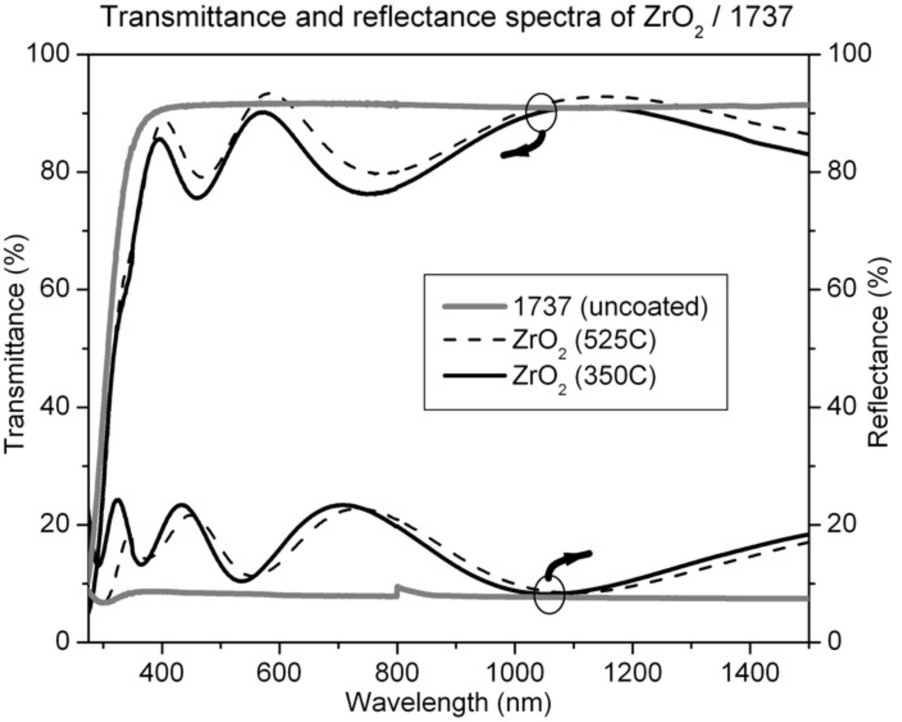

Figure 4.4. The optical transmittance and reflectance of ZrO_2 films deposited at 350˚C and 525˚C on Corning 1737 substrates. The data for the uncoated glass substrate is included for comparison.

Figure 4.5 includes XRD data for films deposited at substrate temperatures of 350˚C and 525˚C. The XRD spectra suggest that the ZrO_2 films are mostly amorphous, although peaks associated with mixed morphological phases are identified in the XRD spectra. For the low temperature film, a broad peak associated with tetragonal zirconia (200) is present. From the interplanar spacing, d_{200}, we calculate the lattice constant, a = 0.359 nm, which is close to the lattice constant for tetragonal ZrO_2 (a=0.364 nm, JCPDS card 42-1164). For the film deposited at 525˚C, the reflection peaks are sharper and the intensity is roughly twice that of the spectra for the film deposited at lower temperature. The spectra of the 525˚C film indicates that the film contains monoclinic, tetragonal and cubic phases. For the peak associated with cubic zirconia, d_{111} gives a calculated lattice constant, a = 0.513 nm from the experimental data compared to a = 0.5218 nm from JCPDS card 49-1642. Similar analyses are used to determine the phases associated with the resolvable peaks, and it is concluded that all peaks are associated with the three aforementioned polymorphs of ZrO_2. From the analysis of the experimentally determined lattice parameters, it is observed that there is 1% lattice contraction for the mixed-phase films compared to the reference data for single-phase powder samples. The contraction is an indication of stress, which could be due to several factors: structural mismatch of films with mixed phase deposited onto an amorphous substrate; deviation from stoichiometry; or thermal induced stress due to expansion coefficient mismatch between film and substrate.

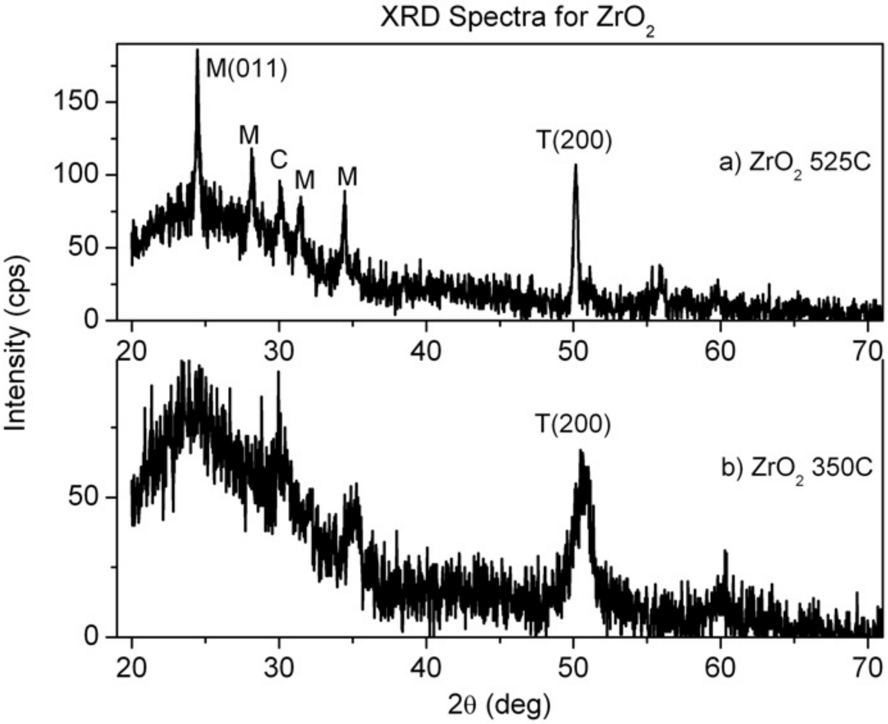

Figure 4.5. X-ray diffraction spectra for ZrO_2 films deposited at a) 525˚C and b) 350˚C. For the sample formed at higher substrate temperature, the diffraction peaks are relatively more intense and defined. All peaks are found to belong to ZrO_2 with a mixed morphology of monoclinic, tetragonal and cubic.

Figure 4.3 shows that the refractive index increases and approaches the bulk value with substrate temperature up to about 475ºC. This is likely due to a high void fraction resulting in lower density films at the lower temperatures, consistent with previously reported work [3]. The observance of higher-density phases in the XRD spectra supports this conclusion.

Peaks associated with oxygen, carbon and zirconium are evident in XPS spectra acquired from all of the films. Figure 4.6 is a representative XPS spectrum. XPS analysis indicates that films deposited at 350-375˚C contain a significant amount of carbon (~ 10 at.%) and the films are somewhat oxygen poor ($\sim ZrO_{1.7}$). Photoemission peaks consistent with ZrO_2 and Zr-C bonding are observed in the Zr-3d line shapes for a film deposited at 350˚C as shown in Figure 4.7. From this we conclude that at lower temperatures, the ZTB precursor, or a carbon-containing intermediate, adsorbs on the substrate more quickly than it can fully decompose and diffuse from the surface. The result is carbon incorporation into the film and poorer film quality. The unintentional incorporation of carbon may also explain the reduced optical quality of the films deposited at the lower temperatures.

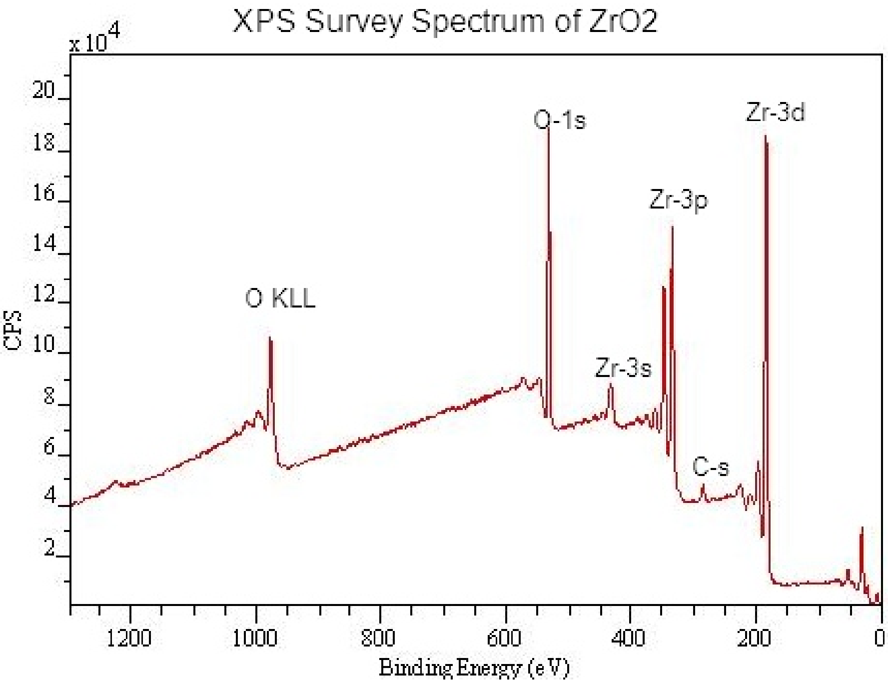

Figure 4.6. Representative X-ray photoelectron survey spectrum of CVD ZrO_2. Peaks associated with Zr, O, and C are identified. The unlabeled peaks at lower binding are identified with photoemission from the valence levels of Zr and O.

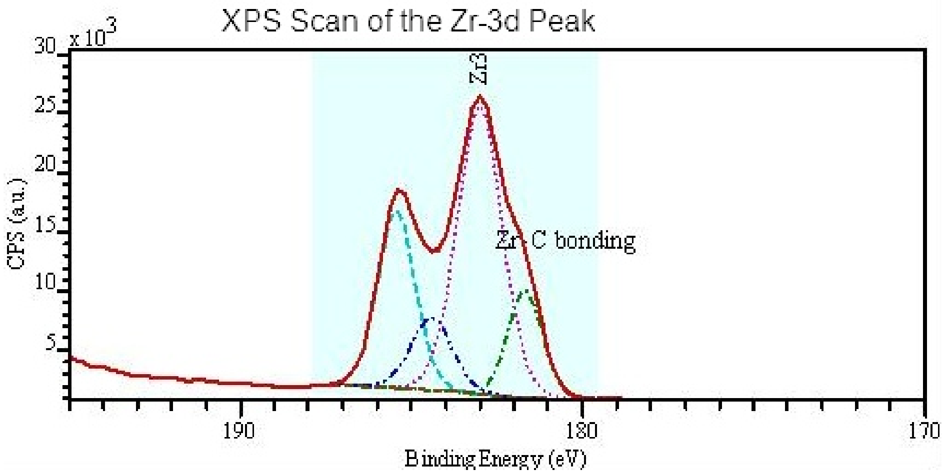

Figure 4.7. High-resolution XPS scan of the Zr-3d doublet photoemission peak. Two Gaussian-Lorentzian peaks are fit to the data associated with Zr-O and Zr-C bonding. A good fit is observed as evident by the overlap between the experimental and total fitted spectra.

For films deposited in the temperature range of 475-525°C, we detect what is probably adventitious carbon for the films analyzed without a sputter clean, however, after a 30-60 sec sputter clean, the C-1s peak is substantially reduced and not well-resolved given our experimental conditions (~0.5-1 at.% C after sputtering). We do note, however, that at these higher temperatures, material is deposited on the leading edge of the susceptor (sample holder), which is probably compensating for what might otherwise be an increase in observed deposition rate on the substrate which is ~ 5 cm downstream (due to depletion of precursor, consistent with the observed gradient in the deposition rate). At 550°C, continuous film deposition has ceased, and gas phase reactions occur. This is evident by small inclusions observed in the film. A powdery substance identified as ZrO_2 with carbon formed on the substrate holder. Based on our experimental results we conclude that ZrO_2 films deposited at temperaures between 475 and 525°C have the best optical, structural and compositional properties.

Results for CVD of ZrO_2:F Films

The fluorine precursor, $CBrF_3$, is added to the CVD process to examine whether fluorine may be incorporated into zirconia films. XPS analysis (Figure 4.8) indicates that the fluorine levels in the films increase with increasing flow rate for films formed at 350˚C. For bromotrifluoromethane flow rates of 300 sccm and 900 sccm, the anion percentage for fluorine in ZrO_2 is 1.5% ± 0.5% and 3% ± 0.5%, respectively, for films formed at substrate temperature of 350˚C. For a film deposited at 525˚C with 900 sccm $CBrF_3$ flow rate, the fluorine level is higher still at an estimated anion percentage level of 4.5% ± 0.5%.

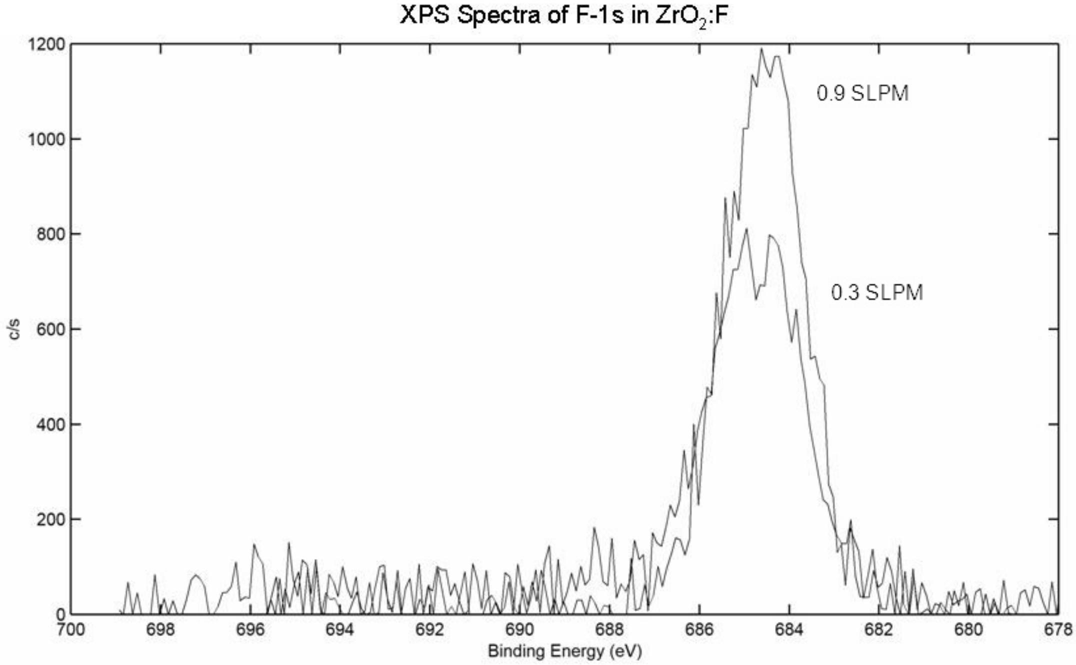

Figure 4.8. High-resolution XPS scan of the F-1s photoemission peaks in zirconia films deposited at 350C at different fluorine precursor flow rates: 0.3 SLPM (300 sccm) and 0.9 SLPM (900sccm). The data indicate fluorine incorporation into the films at 1.5% ± 0.5% and 3% ± 0.5%, respectively.

X-ray diffraction data for films formed with $CBrF_3$ flow rate set at 900 sccm and at deposition temperatures of 350˚C and 525˚C are given in Figure 4.9. Data for the undoped zirconia are included for comparison. We observe structural changes toward polycrystalline morphology for the films formed with fluorine addition. The structure evolves toward a monoclinic (020) texture as the fluorine level increases.

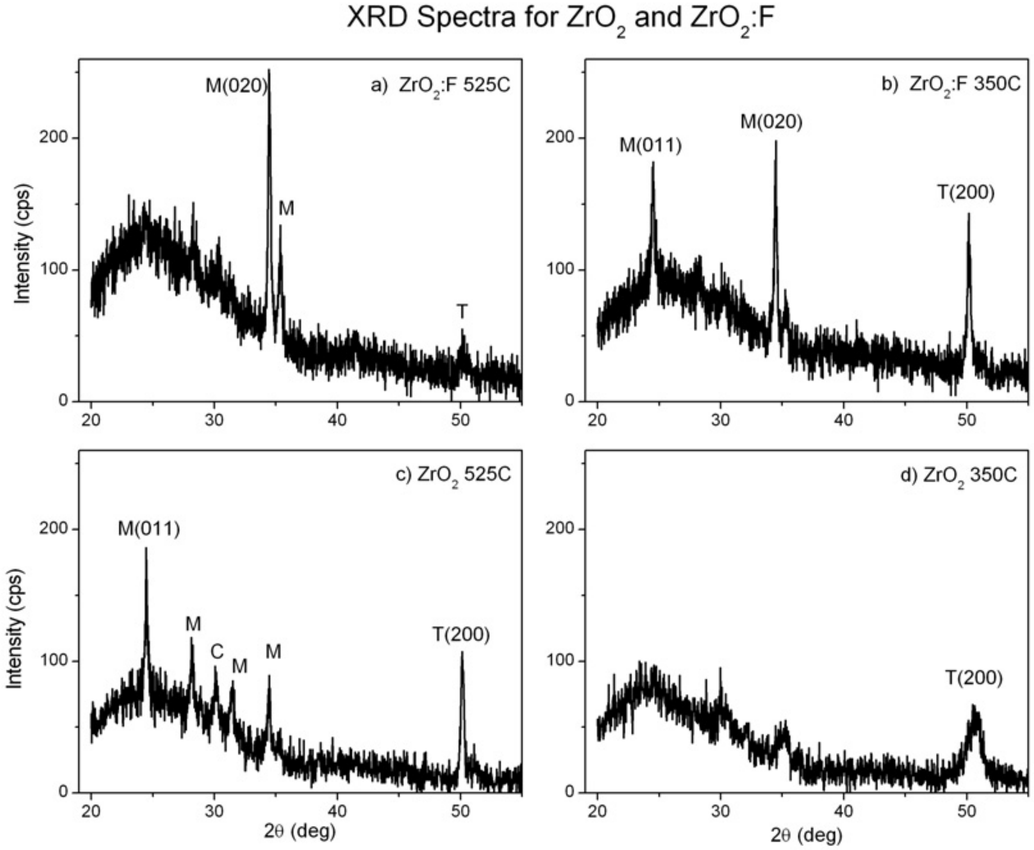

Figure 4.9. X-ray diffractograms for F-doped ZrO_2 films deposited at a) 525˚C and b) 350˚C, corresponding to F (anion) doping levels of 4.5 at.% and 3 at.%, respectively. Undoped ZrO_2 films deposited at c) 525˚C and d) 350˚C. No evidence for phases other than zirconia is observed.

Addition of fluorine precursor in the CVD process for zirconia films led to an observed ~10% decrease in the deposition rate. This could be related to the increased structure and tendency toward a single texture, as observed in the XRD analysis. That is to say, the polycrystalline grains for the F-doped films may grow at a reduced rate compared to the more amorphous structure of the undoped films. Another possible explanation for the decreased deposition rate is that byproducts or intermediates of the $CBrF_3$ precursor, such as HBr and HF, may etch the surface of the growing film. Such etching effects may also be related to the change in morphology. Indeed, preferential etching of amorphous versus polycrystalline grains, and *in situ* surface etching by halogens, is consistent with literature reports [4-7].

Zirconia coatings are often applied to materials to increase their corrosion resistance [8, 9]. Izumi *et al* reported on the corrosion behavior of steel sheets for various zirconia coatings applied by the sol-gel method [9]. They observe increased resistance to corrosion from water and water vapor for a ZrO_2-coated surface versus an uncoated steel sheet. Additionally, they report that the resistance is further enhanced when various fluorine precursors are included during film formation. They surmise that resistance to corrosion is linked to surface contact angle measurements, in which they demonstrate a positive correlation; the contact angle for the F-doped samples is approximately twice that of their standard ZrO_2-coated steel samples.

Results for CVD of SnO_2 Films

SnO_2 films were deposited at substrate temperatures between 500 and 550°C and resulted in deposition rates ranging from ~8-50 nm/min as shown in Figure 4.10. Deposition is not detected after a 10 minute process using a substrate temperature of 475°C in the pressure regime studied (20-45 Torr). Though the electrical and structural properties of the films did not change with pressure, the deposition rate was higher at 45 Torr and uniformity of the deposition rate, and thus film thickness, along the length of the reactor was achieved. Figure 4.11 illustrates Arrhenius plots for the depositions in the temperature region covered in this study. Apparent activation energies of 110 ± 7 kJ/mol and 105 ± 13 kJ/mol are extracted for depositions at 45 and 20 Torr total pressure, respectively. These values are within the range of those reported by others [10-15].

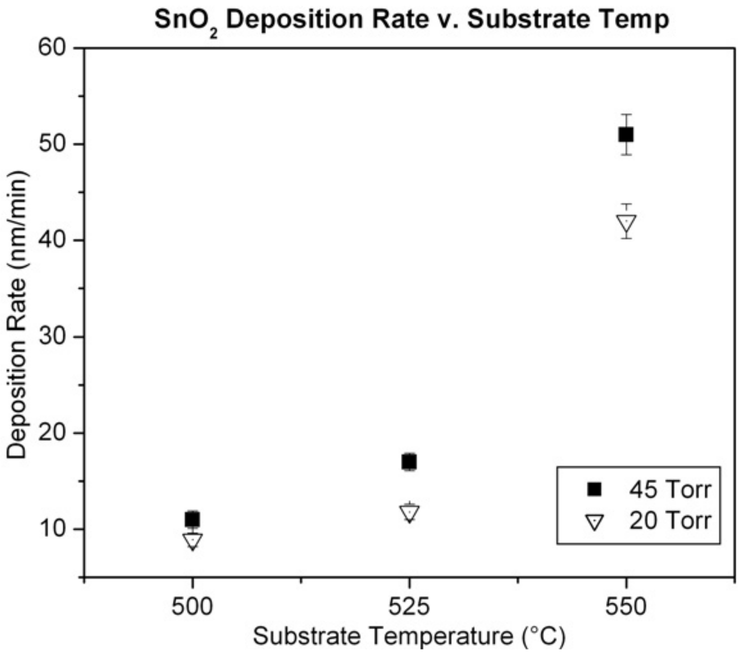

Figure 4.10. Deposition rate of CVD SnO_2 in the temperature range of 500-550˚C. Higher deposition rates are observed at 45 v. 20 Torr total pressure.

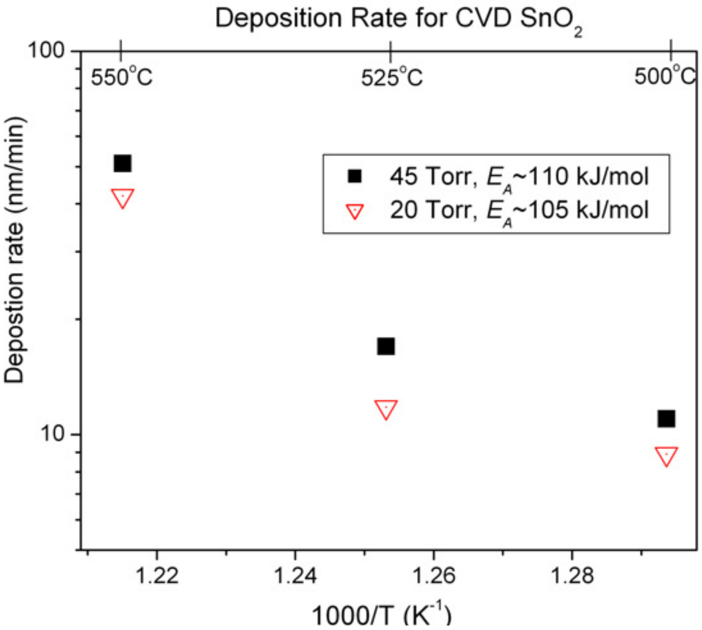

Figure 4.11. Arrhenius plot for the kinetically-limited CVD of SnO_2.

Unintentionally doped tin oxide is a weak n-type semiconductor previously reported to be due to H^+ inclusions, interstitial tin and/or oxygen vacancies leading to nonstoichiometric films [16-20]. The so-called intrinsic, or insulating, SnO_2 (i-SnO_2) films in this study are polycrystalline with a rutile (tetragonal) structure (see the next section for comparison to F-doped films). The films have an optical transmittance greater than 80%, a resistivity of similar to 1 $\Omega\cdot$cm and an optical bandgap of approximately 3.6 eV. Hall measurements confirm that these i-SnO_2 films are n-type, with carrier concentration $n = 3\cdot10^{18}$ cm^{-3}, and carrier mobility $\mu \sim 1\text{-}2$ cm^2/V·s.

Tin oxide films (or more generally, oxide films) which exhibit semiconducting electrical properties, such as these i-SnO_2 films, find use in advanced thin film PV devices [21]. In particular, thin film PV which utilize CdS as the n-type window layer must balance a tradeoff with regard to the CdS thickness. Shorting of the n-p interface (TCO to absorber layer) may occur for devices with thin CdS films as a result of pinholes or other defects in the CdS. These defects are mitigated for thicker CdS films, however, thicker CdS layers limit the photocollection in the blue spectral region due to the bandgap of CdS ($E_G \approx 2.3$ eV). Therefore, it is advantageous to incorporate a thin, ~ 100 nm, layer of a semiconducting transparent oxide between the TCO and CdS layers. For a film having a stable interface and with resistivity high enough to prevent shorting, yet low enough to not interfere with the sheet resistance of (i.e. collection by) the TCO, a thinner CdS layer (below 100 nm) may be used. To illustrate the effect of CdS thickness on the photocurrent available to reach the absorber, a plot of the transmittance spectra for film stacks consisting of CdS/i-SnO_2/SnO_2:F/glass with varying CdS thickness is shown in

Figure 4.12. A decrease in short-wavelength transmittance is observed as the thickness of the CdS is increased.

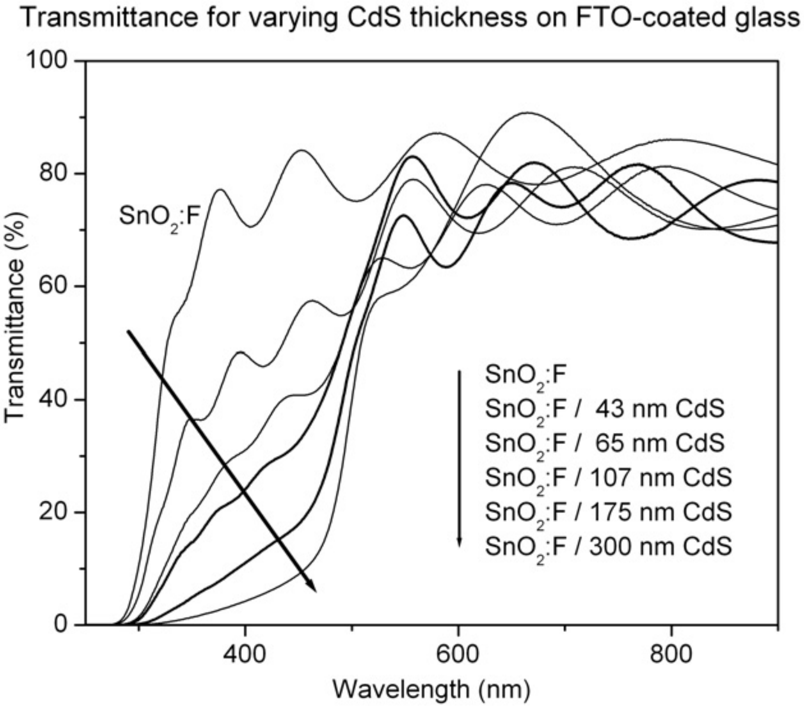

Figure 4.12. Transmittance spectra for films with varying CdS thickness. Decreased transmittance in the UV and blue region of the visible region is apparent for increasing thickness of the CdS layer, consistent with absorptance increasing due to the bandgap of CdS, $E_G \approx 2.3$ eV. The layers consist of CdS/i-SnO_2/SnO_2:F/glass. The tin oxide layer thicknesses are 100 nm and 500 nm, respectively.

It is important to note that (unintentionally-doped) tin oxide films formed from tin precursors which contain one or more halide ligands often contain a significant amount of impurities such as Cl [15, 19, 22]. These impurities act as donor centers and the resistivity of these films is thus about 2 orders of magnitude lower than those in this work. Consequently, films formed using such precursors have not been found to be suitable as a buffer layer in PV devices.

Results for CVD of SnO_2:F Films

The electrical and optical properties of tin oxide are heavily influenced by the addition of fluorine. Fluorine-doping of tin oxide increases both the carrier concentration, from $3 \cdot 10^{18}$ cm^{-3} to $4 \cdot 10^{20}$ cm^{-3}, and the carrier Hall mobility, from 1 cm^2/V-s to 25 cm^2/V-s. This results in a decrease in resistivity by nearly 4 orders of magnitude. Consequent to the increase in donors, which move the available optical transition levels up in the conduction band, the bandgap increases from 3.6 eV to 3.87 eV, for doped versus F-doped tin oxide, respectively.

XPS analysis indicates that the films generally exhibit a Sn:O ratio similar to 1:1.7. Quantification of the F-1s and O-1s spectra indicates that the F anion ratio is 1.5 ± 0.5 anion%. This doping level is equivalent to $1.3 \cdot 10^{21}$ atoms(F)/cm^3, which is much larger than the carrier concentration obtained from Hall measurements. This indicates that less than one-third of the incorporated fluorine atoms are electrically active in the tin oxide matrix. The inclusion of neutral impurities is generally undesirable; in a perfect crystal these only serve as scattering centers (and so termed neutral impurity scattering). However, from the electrical data, it is observed that the mobility *increases* (up to a point) with increasing carrier concentration (i.e. F incorporation). In polycrystalline material, “excess” impurities tend to reside at or near grain boundaries and other (point or line) defects [19, 23, 24]. This implies that the crystal structure, crystallinity and surface morphology may be impacted by F addition. For the present case, where the carrier mobility increases with F addition, it could be that F may passivate some mobility-limiting defects.

The change in the films' crystallographic structure and texture are evident in the XRD spectra shown in Figure 4.13. Both the TO and FTO are indexed to tetragonal (rutile) SnO_2 (JCPDS card 41-1445). This set of films was deposited at substrate temperature of 550˚C and to a thickness of about 500 nm. A large change in structure is observed: the TO sample appears to be predominantly [211] oriented with [301] and [110] directions also clearly identified; in contrast the FTO sample is strongly [002] oriented with weak reflections corresponding to [310] and [110] observed. Such a change toward [002] texture by F-doping has been observed by others [19, 23]. The texture coefficient quantifies the extent to which a particular crystallographic orientation is favored and is calculated from

$$TC[hkl] = \frac{I[hkl]/I_o[hkl]}{N_R^{-1}\sum_{N_R} I[hkl]/I_o[hkl]} \tag{4.1}$$

where $I[hkl]$ is the measured intensity of [hkl] from the film and $I_0[hkl]$ is the intensity obtained from standard card files of the Joint Committee on Powder Diffraction Standards (JCPDS) [25]. If $TC[hkl]$ is much less than 1, the film is considered randomly orientated. If $TC[hkl]$ is close to or larger than 1, the film is preferentially orientated in the [hkl] direction. Table 4.1 lists the texture coeffients calculated from the XRD spectra of Figure 4.13. The calculations indicate that the undoped tin oxide film has preferred texture (compared to a powder sample) for grains oriented in the [211] and [301] directions. In contrast, the FTO sample shows preferred texture for the [002] direction.

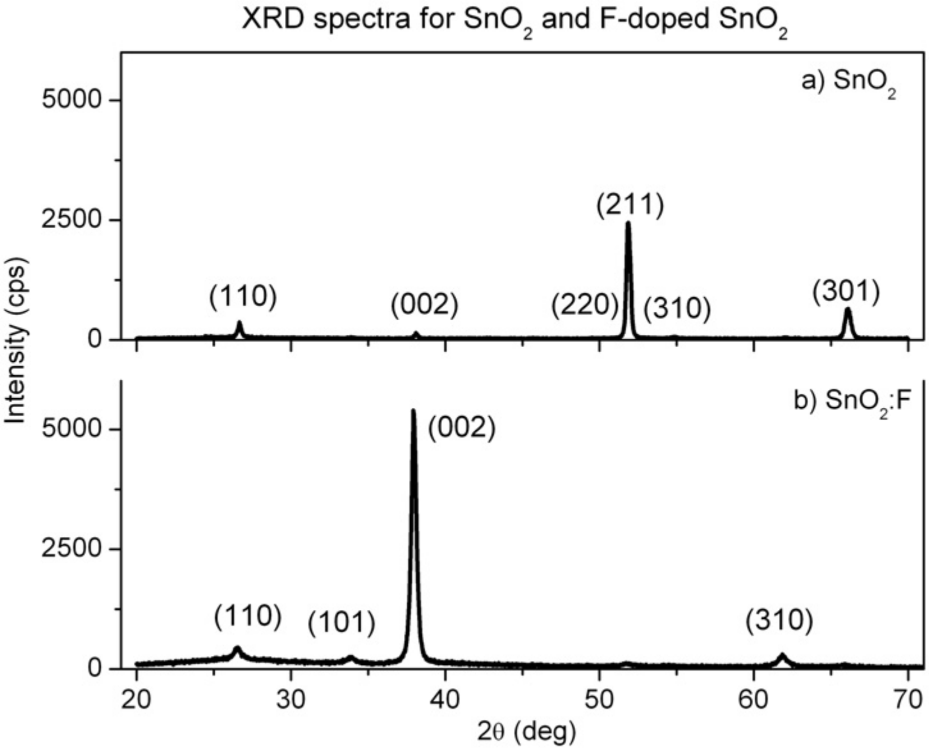

Figure 4.13. X-ray diffraction patterns referenced to tetragonal SnO_2 for a) undoped (TO) and b) F-doped tin oxide (FTO) films, indicating a strong change in crystal structure.

Table 4.1. The calculated texture coefficients for tin oxide and fluorine-doped tin oxide. The data are calculated from the XRD spectra in Figure 4.13 and referenced to JCPDS card 41-1445 for tetragonal SnO_2.

SnO_2 film	**TC[110]**	**TC[002]**	**TC[211]**	**TC[301]**
undoped	0.3	0.15	3.1	2.2
F-doped	0.15	3.7	0.01	0.1

In agreement with the structure data, we also observe that F-doping alters the morphology of the films. The surface morphology of TO and FTO films, as observed from AFM imaging, is shown in Figure 4.14. The values of average surface roughness extracted from AFM measurements and from the SE models are compared in Table 4.2.

The data from both sets of measurement techniques are consistent in that the undoped film has larger surface roughness than that for the F-doped film. Using the Scherer formula, values for the mean crystallite size, *l*, are calculated from the XRD spectra (Table 4.2) [26]. In agreement with the observed decrease in surface roughness, the average size of crystallites is smaller for the F-doped film.

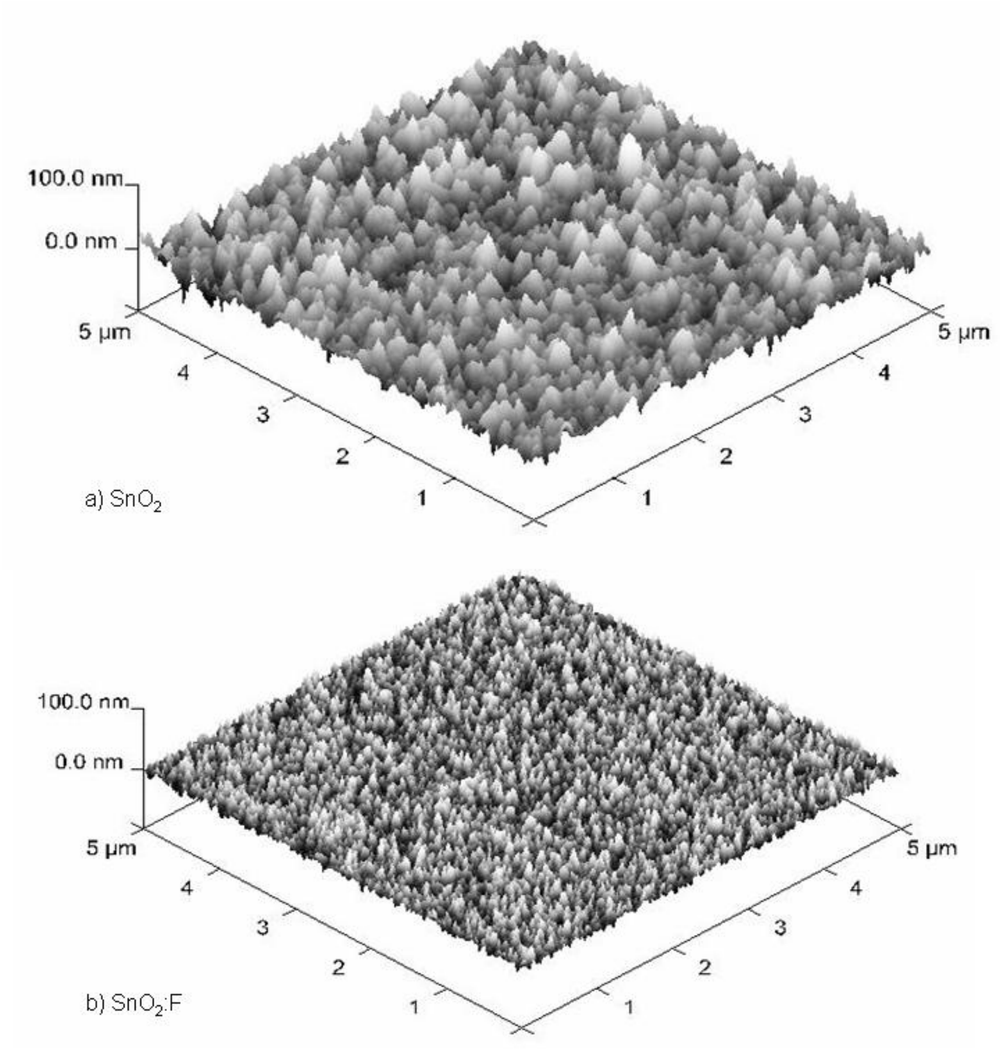

Figure 4.14. AFM images for a) undoped SnO$_2$ and b) F-doped SnO$_2$.

Table 4.2. Comparison of mean crystallite size obtained from analysis of X-ray diffraction (XRD) spectra, and of surface roughness obtained from spectroscopic ellipsometry (SE) analysis and atomic force microscopy (AFM) imaging for undoped and F-doped tin oxide.

SnO_2 film	**Surface Roughenss, R_A (nm)**		**Crystallite size, l (nm)**
	SE	**AFM**	
undoped	27	19	49
F-doped	15	11	31

We also observe broadening of the reflection peaks in the XRD spectra acquired from the undoped tin oxide. This broadening increases for peaks at higher diffraction angle. Such observations are consistent with the presence of crystallographic sheer planes (also called antiphase domain boundaries, APBs) [26]. The occurrence of APBs in thin films is a stress relief mechanism occurring between adjacent grains and is typified by a high defect density at the grain boundary [18, 26-29]. These defects could be related to tin interstitials, oxygen vacancies, hydrogen incorporation, or other complexes which lead to the observed high carrier concentration in undoped tin oxide [30]. The high APB density is likely responsible for the relatively low carrier mobility in undoped tin oxide. The data for the F-doped tin oxide does not indicate the presence of APBs, yet the (intentional) impurity level is high. Taken together that: i) the level of F incorporation is greater than the carrier concentration, ii) mobility increases with F incorporation, iii) XRD data indicate improved crystallinity upon F-doping, and iv) data suggesting the presence of APBs is observed in undoped tin oxide but not in the F-doped samples, we conclude that excess fluorine resides at grain boundaries (or similar defect sites) and decreases the defect sites' influence on the scattering of mobile charge.

To summarize the effects of F-doping on SnO_2, the greater than two orders of magnitude increase in charge carrier concentration induces an increase in the optical bandgap to ~ 3.87 eV, due to a blue shift in the transmittance spectra. This is explained in the context of the conduction band filling with ionized impurities due to degenerately doping, as explained by Burstein and Moss [31, 32]. This is discussed in further detail in Chapter I. The lowest resistivity for SnO_2:F (FTO) films observed in this study, $4.5 \cdot 10^{-4}$ $\Omega \cdot$cm, is achieved at a deposition temperature of 545˚C and flow rates of oxygen and fluorine precursors, F_{O2}/F_{CBrF3}, = 1.5, where the F-doping level is found to be 2% ± 0.5 at%. The associated carrier concentration and mobility, obtained from Hall measurements, are $4.5 \cdot 10^{20}$ cm^{-3} and 27 $cm^2/V \cdot s$, respectively. The increase in mobility upon fluorine addition may be associated with structural changes, exhibited by a significant increase in (200) texture of the F-doped films. F-doping promotes growth of tin oxide grains in the [002] direction.

Results for CVD of SnO_2-ZrO_2 Films

The results from the chemical vapor deposition studies of SnO_2 and ZrO_2 thin films, as described in previous sections, indicate a process overlap in deposition temperature (500-525°C) and total pressure (20-45 Torr). The zirconia depositions resulted in a thickness gradient in the gas flow direction, as discussed above, however, the tin oxide films are uniform with respect to thickness and electronic properties. Therefore, the combined process is a combinatorial synthesis of SnO_2-ZrO_2: each deposition yields a set of films in which all samples are identically processed, but the zirconia concentration in the films is linearly graded. The zirconia concentration gradient in a particular deposition is adjusted by the ZTB bubbler temperature, ZTB flow rate, or both. The zirconia concentration in SnO_2 and SnO_2:F (FTO) films is reported in cation %, in which the atomic ratios are determined by XPS analysis. Figure 4.15 shows that the lineshapes of the Zr-3d peak analyzed for the films containing in the range of 1-10 cat.% Zr are consistent with that from the ZrO_2 films presented earlier. The peaks are not shifted in binding energy and indication for multiple peaks is not evident. We consequently conclude that zirconium is present in the films as ZrO_2. Hence, this study offers the opportunity to test how the addition of a *high permittivity oxide* into tin oxide influences the optoelectronic properties.

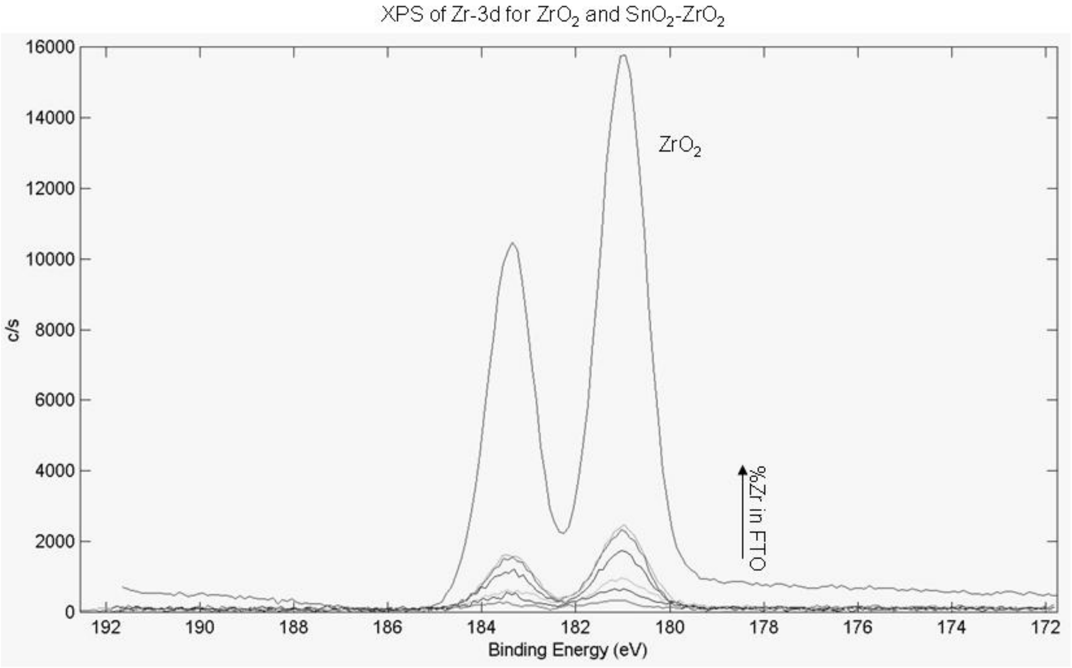

Figure 4.15. High-resolution XPS scan of the Zr-3d peak for ~ 1-10 at.% Zr in SnO_2. The scan from a ZrO_2 film is included which indicates that the Zr is present as ZrO_2 in the tin oxide films.

An example of the Zr:Sn concentration and film thickness variation across the reactor is shown in Figure 4.16. The relevant deposition parameters are: substrate temperature = 525˚C; total pressure is 20 Torr; ZTB flow and bubbler temperature is 30 sccm and 65˚C, respectively; $CBrF_3$ flow rate is 300 sccm. Ignoring the front edge of the samples, corresponding to the first few centimeters in the reaction region, the linearity of both the Zr concentration and the total film thickness is apparent. This linearity, observed in many runs, allows for useful comparisons to be made between sample sets and depositions.

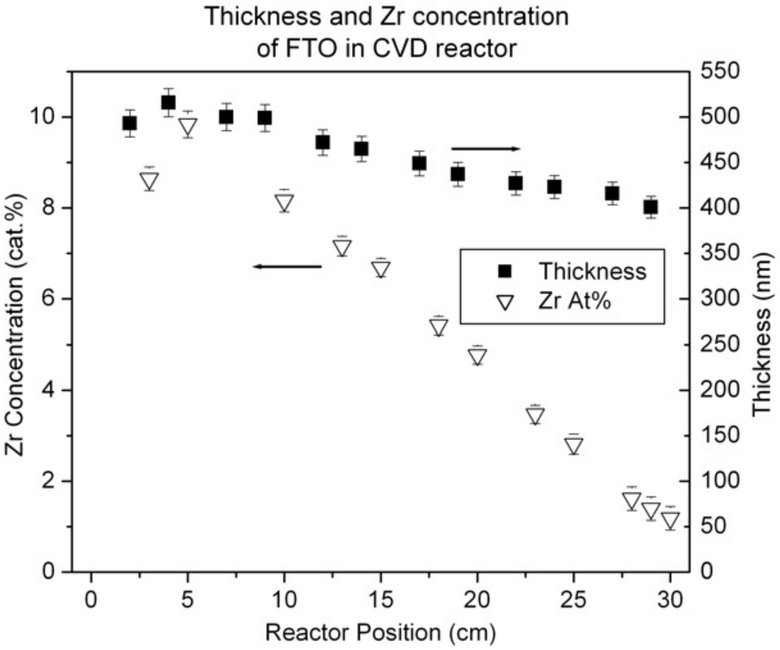

Figure 4.16. The concentration of Zr and the film thickness for various samples corresponding to the position in the reactor during deposition. Excepting the first few centimeters, both the Zr content and thickness are linearly graded.

The sheet resistance for this same set of films is shown in Figure 4.17. If the electrical properties (carrier concentration and mobility) were the same for all samples, one should expect a linear *increase* in sheet resistance due to the linear *decrease* in film thickness. We observe that for Zr concentrations higher than about 5 at.%, the sheet resistance, *R_S*, increases sharply. Films with a few at.% Zr have similar sheet resistance. To separate the effects of film thickness and Zr concentration on *R_S*, the carrier concentration and Hall mobility data are shown in Figure 4.18. Particularly evident, is that even for up to ~10% Zr in SnO_2:F films, carrier mobility is still above 20 $cm^2/V \cdot s$ while charge carrier concentrations vary in the range of 0.5-2.5 x 10^{20} cm^{-3}. A more in depth analysis of the variation in carrier mobility as it relates to zirconia addition is presented in Chapter VI. Films containing in the range of ~1-5 at.% Zr have similar carrier concentration values to FTO processed under similar conditions, and this is observed for many sets of samples.

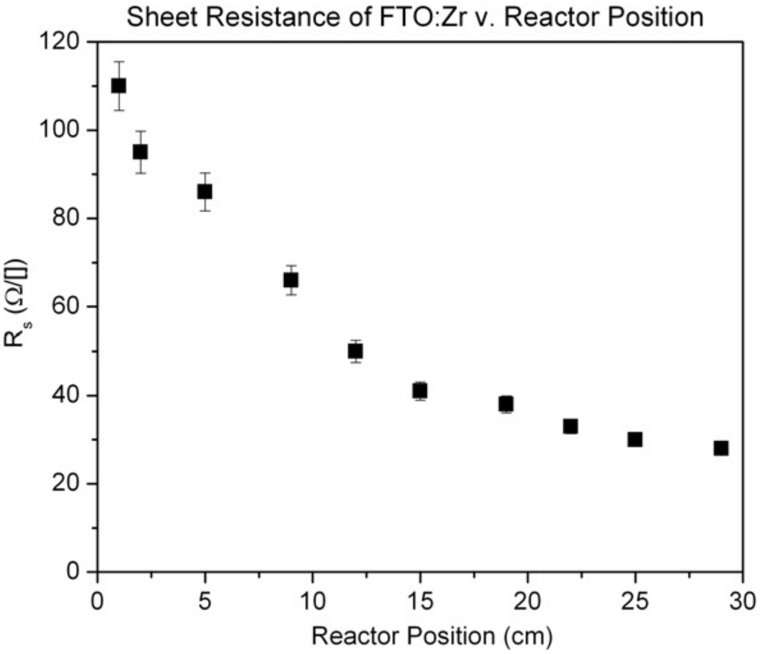

Figure 4.17. Sheet resistance of FTO films containing in the range of ~1-10 at.% Zr. Comparison with Figure 4.16 indicates that films with a ~1-5 at.% Zr have similar sheet resistance values, while the films with 5-10 at.% Zr show a steep increase in resistance values.

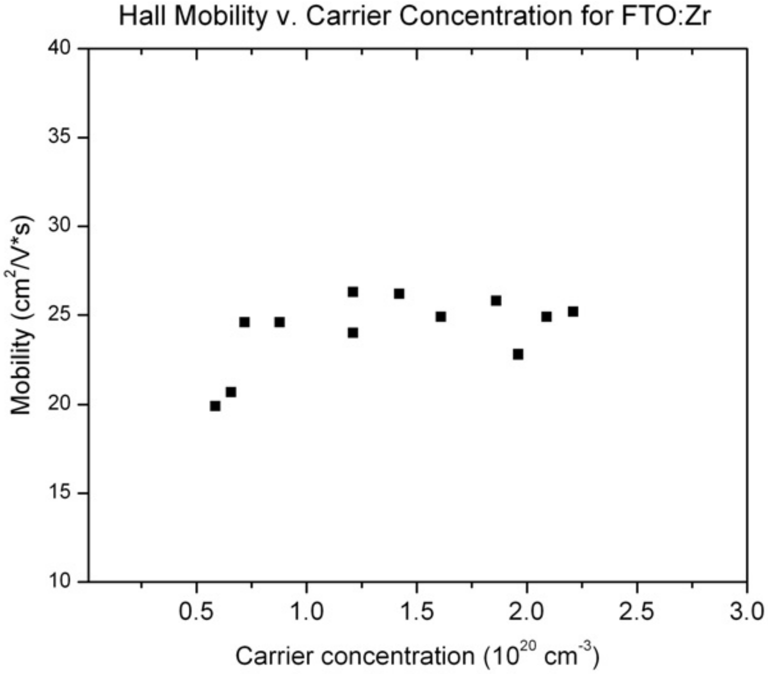

Figure 4.18. The mobility and carrier concentration as obtained from Hall measurements. Films with ~ 1-5 at.% Zr maintain both high carrier concentration and mobility values close to 25 cm^2/V·s. Interestingly, the mobility remains relatively high even for ~ 10 at.% Zr in the FTO films.

The optical performance of a TCO film is particularly important when evaluating their efficacy for PV devices. The transmittance data for an FTO film and for FTO containing ~ 1-5 at.% Zr is presented in Figure 4.19. Though the carrier concentration, mobility and film thickness do not vary greatly, the transmittance window is widened for the films containing ZrO_2. This promising result of increased transmittance in the NIR is studied more in depth in Chapter V. The optical bandgap increases to 3.95 eV (from 3.87 eV for SnO_2:F) for a sample with ~3 at.% Zr addition; however, the carrier concentration is nearly identical ($n \sim 2 \cdot 10^{20}$ cm^{-3}). Since the bandgap widening is not explained through conduction band filling, we conclude that this is a result of alloying with the wide bandgap ZrO_2.

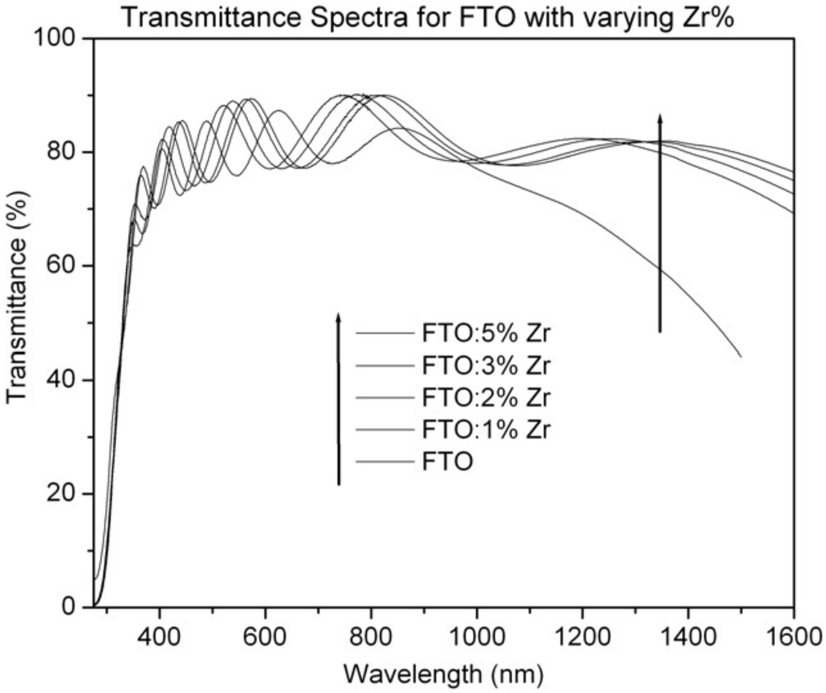

Figure 4.19. Transmittance data for FTO films with various Zr concentrations. An increase in the NIR transmittance is observed with increasing zirconia.

The addition of zirconia into fluorine-doped tin oxide impacts the crystal structure and decreases texture. The X-ray diffraction scans for films of FTO and FTO with 1, 3 and 5 at.% Zr are shown in Figure 4.20. Only peaks associated with tin oxide are evident, and none of the peaks can be indexed to any of the ZrO_2 polymorphs. The intensity ratio, I_{002}/I_{110}, decreases sharply from ~ 10 to 1.7 for FTO and FTO:5%Zr, respectively. We discussed in a previous section the impact of F-doping on tin oxide, in particular the prominence of the [002] texture. Figure 4.21 offers the XRD spectra for films prepared with different F precursor flow rates (referred by their relative amount to the O_2 flow rate). They were deposited under otherwise identical conditions, and the cation composition for the films is approximately 1 at.% Zr. XPS results indicate that the F content in the film increases with $CBrF_3$ flow rate, with an estimated maximum of 3 at.% F. As the F/O_2 flow ratio decreases, the (002) peak intensity remains relatively constant. However, the intensity corresponding to (110)-orientated grains increases with decreasing F. Similarly, several more peaks become apparent, all of which can be indexed to tetragonal SnO_2. Interestingly, however, we observe additional peaks corresponding to grain orientations not observed in our tin oxide or FTO films. Our observations in the previous section argued for a correlation between changes in crystal structure, mobility and scattering due to fluorine incorporation. For films containing Zr, we note that the mobility remains relatively high and constant with Zr addition, yet the structure and texture may change dramatically. Therefore, a fundamental difference in the dominant scattering mechanisms which limit mobility must be due to the addition of zirconia. Chapter VI offers further discussion of this analysis.

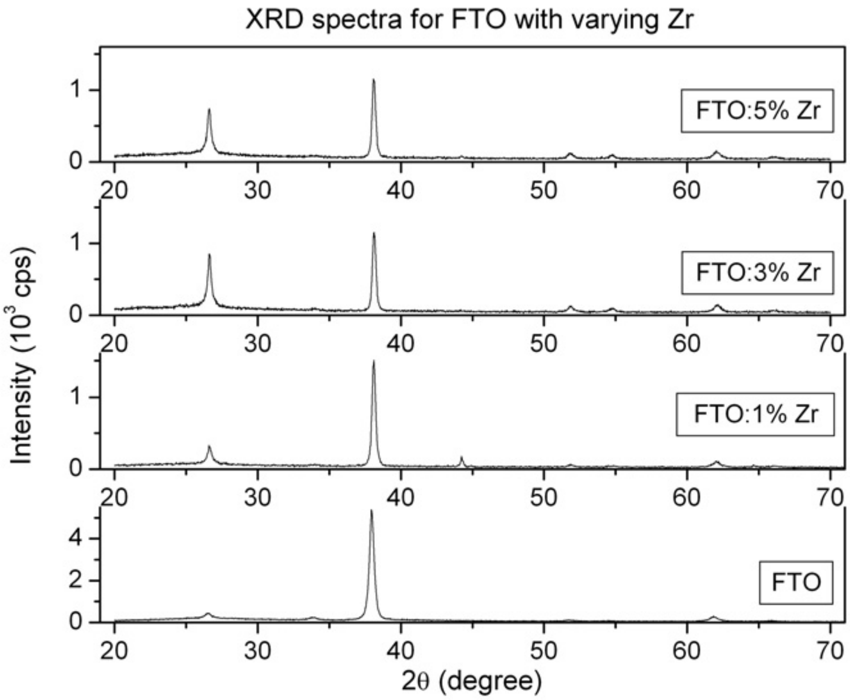

Figure 4.20. XRD spectra of FTO films with 0, 1, 3 and 5 at.% Zr.

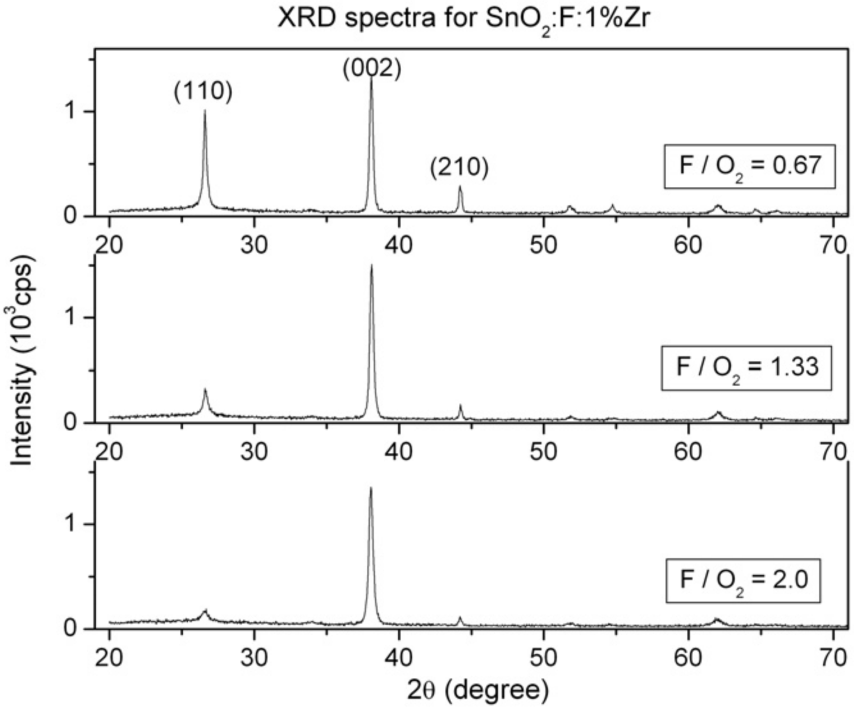

Figure 4.21. X-ray spectra for films of FTO:1%Zr for varying $CBrF_3/O_2$ flow ratios.

The surface morphology, studied by AFM, is also impacted by the ZrO_2 content in the FTO films. Figure 4.22 shows 3-D images of the surfaces of FTO samples with a) 1 at% Zr ($F/O_2 = 2.0$), b) 1 at% Zr ($F/O_2 = 0.67$), and c) 3 at% Zr ($F/O_2 = 0.67$). Comparing a) and b), the FTO:1%Zr samples, the film deposited with higher F precursor flow rate has slightly lower surface roughness than for the lower F flow rate, 7 nm and 9 nm respectively. Again, a lower surface roughness correlated with higher [002] prominence is consistent with the fact that (002) grains will have smoother surface features than (110)- or (211)- oriented grains, which tend to be more pyramidal than flat. Comparing b) and c), it is observed that surface roughness increases with increasing ZrO_2 content, which is again consistent with the observations from the XRD analysis. A more extensive analysis of the surface roughness is performed for sets of films formed by similar process conditions but varying zirconia content. The results for the average surface roughness estimated from AFM measurements and from the SE model are plotted together in Figure 4.23. Using either technique, we observe an increase in surface roughness with increasing ZrO_2 content, especially for greater than ~ 1 at.% Zr. The data extracted from SE modeling consistently gives roughness values nearly twice that obtained from the AFM technique. This inconsistency is actually expected due to the difference in which average surface roughness is defined in the two methods. Further discussion on this topic and the two techniques is provided in Chapter III.

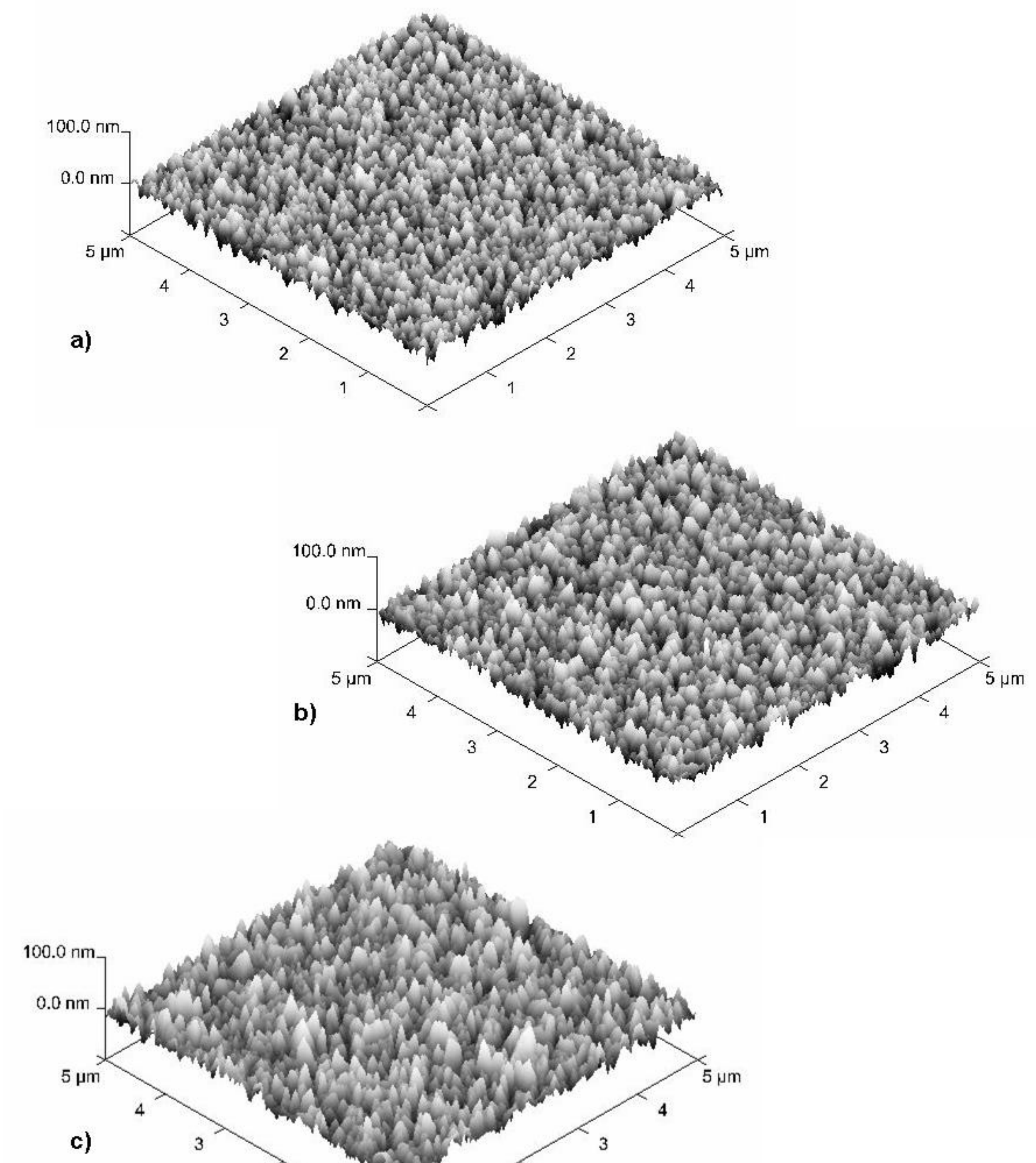

Figure 4.22. AFM surface topography images of the surfaces of FTO samples with a) 1 at% Zr ($F/O_2 = 2.0$); b) 1 at% Zr ($F/O_2 = 0.67$); and c) 3 at% Zr ($F/O_2 = 0.67$).

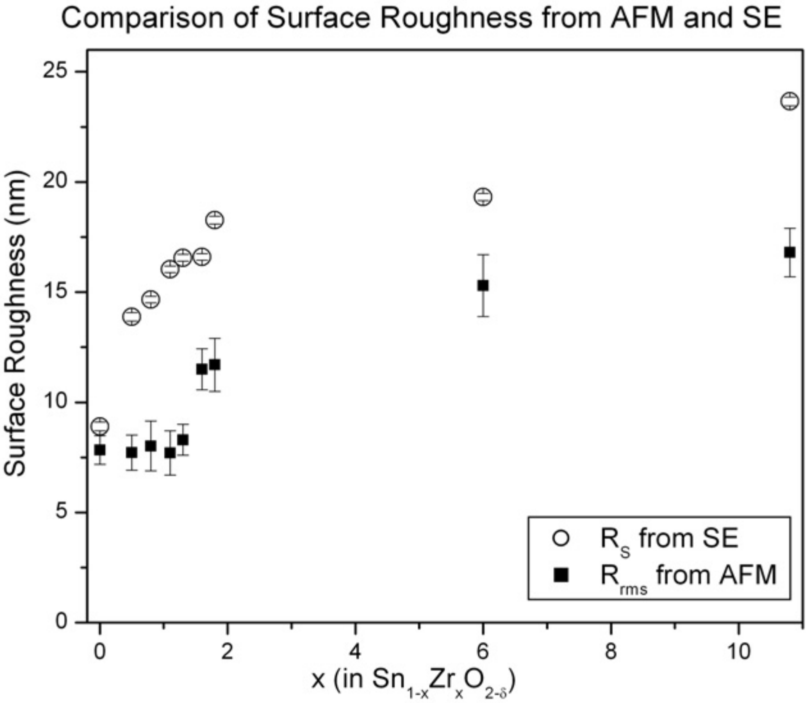

Figure 4.23. Average surface roughness values obtained from AFM and SE analysis for FTO films with varying ZrO_2 content.

Results for Damp Heat Stability Testing

In addition to high visible transparency and electrical conductivity, these properties of a TCO film must not degrade over time [33]. An accepted method for accelerated lifetime testing (ALT) of TCOs is the so-called 85/85 test [34, 35]. The test consists of 1000 cumulated hours of exposure to damp heat: 85˚C at 85% relative humidity (R.H.), which is said to simulate 25 years of exposure in the environment typical for PV. A set of control samples, which were a matched pair to those used in the damp heat study, were left at ambient (in a sample drawer at room conditions) and measured at the beginning and end of the ALT. The control samples showed no variation in sheet resistance or measured Hall properties (as expected). The sample set consisted of: FTO:1%Zr, FTO:5%Zr, and a FTO:1%Zr deposited under high F/O_2 conditions, all with starting sheet resistance values in the range 10-15 Ω/□. This set of samples was repeated for depositions which yielded thinner films corresponding to starting sheet resistance values in the range of about 100 Ω/□. A "standard" FTO sample (labeled L080606 in the figure) and a commercially-available FTO sample (Pilkington Tec15™) are included in the study. This study tests the damp heat stability (and the projected 25 year lifetime PV exposure) of FTO: with varying ZrO_2 content, varying F content and varying thickness.

Figure 4.24 shows little difference in sheet resistance (4pp) variation throughout the duration of the test. For the thicker films ($t \sim 500$ nm, corresponding to $R_S \sim 10\text{-}15$ Ω/□), essentially no change is observed. Hall measurements confirm the results obtained by 4pp. Error bars are not included because of the overlap between data points. However, the sheet resistance measurement may be considered to have an error of approximately ± 1 Ω/□. Therefore, apparent changes in the sheet resistance with damp heat exposure may not be statistically relevant. However, further analysis of the thinner (50-100 nm) films suggests that changes to the electronic properties occur during the ALT. Indeed, for the sample formed under high F/O_2, the charge carrier concentration *decreased* from $n \sim 1.7 \cdot 10^{20} \mathrm{cm}^{-3}$ to $1.2 \cdot 10^{20} \mathrm{cm}^{-3}$, yet the carrier mobility remained constant ($\mu \sim 23\ \mathrm{cm}^2/\mathrm{V \cdot s}$). The resistivity values obtained from the Hall measurements were comparable to the 4-point probe sheet resistance values. No other analysis is used to study these films at this time, though we could speculate that thinner films were more susceptible to water vapor adsorption, which would account for a decreased electron density.

We note that the thicker films, which correspond to sheet resistance values in the range of 10-15 Ω/□ are more consistent with what would be useful in a PV device. However, the increased sheet resistance (due to decreased carrier concentration) with damp heat exposure may provide an avenue for interesting future research. Further, the oxide buffer layer is typically of this order of thickness, but with resistance values about 3 orders of magnitude higher. Therefore, it is not clear from this study how damp heat would affect the oxide buffer layer in ALT by damp heat exposure.

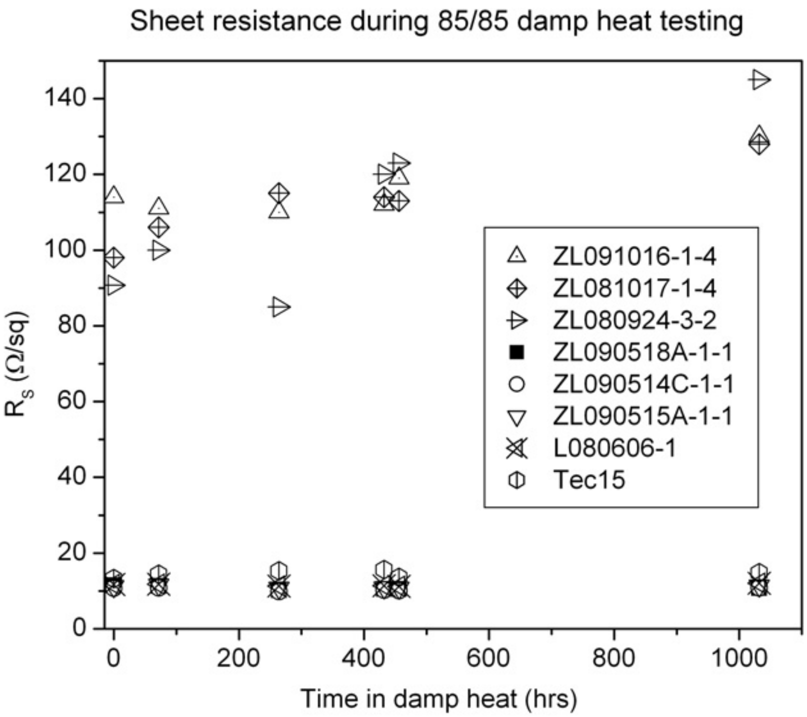

Figure 4.24. Results for the change in sheet resistance during damp heat exposure for accelerated lifetime testing of FTO, FTO:1%Zr, FTO:5%Zr and FTO:1%Zr at high F/O_2 pressures. The sets of films include those deposited to two different thicknesses (corresponding to the sheet resistance changes). A commercial FTO sample is included (Pilkington Tec15™).

References

1. Wu, X.Z., *High-Efficiency Polycrystalline CdTe Thin-Film Solar Cells.* Solar Energy, 2004. **77**(6): p. 803-814.

2. Li, X.A., T.A. Gessert, and T. Coutts, *The Properties of Cadmium Tin Oxide Thin-Film Compounds Prepared by Linear Combinatorial Synthesis.* Applied Surface Science, 2004. **223**(1-3): p. 138-143.

3. Song, Z., B.R. Rogers, and N.D. Theodore, *Spectroscopic Ellipsometry Characterization of ZrO_2 Films on Si(100) Deposited by High-Vacuum-Metalorganic Chemical Vapor Deposition.* Journal of Vacuum Science & Technology A, 2004. **22**(3): p. 711-718.

4. Dorsch, O., M. Werner, E. Obermeier, R.E. Harper, C. Johnston, and I.M. Buckley-Golder, *Etching of Polycrystalline Diamond and Amorphous Carbon Films by RIE.* Diamond and Related Materials, 1992. **1**(2-4): p. 277-280.

5. Kukli, K., M. Ritala, T. Sajavaara, J. Keinonen, and M. Leskelä, Thin Solid Films, 2002. **416**: p. 72.

6. Aarik, J., J. Sundqvist, A. Aidla, J. Lu, T. Sajavaara, K. Kukli, and A. Hårsta, Thin Solid Films, 2002. **418**: p. 69.

7. Kukli, K., M. Ritala, J. Sundqvist, J. Aarik, J. Lu, T. Sajavaara, M. Leskelä, and A. Hårsta, Journal of Applied Physics, 2002. **92**: p. 5698.

8. Atik, M., J. Zarzycki, and C. Rkha, *Protection of Ferritic Stainless-Steel against Oxidation by Zirconia Coatings.* Journal of Materials Science Letters, 1994. **13**(4): p. 266-269.

9. Izumi, K., H. Tanaka, M. Murakami, T. Deguchi, A. Morita, N. Tohge, and T. Minami, *Coating of Fluorine-Doped ZrO_2 Films on Steel Sheets by Sol-Gel Method.* Journal of Non-Crystalline Solids, 1990. **121**(1-3): p. 344-347.

10. Chow, T.P., M. Ghezzo, and B.J. Baliga, *Antimony-Doped Tin Oxide-Films Deposited by the Oxidation of Tetramethyltin and Trimethylantimony.* Journal of the Electrochemical Society, 1982. **129**(5): p. 1040-1045.

11. Borman, C.G. and R.G. Gordon, *Reactive Pathways in the Chemical Vapor-Deposition of Tin Oxide-Films by Tetramethyltin Oxidation.* Journal of the Electrochemical Society, 1989. **136**(12): p. 3820-3828.

12. Ghoshtagore, R.N. in *Proc. Int. Conf. Chem. Vap. Dep.* 1977.

13. Ghoshtagore, R.N., *Mechanism of CVD Thin-Film SnO_2 Formation.* Journal of the Electrochemical Society, 1978. **125**(1): p. 110-117.

14. Vetrone, J. and Y.W. Chung, *Organometallic Chemical Vapor-Deposition of SnO_2 Single-Crystal and Polycrystalline Films.* Journal of Vacuum Science & Technology a-Vacuum Surfaces and Films, 1991. **9**(6): p. 3041-3047.

15. van Mol, A.M.B., *PhD Thesis*. 2003, TU Eindhoven.

16. Kilic, C. and A. Zunger, *N-Type Doping of Oxides by Hydrogen.* Applied Physics Letters, 2002. **81**(1): p. 73-75.

17. Kilic, C. and A. Zunger, *Origins of Coexistence of Conductivity and Transparency in SnO_2.* Physical Review Letters, 2002. **88**(9): p. -.

18. Batzill, M. and U. Diebold, *The Surface and Materials Science of Tin Oxide.* Progress in Surface Science, 2005. **79**(2-4): p. 47-154.

19. Li, X., J. Penkow, B. To, and T. Gessert, *Comparison between Research-Grade and Commercially Available SnO_2 for Thin-Film CdTe Solar Cells*, in *33rd IEEE Photovoltaics Specialists Conference,*. 2008: San Diego, CA.

20. Robertson, J., *Disorder, Band Offsets and Dopability of Transparent Conducting Oxides.* Thin Solid Films, 2008. **516**(7): p. 1419-1425.

21. Rose, D.H., F.S. Hasoon, R.G. Dhere, D.S. Albin, R.M. Ribelin, X.S. Li, Y. Mahathongdy, T.A. Gessert, and P. Sheldon, *Fabrication Procedures and Process Sensitivities for CdS/CdTe Solar Cells.* Progress in Photovoltaics, 1999. **7**(5): p. 331-340.

22. Li, X., J. Pankow, and Y. Yan. *Impurity Study of Optical Properties in Fluorine-Doped Tin Oxide for Thin-Film Solar Cells*. in *Materials Research Society Symposium*. 2009.

23. Hartnagel, H.L., A.L. Dawar, A.K. Jain, and C. Jagadish, *Semiconducting Transparent Thin Films*. 1995, Philadelphia: IOP Publishing Ltd.

24. Schroeder, D.K., *Semiconductor Material and Device Characterization*. 1990: Wiley.

25. Gurumurugan, K., D. Mangalaraj, and S.K. Narayandass, *Structural Characterization of Cadmium-Oxide Thin-Films Deposited by Spray-Pyrolysis.* Journal of Crystal Growth, 1995. **147**(3-4): p. 355-360.

26. Cullity, B.D., *Elements of X-Ray Diffraction*. 1978: Addison Wesley.

27. Guineir, A., *X-Ray Diffraction in Crystals, Imperfect Crystals, and Amorphous Bodies*. 1994, New York: Dover Publications.

28. Batzill, M., J.M. Burst, and U. Diebold, *Pure and Cobalt-Doped* SnO_2*(101) Films Grown by Molecular Beam Epitaxy on* Al_2O_3. Thin Solid Films, 2005. **484**(1-2): p. 132-139.

29. Batzill, M. and U. Diebold, *Surface Studies of Gas Sensing Metal Oxides.* Physical Chemistry Chemical Physics, 2007. **9**(19): p. 2307-2318.

30. Zheng, J.G., X. Pan, M. Schweizer, U. Weimar, W. Göpel, and M. Rühle, *Crystallographic Shear Planes in Nanocrystalline* SnO_2 *Thin Films by High-Resolution Transmission Electron Microscopy.* Journal of Materials Science, 1996. **31**(9): p. 2317-2324.

31. Moss, T., *The Interpretation of the Properties of Indium Antimonide*, Proc. Phys. Soc., 1954. **67B**: p. 775.

32. Burstein, E., *Anomalous Optical Absorption Limit in InSb*, Phys. Rev., 1954. **93**: p. 632.

33. Osterwald, C.R., T.J. McMahon, and J.A.d. Cueto, *Electrochemical Corrosion of* SnO_2*:F Transparent Conducting Layers in Thin-Film Photovoltaic Modules.* Solar Energy Materials and Solar Cells, 2003. **79**(1).

34. Pern, F.J., R. Noufi, X. Li, C. DeHart, and B. To. *Damp-Heat Induced Degradation of Transparent Conducting Oxides for Thin-Film Solar Cells*. in *33rd IEEE Photovoltaics Specialists Conference*. 2008. San Diego, CA.

35. IEC, *Damp Heat Stability, 61646.*

CHAPTER V

ENHANCED OPTICAL TRANSMITTANCE OF HIGHLY CONDUCTIVE F-DOPED SnO_2 THROUGH PERMITTIVITY ENGINEERING

We report enhanced transmission from degenerate fluorine-doped SnO_2 films alloyed with ZrO_2. Spectroscopic ellipsometry measurements show these films exhibit increased permittivity in agreement with Drude theory. Fluorine-doped SnO_2 films with less than ~5 at.% Zr maintain high electrical conductivity, with corresponding Hall mobility up to 32 $cm^2/V\cdot s$. The potential impact of integrating these films into photovoltaic devices is discussed by calculating short circuit current density losses due to absorption in the transparent conducting electrode. Our analysis shows that addition of ~ 1.5% ZrO_2 into F-doped SnO_2 films decreases the loss in current density by 0.6 mA/cm^2.

Introduction

Metal oxides that combine electrical conductivity and optical transparency are important materials for production of photovoltaic (PV) solar cells, window coatings, flat panel displays and other products [1, 2]. These transparent conducting oxides (TCOs) are typically n-type and include alloys of cadmium oxide, indium oxide, tin oxide and zinc oxide, which are degenerately-doped to bring their conductivity to acceptable levels. However, high charge carrier concentration is typically needed to achieve high conductivity. However, high charge carrier concentration reduces optical transmission at longer wavelengths due to absorption by free carriers [3]. The cost of the reduced transmission through F-doped SnO_2 electrodes has been estimated at 5% of the PV cell's current density [4]. This tradeoff between optical and electrical performance has driven research in the field toward materials which yield a compromise between optical transmittance and electrical resistivity for a given application [5-9].

Glass coated with SnO_2, the most common TCO in terms of production volume and application diversity, is currently used in the production of low-emissivity glass and thin film Si- and CdTe-based photovoltaic devices [10]. For TCO applications, tin oxide is typically doped with fluorine (referred to as FTO) in the range of a few atomic percent. The main advantages to using tin oxide are that it contains neither scarce indium nor toxic cadmium and the optical and electrical properties remain stable in high temperature processing (> 650 ºC). Other benefits include long-term environmental stability and chemical resistance [11]. However, electron mobility in tin oxide generally is less than that in indium oxide or cadmium oxide, and therefore a higher charge carrier concentration is necessary to achieve similar conductivity.

Coutts *et al* applied the Drude theory to TCOs [12]. Their analysis suggests that increasing charge carrier mobility (i.e. increasing the relaxation time between scattering events) is the preferred path to minimize absorption due to free carriers. Further analysis of the Drude theory suggests that increasing the permittivity of the host transparent conductor should shift the plasma edge to longer wavelengths [13]. The plasma frequency, ω_P (plasma wavelength, λ_P), in terms of a material's high frequency permittivity, ε_∞, is shown to be

$$\omega_P{}^2 = \frac{ne^2}{\varepsilon_\infty \varepsilon_0 m^*}, \quad \left(\lambda_p = 2\pi \cdot c \sqrt{\frac{\varepsilon_0 \varepsilon_\infty m^*}{ne^2}} \right) \tag{5.1}$$

where c is the speed of light, ε_o is the permittivity of free space, m^* is the electron effective mass, n is the carrier concentration and e is the electronic charge [13, 14]. The real and imaginary parts of the complex permittivity ($\tilde{\varepsilon} = \varepsilon_1 + i\varepsilon_2$) are related to the electrical properties by

$$\varepsilon_1(\omega) = \varepsilon_\infty - \frac{ne^2}{\varepsilon_0 m^* \omega^2} \tag{5.2}$$

$$\varepsilon_2(\omega) = \frac{ne^2}{\varepsilon_0 m^* \omega^3 \tau} \tag{5.3}$$

where τ is the mean scattering time for free electrons [3, 14, 15].

The present work outlines a method for maintaining or improving electrical properties in chemical vapor deposited (CVD) tin oxide-based films while enhancing optical performance. We report improved near-infrared transmission of fluorine-doped tin oxide (FTO) through the addition of 1-5 cat% Zr. Importantly, the Zr-doped FTO films have similar electrical properties to FTO films. Extending the transmission bandwidth of FTO transparent electrodes in thin film photovoltaic (PV) cells will directly lead to increased PV cell efficiency.

Experimental

The films are deposited on Corning 1737 glass by low-pressure chemical vapor deposition (LPCVD), a process currently used in large-area device fabrication. The CVD system has been previously described in Chapter III. Details of the deposition process are discussed in Chapter IV. The films' electrical resistivity, charge carrier concentration and carrier mobility are ascertained by Hall measurements in the van der Pauw configuration (Bio Rad HL5500) [16]. Optical transmittance and reflectance spectrophotometric measurements are used to obtain absorptance, absorption coefficient and optical bandgap (Varian Cary 6i) [3]. The spectrophotometer data are referenced to air, and thus include the substrate contribution. Film thickness is determined by stylus profilometry and spectroscopic ellipsometry (Dektak 8 and J.A. Woollam M-2000, respectively). Film composition is determined from X-ray photoelectron spectroscopy (XPS) measurements (PHI 5000 Versa-Probe). Zr concentration is given in cation %, employing published sensitivity factors [17]. Structural properties are obtained from X-ray diffraction (XRD, Scintag DMS).

Results

The pure tin oxide sample has resistivity, $\rho \sim 1\ \Omega\cdot\text{cm}$, associated with both low mobility and carrier concentration. The XRD spectrum (not shown) indicates that this is randomly oriented polycrystalline material. F-doping induces a strong (002) texture, and a decrease in the resistivity to approximately $10^{-4}\ \Omega\cdot\text{cm}$. Only diffraction peaks associated with tin oxide are identified in XRD spectra of films alloyed with up to ~ 10% ZrO_2. This indicates that the films retain the rutile tetragonal structure of the tin oxide host lattice. Optical and electrical analyses indicate that the doped films are degenerate transparent conductors. Figure 5.1 shows the extracted Hall mobility and charge carrier concentration for several samples with varying Zr concentrations in SnO_2:F. Data for an undoped SnO_2 sample and several SnO_2:F samples are included for comparison. The general trend is that carrier mobility remains above ~ 25 $cm^2/V\cdot s$ for up to ~6 cat.% Zr, while mobility and carrier concentration both decrease for Zr concentrations $\geq 8\%$. Importantly, the electrical properties of films containing 1-5 at.% Zr are nearly identical to that of the SnO_2:F with no Zr addition. The highest mobility, $\mu = 32$ $cm^2/V \cdot s$, is observed for the films containing 2 at% Zr.

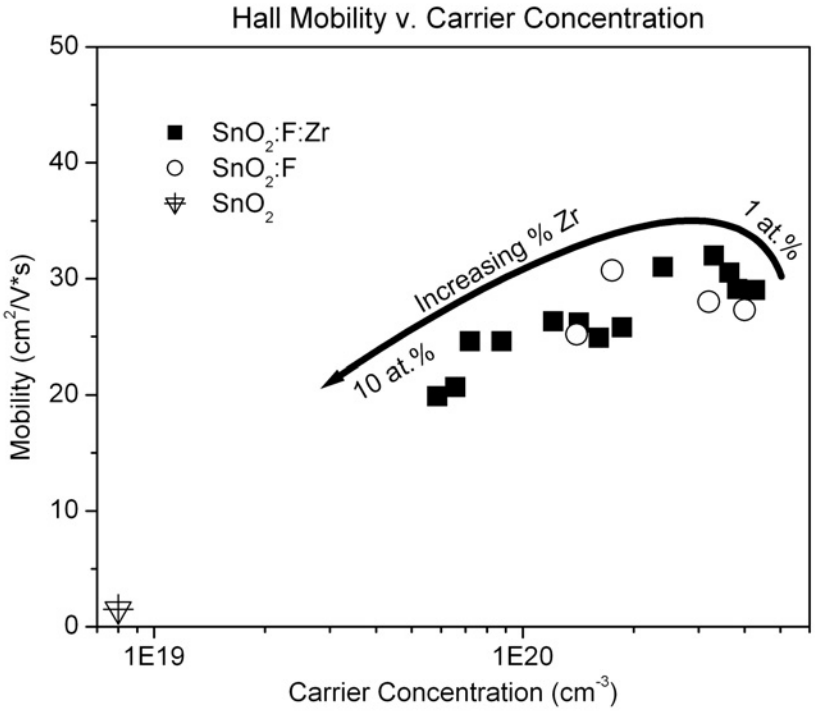

Figure 5.1. Extracted Hall mobilities and charge carrier concentrations for samples with 0-10 at% Zr in SnO_2:F, and an undoped SnO_2 sample. Carrier mobility remains above 25 for up to ~6 at.% Zr .Mobility and carrier concentration both decrease for > 8 at % Zr. The electrical properties of films containing 1-3 at.% Zr are nearly identical to that of SnO_2:F.

The optical properties of films with similar electrical properties and physical thickness but with different Zr content were analyzed by spectroscopic ellipsometry. Figure 5.2 shows the real part of the permittivity, ε_1, for SnO_2:F with ~1-10% Zr. The data for FTO and ZrO_2 are included for comparison. A large increase in permittivity is observed for 1% Zr addition. As Zr concentration increases to > 10%, the observed permittivity approaches that of ZrO_2. Large increases in permittivity at low alloying concentrations have been observed by others [13, 18]. Lucovsky *et al* have explained the increase in permittivity of silicates with small ZrO_2 additions in terms of a microscopic model to simulate the experimental data [18]. Their results are shown together with our current results for ZrO_2 in SnO_2:F in Figure 5.3. Recalling from Drude theory that the plasma wavelength, λ_p, is centered at $\varepsilon_1 = 0$, a shift of λ_p deeper into the IR is observed in Figure 5.2 for ZrO_2-containing samples compared to the standard SnO_2:F. This trend is precisely what is predicted by equations (5.1) and (5.2).

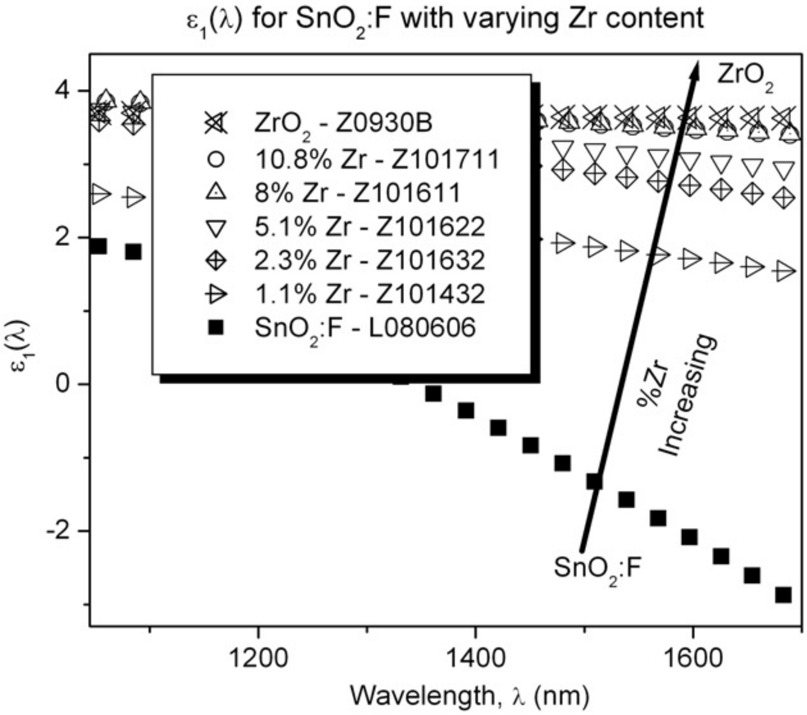

Figure 5.2. Real part of permittivity obtained by Drude-Lorentz parameterization of spectroscopic ellipsometry data for ~1-10% Zr in F-doped SnO_2. Undoped SnO_2:F (bottom) and ZrO_2 (top) are included for comparison.

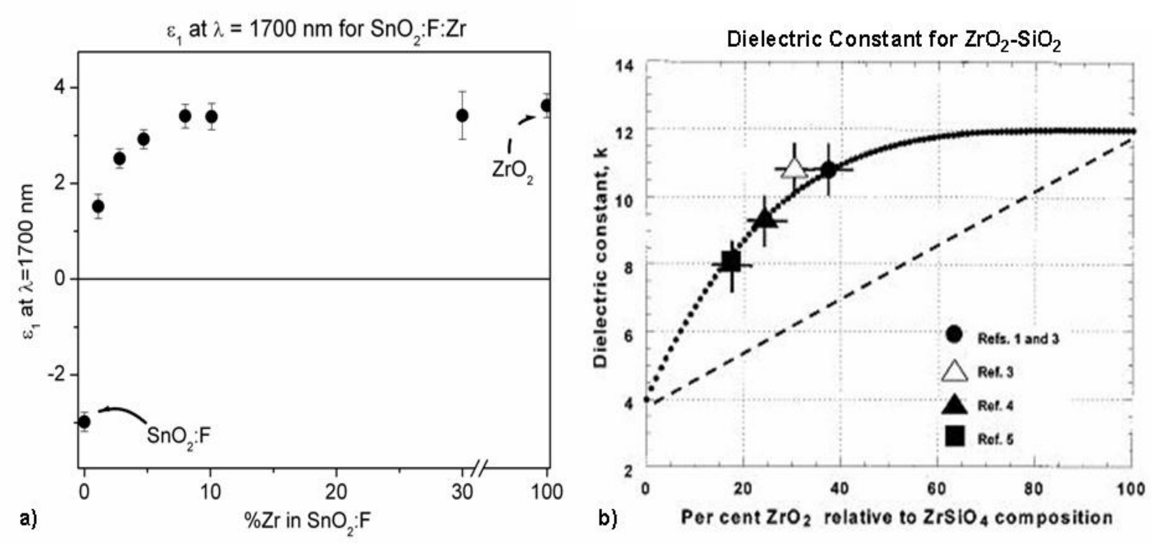

Figure 5.3. a) The increase in ε_1 at 1700 nm with ZrO_2 content in SnO_2:F (from Figure 5.2) compared to the increase in κ with ZrO_2 in SiO_2, from *Lucovsky et al* [18].

The measured transmittance and calculated absorptance of SnO_2:F and that with ~1% Zr is shown in Figure 5.4. This set of films has fairly low carrier concentration, which may desirable for some applications. Further, as will be discussed, they serve as a useful comparison to films with a higher charge carrier density. Though the electrical data, *n* and μ, are similar for the films, increased transmittance through most of the visible wavelength spectrum is observed for the film alloyed with ZrO_2. A dramatic increase in transmittance is apparent at longer wavelengths, consistent with the decreased absorptance in the NIR. This increased optical performance is consistent with the shift in the plasma wavelength deeper into the IR, and is attributed to the increased permittivity of the film upon addition of Zr.

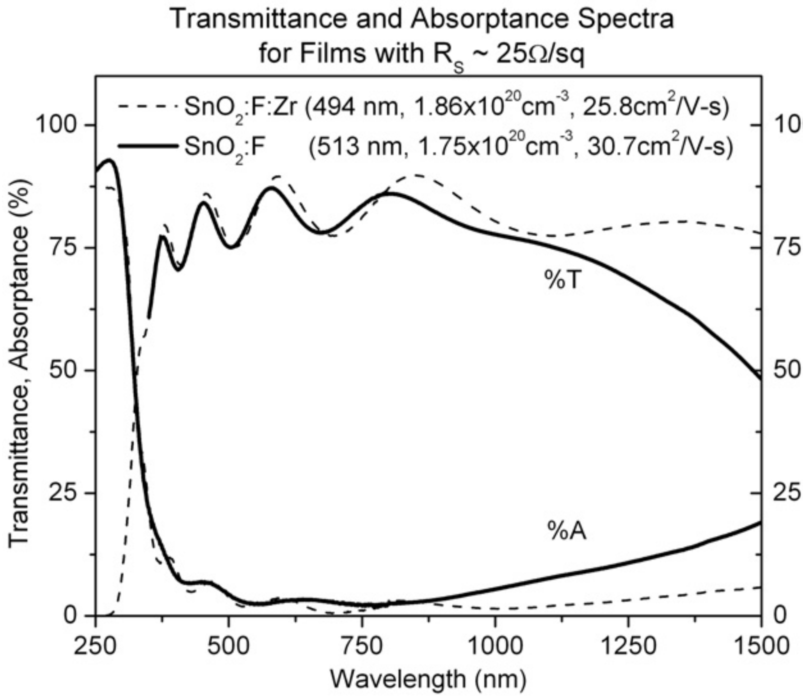

Figure 5.4. Transmittance and absorptance of SnO_2:F films with 0 and 1.1% Zr doping. Having similar charge carrier concentration and electron mobility, films with ~1% Zr display increased optical performance compared to films with 0% Zr.

Figure 5.5 shows the measured transmittance and calculated absorptance of FTO and that with ~2 at% Zr. These films exhibit higher values of carrier concentration than those presented in Figure 5.4, which yield a nominal sheet resistance of 10 Ω/□. These electrical properties are consistent with that typically utilized for CdTe-based absorbers in PV applications [19]. Again, for the sample alloyed with ZrO_2, we observe increased transmittance through most of the visible region with a slight optical bandgap widening from 3.86 eV to 3.92 eV. Because the charge carrier concentration is similar for the two films, the optical bandgap widening (blue-shift) cannot be explained by the conventional conduction band-filling mechanism as presented by Burstein and Moss [20, 21]. Instead, we attribute this to the alloying effect with the wide bandgap (5.8 eV) zirconium oxide.

A fairly uniform increase in transmittance is observed at near-infrared wavelengths, again due to the shift in the plasma edge. The fact that the higher conductivity samples have a less dramatic change in NIR response is consistent with the Drude theory expectations: as carrier concentrations increase, the benefit derived by increased permittivity is reduced [13]. Gessert *et al* concisely illustrated these points by differentiating (5.1) with respect to ε_∞ and by n which gives

$$\frac{\partial \lambda_P}{\partial \varepsilon_\infty} = \frac{c}{4\pi}\sqrt{\frac{\varepsilon_0 m^*}{\varepsilon_\infty n e^2}} = \frac{\lambda_P}{2\varepsilon_\infty} \tag{5.4}$$

$$\frac{\partial}{\partial n}\left(\frac{\partial \lambda_P}{\partial \varepsilon_\infty}\right) = -\frac{c}{8\pi}\sqrt{\frac{\varepsilon_0 m^*}{\varepsilon_\infty n^3 e^2}} = -\frac{\lambda_P}{4\varepsilon_\infty n} \tag{5.5}$$

Equation (5.1) indicates that, for a given n, λ_P increases with increasing ε_∞; however, (5.4) further demonstrates that the rate of change in λ_P reduces with increasing ε_∞. This further explains the observation of large increases in transmittance with small increases in permittivity of our films. Equation (5.5) shows that the plasma wavelength decreases with increasing carrier concentration, which is the origin of the well-known tradeoff between increasing conductivity and increasing transparency in TCOs. However, the differential also shows that the rate of change in λ_P for a given ε_∞ is smaller for larger values of n. This is consistent with the differences in improved transmittance for the sets of films in Figures 5.4 and 5.5. The films in Figure 5.5 have ~ 2.5 times greater n, so a smaller change in λ_P, and hence transmittance, is expected when compared to those in Figure 5.4.

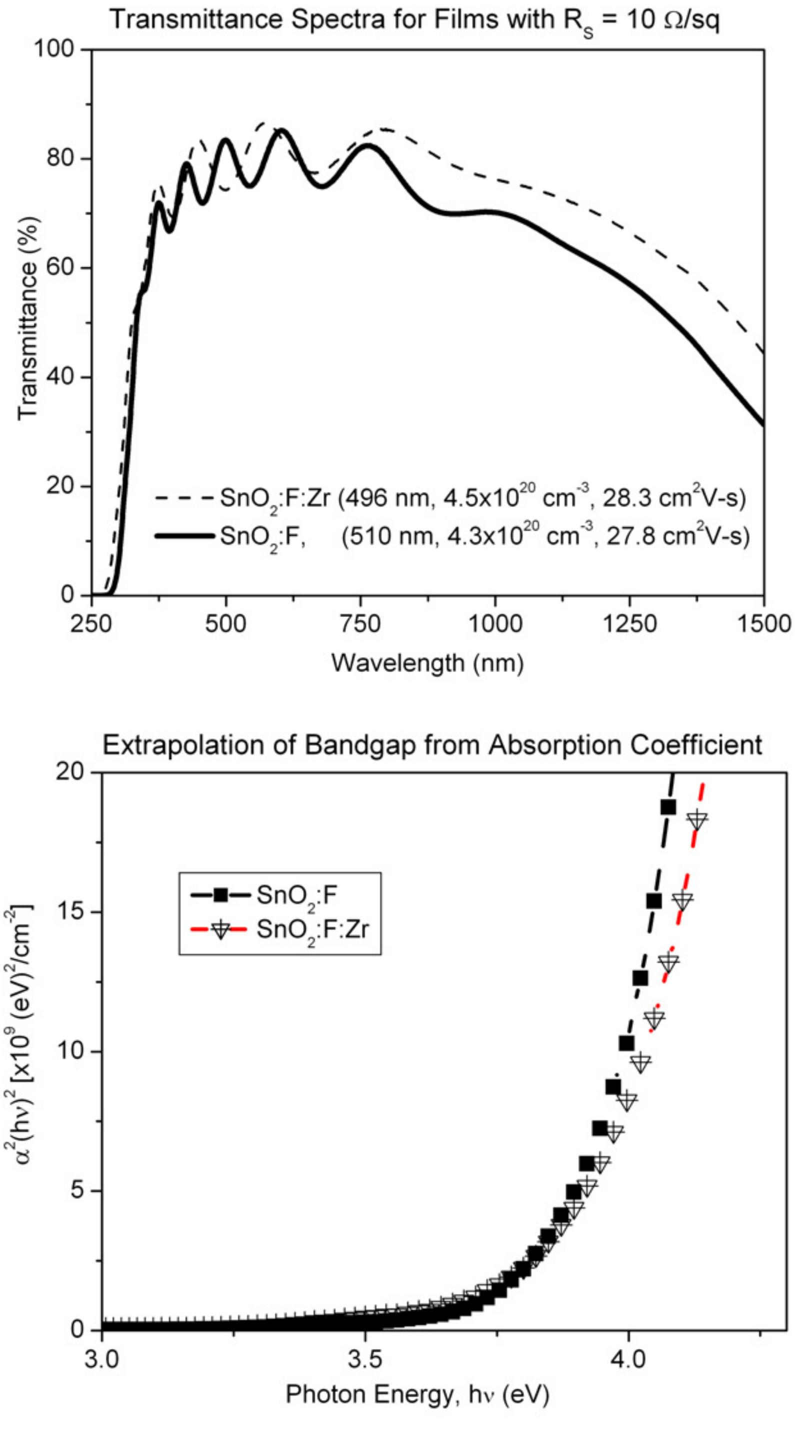

Figure 5.5. (a) Transmittance and absorptance of SnO$_2$:F films with 0 and ~ 2% Zr doping. Having similar electrical properties (R_S ~ 10Ω/□), films with Zr have increased transmittance in the visible and NIR compared to films with 0% Zr. (b) The apparent bandgap for 0% and 2% Zr in SnO$_2$:F. The slight blue shift in the band edge is likely due to alloying with the high bandgap (5.8 eV) zirconia.

Table 5.1 compares the average transmittance (throughout the visible and vis-NIR) for the film set discussed in Figure 5.5. Additionally, we calculate the theoretical short-circuit current density loss due to absorption in the TCO/glass by integrating the average transmittance with the AM1.5 solar spectrum (see Figure 5.6). This is done over two wavelength ranges corresponding to two thin film absorber PV technologies, CdTe and microcrystalline Si (μ-Si). The quantum efficiency for the respective devices is not incorporated in the calculation. We include the data for the glass substrate to aid in weighing the contribution of the starting material. Previous studies by Li *et al* revealed that some glass substrates have a large contribution in optical losses [4]. The visible transmission is slightly greater for the sample with Zr, but an ~ 10% increase in average transmission is calculated when the NIR response is included. The current density loss is 0.6 mA/cm^2 less for the film containing 1.5% ZrO_2 over the wavelength range pertaining to CdTe devices. For μ-Si, the difference in losses due to TCO absorption is less dramatic, despite the apparent enhanced transmission at longer wavelengths. This is due to the fact that much less solar radiance is incident at these longer wavelengths. Finally we calculate a figure of merit (FOM) which considers the integrated (visible) transmittance and sheet resistance, $\Phi = T^{10} / R_S$, as explained by Haacke [22]. This method gives more weight to the optical transmission than other methods, which is perhaps more relevant for comparing films intended for PV applications. An enhancement in the FOM is realized for the film with Zr compared to that without, which is expected from our observations that there is an increase in visible transmittance.

Table 5.1. Comparison of i) optical transmittance in the visible (380-700 nm), ii) visible-to-infrared (380-1200 nm), iii) short-circuit current density loss due to absorption in glass/TCO integrated with the AM1.5 solar spectrum for two wavelength regions corresponding to CdTe (350–860 nm) and μ-Si (350-1200 nm) PV technologies; for films with and without Zr. The sheet resistances are given, and Haacke's figure of merit is calculated [22]. Data for the glass substrate are also compared.

	% Transmission		**J_{SC} loss (mA/cm^2)**		**R_S**	**FOM**
Sample	**vis**	**vis-NIR**	**CdTe**	**μ-Si**	**(Ω/□)**	**(10^{-3}/ Ω)**
SnO_2:F	79%	69%	2.67	4.53	10.2	9.3
SnO_2:F:Zr	81%	79%	2.07	4.3	9.9	12
Corning 1737	91%	91%	0.18	0.37	-	-

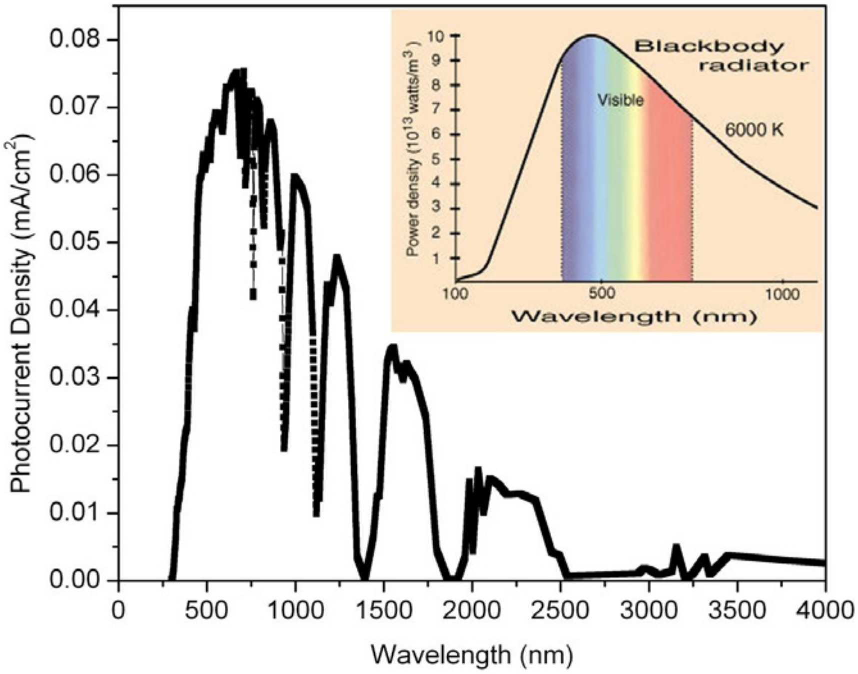

Figure 5.6. The AM1.5 solar irradiance spectrum [23]. The inset shows the calculated power density spectrum for 6000K blackbody radiator.

Tuning the properties of TCOs has historically involved attempts at achieving or maintaining reasonably high mobility while modifying the charge carrier concentration to obtain suitable electro-optical performance. This invariably results in a compromise toward optimization of either the electrical or optical properties. Taken together, Figures 5.2, 5.4 and 5.5a offer compelling evidence that permittivity engineering is an additional path to optimizing TCOs. Further, we demonstrate that permittivity engineering does not negatively impact the electrical properties associated with either of the two other tuning parameters (carrier concentration and carrier mobility).

Conclusions

We have demonstrated that tin oxide-based TCO films with similar electrical properties but higher permittivity can be synthesized via CVD. The higher permittivity leads to an observed higher optical transmittance, particularly in the near infrared. This is attributed to the plasma edge, that is, the frequency at which the free electrons resonate with incident radiation, being shifted to longer wavelengths. Permittivity engineering could be extended to other oxide systems, and perhaps enhanced by alloying with even higher permittivity materials.

References

1. Haacke, G., *Transparent Conducting Coatings.* Annual Review of Materials Science, 1977. **7**: p. 73-93.

2. Chopra, K.L., P.D. Paulson, and V. Dutta, *Thin-Film Solar Cells: An Overview.* Progress in Photovoltaics, 2004. **12**(2-3): p. 69-92.

3. Pankove, J.I., *Optical Processes in Semiconductors*. 1971: Dover Publications, Inc.

4. Li, X., J. Penkow, B. To, and T. Gessert, *Comparison between Research-Grade and Commercially Available SnO_2 for Thin-Film CdTe Solar Cells*, in *33rd IEEE Photovoltaics Specialists Conference,*. 2008: San Diego, CA.

5. Minami, T. and T. Miyata, *Present Status and Future Prospects for Development of Non- or Reduced-Indium Transparent Conducting Oxide Thin Films.* Thin Solid Films, 2008. **517**(4): p. 1474-1477.

6. Campet, G., S.D. Han, S.J. Wen, J.P. Manaud, J. Portier, Y. Xu, and J. Salardenne, *The Electronic Effect of Ti^{4+}, Zr^{4+} and Ge^{4+} Dopings Upon the Physical-Properties of In_2O_3 and Sn-Doped In_2O_3 Ceramics - Application to New Highly-Transparent Conductive Electrodes.* Materials Science and Engineering B-Solid State Materials for Advanced Technology, 1993. **19**(3): p. 285-289.

7. Li, X.A., T.A. Gessert, and T. Coutts, *The Properties of Cadmium Tin Oxide Thin-Film Compounds Prepared by Linear Combinatorial Synthesis.* Applied Surface Science, 2004. **223**(1-3): p. 138-143.

8. Qadri, S.B., H. Kim, H.R. Khan, A. Pique, J.S. Horwitz, D. Chrisey, W.J. Kim, and E.F. Skelton, *Transparent Conducting Films of In_2O_3-ZrO_2, SnO_2-ZrO_2 and ZnO-ZrO_2.* Thin Solid Films, 2000. **377**: p. 750-754.

9. Wu, X.Z., *High-Efficiency Polycrystalline CdTe Thin-Film Solar Cells.* Solar Energy, 2004. **77**(6): p. 803-814.

10. Gerhardinger, P. and D. Strickler, *Fluorine Doped Tin Oxide Coatings - over 50 Years and Going Strong*, in *Innovations in Materials Science*. 2008, Business Wire.

11. Pern, F.J., R. Noufi, X. Li, C. DeHart, and B. To. *Damp-Heat Induced Degradation of Transparent Conducting Oxides for Thin-Film Solar Cells*. in *33rd IEEE Photovoltaics Specialists Conference*. 2008. San Diego, CA.

12. Coutts, T.J., D.L. Young, and T.A. Gessert, *Modeling, Characterization and Properties of Transparent Condicting Oxides*, in *Thin Film Photovoltaics*. to be submitted.

13. Gessert, T.A., Y. Yoshida, C.C. Fesenmaier, and T.J. Coutts, *Sputtered In_2O_3 and ITO Thin Films Containing Zirconium.* Journal of Applied Physics, 2009. **105**(8): p. 6.

14. Wooten, F., *Optical Properties of Solids*. 1972, London: Academic Press, Inc.

15. Ashcroft, N.W. and N.D. Mermin, *Solid State Physics*. 1976: Thomson Learning, Inc.

16. van der Pauw, L.J., *A Method of Measuring Specific Resistivity and Hall Effect of Discs of Arbitrary Shape.* Philips Research Reports, 1958. **13**: p. 1–9.

17. Moulder, J.F., W.F. Stickle, P.E. Sobol, and K.D. Bomben, *PHI Handbook of Photoelectron Spectroscopy*. 1992: Perkin-Elmer Corp.

18. Lucovsky, G. and G.B. Rayner, *Microscopic Model for Enhanced Dielectric Constants in Low Concentration SiO_2-Rich Noncrystalline Zr and Hf Silicate Alloys.* Applied Physics Letters, 2000. **77**(18): p. 2912-2914.

19. Rose, D.H., F.S. Hasoon, R.G. Dhere, D.S. Albin, R.M. Ribelin, X.S. Li, Y. Mahathongdy, T.A. Gessert, and P. Sheldon, *Fabrication Procedures and Process Sensitivities for CdS/CdTe Solar Cells.* Progress in Photovoltaics, 1999. **7**(5): p. 331-340.

20. Burstein, E., *Anomalous Optical Absorption Limit in InSb*, Phys. Rev., 1954. **93**: p. 632.

21. Moss, T., *The Interpretation of the Properties of Indium Antimonide*, Proc. Phys. Soc., 1954. **67B**: p. 775.

22. Haacke, G., *New Figure of Merit for Transparent Conductors.* Journal of Applied Physics, 1976. **47**(9): p. 4086-4089.

23. ASTM, *Terrestrial Reference Spectra for Photovoltaic Performance Evaluation, ASTM G173-03*.

CHAPTER VI

INCREASED MOBILITY IN TIN OXIDE AND FLUORINE-DOPED TIN OXIDE BY ADDITION OF ZrO_2

The carrier mobility is shown to increase when ZrO_2, a high permittivity material, is added to SnO_2 and F-doped SnO_2 thin films. The transparent conducting oxide films are deposited by chemical vapor deposition onto glass substrates in the temperature range of 500-525˚C. The fluorine-to-oxygen content is varied systematically and it is found that the mobility remains higher for films containing up to ~ 10 at% Zr compared to those without zirconia. The results are explained in the context of the increased permittivity and high Lewis acid strength of the zirconia additive.

Introduction

Thin films which are both optically transparent and DC conductive are intensively studied due to their industrial application in, for example, flat panel displays and photovoltaic (PV) solar cells [1-4]. Tin oxide belongs to the class of materials known as transparent conducting oxides (TCOs) and, along with indium oxide, cadmium oxide, zinc oxide and their alloys, are utilized as top contacts in nearly all thin-film PV devices [2]. Their conductivity arises due to intrinsic point defects and is enhanced through extrinsic doping by aliovalent ions.

Although there is a tradeoff between optimizing the optical versus electrical properties in a TCO film, it has been recognized that increasing carrier mobility is the preferred course when optimizing the electro-optical properties [4]. For an n-type material, the DC conductivity is related to the electron concentration, n, and carrier mobility, μ by

$$\sigma = ne\mu \tag{6.1}$$

where e is the electron charge. Therefore conductivity is increased by increasing the carrier concentration , increasing the carrier mobility, or both. The mobility is given by

$$\mu = \frac{e\tau}{m^*} \tag{6.2}$$

where τ is the scattering time and m^* is the effective electron mass. In general, it is recognized that the mobility and carrier concentration cannot be simultaneously increased for high n due to carrier scattering by ionized impurities. This negative correlation between n and τ limits possible increases in μ using conventional methods. The equation for mobility limited by ionized impurity scattering is given by

$$\mu_i = \frac{3h^3(\varepsilon_o\varepsilon_r)^2}{16\pi^2 e^2 m^{*2} n_i f(x)} \tag{6.3}$$

where h is Planck's constant, ε_0 is the permittivity of free space, ε_r is the relative permittivity, $f(x)$ is a function related to the Thomas-Fermi wave vector and n_i is the density of ionized impurities [5]. Note that the magnitude of the mobility is proportional to the square of the relative permittivity. The idea of increasing permittivity as a means to improve the electro-optical properties of TCOs has not been reported in the literature. Indeed, only Gessert *et al* have reported on the effects of permittivity on the *optical* properties of indium oxide-based films [6]. In this chapter, we discuss the effects of increased permittivity on the *electrical* properties of TCO films. The permittivity of the host tin oxide lattice has been shown to increase with the addition of zirconia (discussed in Chapter V), and those results are compared to empirical data and theoretical arguments from other authors to explain the increased mobility in the films of this study.

Experimental Details

Films are deposited on Corning 1737 glass by low-pressure chemical vapor deposition (LPCVD) as described in Chapter III. Details of the deposition process are discussed in Chapter IV. The resistivity, charge carrier concentration and carrier mobility are probed by Hall measurements, using the van der Pauw configuration (Bio Rad HL5500) [7]. Optical transmittance and reflectance measurements are collected on a commercial spectrophotometer (Varian Cary 6i). The spectrophotometer data are referenced to air, and therefore include the contribution from the substrate. Film thickness is determined by stylus profilometry and spectroscopic ellipsometry (Dektak 8 and J.A. Woollam M-2000, respectively), the details of which are given in Chapters 3 and 4. Film composition and valence band structure are determined from X-ray photoelectron spectroscopy (XPS) measurements (PHI 5000 Versa-Probe). Zr concentration is given in cation %, using published sensitivity factors [8]. Film structure is observed by analysis of X-ray diffraction spectra (XRD, Scintag DMS).

Results

Table 6.1 compiles the comparisons of the electrical properties for three sets of SnO_2-based films with and without zirconia: (i) F-doped deposited at a substrate temperature of 500˚C, (ii) F-doped films deposited at 525˚C, and (iii) undoped films, deposited at 525˚C. At 500˚C, the mobility is ~ 50% higher for the samples with zirconia. At 525˚C, we compare films with and without F doping. The critical Mott carrier density defines the minimum carrier density for degeneracy; for tin oxide this value corresponds to $n > 3 \cdot 10^{18}$ cm^{-3} (see Chapter III for details). The F-doped samples are all degenerate, as evidenced by the high carrier concentration, and the sample with 2 at% Zr addition has similar carrier concentration to the FTO sample, but higher mobility. The sample with 10 at% Zr has both slightly lower carrier concentration and mobility. Taken together with the previous sample set, this indicates that the electrical properties are limited to this higher level of zirconia addition. Indeed, it was discussed in Chapters IV and V that an increase in resistivity was observed for films containing more than 6 at% Zr, whereas films with 1-5% Zr maintain carrier concentrations similar to the unaltered host.

The undoped (no F) samples show n-type carrier behavior, with carrier concentrations in the 10^{18} cm^{-3} range, about 2 orders of magnitude lower than the F-doped samples. The mobility is very low, in the range of 1 cm^2/V·s for the pure SnO_2 film. We have previously found (Chapter IV) that mobility increase upon fluorine doping of tin oxide is consistent with an increased (002) texture in the film, as shown by XRD. However, the mobility of the undoped sample with 2% Zr addition is over 14 times greater than the undoped sample with no Zr additiona. This dramatic difference is not consistent with improved crystallinity, as ZrO_2 addition decreases texture and crystallinity.

Table 6.1. Comparison of the affect of ZrO_2 addition on the measured properties for SnO_2 films.

Sample ID	**%Zr in SnO_2**	**%Zr in SnO_2:F**	**Dep. Temp. (°C)**	**Thickness (nm)**	**Mobility ($cm^2/V{\cdot}s$)**	**n_e (10^{20} cm^{-3})**
L080923A-1		0	500	270	13.1-14.7	1.8
ZL080924-3-2		10	500	420	20.5	1.5
ZL081014-3-10		***0***	***525***	***390***	***27***	***4.1***
ZL081016-3-2		***2***	***525***	***410***	***36***	***3.7***
ZL090512-1-2		***10***	***525***	***485***	***23.2***	***1.7***
L080707-1	0		525	500	~1	0.03
L100314A-1	2		525	440	14.3	0.02

The Hall data for a large set of samples is compiled in Figure 6.1. In this set of experiments, all films are degenerately doped by fluorine addition. The $CBrF_3/O_2$ flow ratio is varied systematically from ~ 0.22 to 2.0, and the data are plotted such that each group corresponds to a percentage level of Zr with varying fluorine precursor flow. The data are compared in terms of the percentage of Zr with respect to Sn (cation %). Films containing Zr have lower carrier concentration than the highest achieved for FTO without Zr. However, the general trend is that mobility is always higher, and the highest mobility is observed for the 1-3 at% Zr levels.

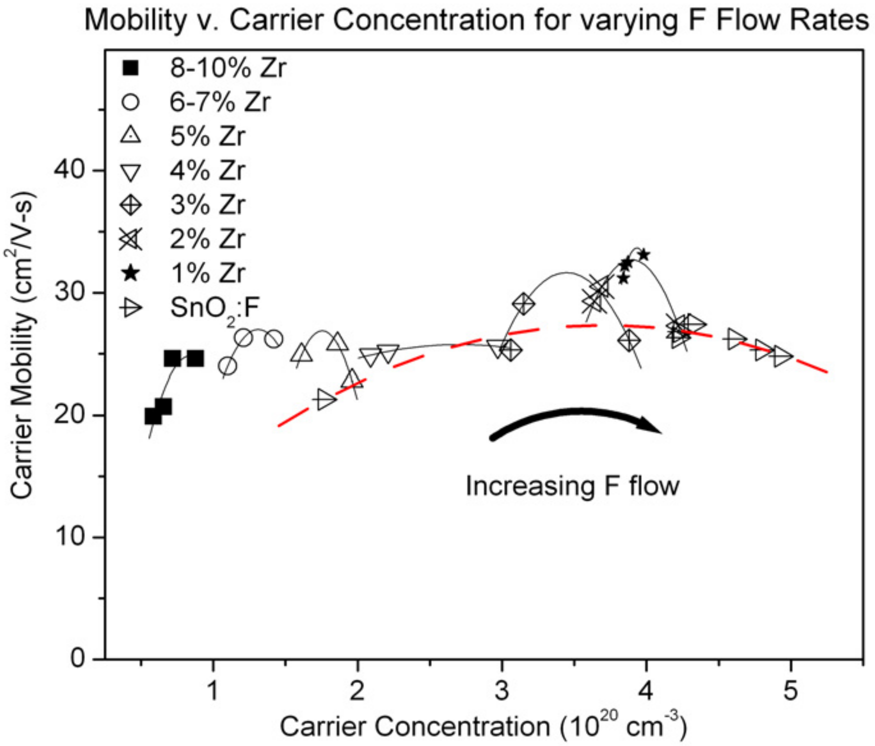

Figure 6.1. Mobility v. carrier concentration is plotted for a large compilation of samples with varying zirconia content. The F:O_2 flow rate is varied in the range 0.22-2.0, and in all cases the carrier concentration increases with fluorine flow. The solid lines are to aid the eye in seeing the trends for various Zr concentrations in FTO for various $CBrF_3$ flow rates. The dashed red line is the curve through data for FTO without Zr. The trend is that mobility is enhanced upon Zr addition and highest for 1 at% Zr in FTO. Further, the mobility remains high over a much broader range of carrier concentrations, especially at high F flow.

Discussion

The addition of Zr^{4+} (in the form of ZrO_2) should not positively influence the electronic properties of SnO_2 (Sn^{4+}) since the charge difference, ΔZ, between cations is zero. Additionally, since ZrO_2 ($\varepsilon_r \sim 25$) has a higher permittivity than SnO_2 ($\varepsilon_r \sim 10$), this experiment enables us to determine the influence of permittivity on the electronic properties of these films. From (6.3), it is evident that

$$\mu \propto \varepsilon_r^2 \tag{6.4}$$

indicating that notable increases in mobility may be evident for even small changes in the permittivity. Using ellipsometry data, it was shown in Chapter V that the real part of the permittivity, ε_1, increases with zirconia addition. Therefore, one can conclude that the increase in mobility in the films in the current study may be due to an increase in permittivity as predicted by Equation (6.3).

To further appreciate how permittivity changes influence the electronic properties of a material, we can draw comparisons to chemical criteria used to describe similar oxide systems. The complex permittivity is proportional to the polarizing power which is given by

$$\tilde{\varepsilon} \propto \tilde{P} = \frac{Z}{r^2} \tag{6.5}$$

where Z and r are the valence state and ionic radius, respectively, of the ion [9]. Zhang has formulated the following relationship for an ion's "Lewis acid strength," L,

$$L = \frac{Z}{r^2} - 7.7\chi_Z + 0.8 \tag{6.6}$$

where χ_z is the electronegativity for the impurity ion [10]. Notice that the first term is the polarizability, which is related to permittivity as given in (6.5). Wen *et al* have reported experiments into indium oxide-based ceramics in which cations (Sn, Ge, Si, Ti, Zr, Cu) of different Lewis acid strengths were incorporated [11, 12]. They report the trend of higher mobility for materials doped with cations of higher Lewis acid strength. That is,

$$\mu \propto L \tag{6.7}$$

where L is calculated from (6.6). A recent publication by Nakao *et al* demonstrated high mobility (~80 cm^2/Vs) for (pseudo-epitaxial) Ta-doped SnO_2 films formed by PLD using a TiO_2 seed layer approach [13]. The highest mobility and lowest resistivity are reported for 1% and 2% Ta doping, respectively. Taking the current study together with [13], the “Lewis acid strength” argument may explain the seemingly anomalous occurrence of high mobility. Ta_2O_5 is also a high permittivity oxide, with relative permittivity values ranging from 25-40. Recall the permittivity for ZrO_2 is typically in the range of 20-25. In general, high permittivity materials have higher Lewis acid strength, though this has not been mentioned specifically in the literature [14, 15]. Relevant data are compiled in Table 6.2, and the Lewis acid strength is computed according to [10]. The Lewis acid strength is slightly higher for Ta^{5+} versus Zr^{4+}. From the results in [13], 1-2 at.% Ta (in the form of Ta_2O_5) was added to SnO_2, and they report much improved carrier mobility values. It follows then that the films containing cations with higher Lewis acid strength and whose oxides exhibit even higher permittivity than ZrO_2, that the mobility would increase. We do contend however, that this comparison is compounded by the fact that the addition of Ta^{5+} is the source of donors in their films, while in the present study, the addition of F^- is the donor source.

.

Table 6.2. The ionic radii, polarizing power and Lewis acid strength.

Ion	**Ionic Radius (Å)**	**Z/r^2**	**Lewis acid strength**
Ta^{5+}	0.64	12.2	2.5
Zr^{4+}	0.71	7.93	2.2
Sn^{4+}	0.69	8.40	0.23

Wen *et al* have reported that the “ideal” cation addition is one that has low electronegativity and ionic radius, the latter of which is associated with a high nuclear charge, Z [11]. The high Z and low r are directly analogous to an oxide with high relative permittivity, as given by (6.5). Doping or alloying with such a material having high polarizing power can serve to screen the charge of the valence band (which has O-2p structure) because it can more strongly polarize the electron cloud [12]. This charge screening effect then weakens the strength of scattering centers. Note that this argument qualitatively agrees with the calculation for mobility when limited by ionized impurity scattering as given by (6.3).

Conclusion

It was found that the carrier mobility increases when ZrO_2, a high permittivity material, is added to SnO_2 and F-doped SnO_2 thin films. By varying the fluorine-to-oxygen flow rate during the chemical vapor deposition, it is found that mobility is higher for films containing up to ~ 1-10 at.% Zr compared to those without zirconia. The results are explained in the context of the increased permittivity. Our results are consistent with other author's arguments of a "high Lewis acid strength" of the zirconia additive into ITO-based ceramics, in which the polarizing power of ZrO_2 effectively screens charge associated with scattering centers, which serve to limit mobility.

Recalling our previous results in Chapter IV, it is found that mobility in FTO increases and is consistent with an increase in texture and crystallinity. However, films with ZrO_2, even with as-high or higher mobility, do not have as strong a texture as the films without ZrO_2. Hence, the high mobility cannot be attributed to texture or crystal quality. This implies that with addition of ZrO_2 into SnO_2, the structural effects are not as strong as the "permittivity" effects with regard to carrier mobility.

References

1. Minami, T. and T. Miyata, *Present Status and Future Prospects for Development of Non- or Reduced-Indium Transparent Conducting Oxide Thin Films.* Thin Solid Films, 2008. **517**(4): p. 1474-1477.

2. Chopra, K.L., P.D. Paulson, and V. Dutta, *Thin-Film Solar Cells: An Overview.* Progress in Photovoltaics, 2004. **12**(2-3): p. 69-92.

3. Chopra, K.L., S. Major, and D.K. Pandya, *Transparent Conductors - A Status Review*, Thin Solid Films, 1983. **102**(1).

4. Coutts, T.J., D.L. Young, and X. Li, *Characterization of Transparent Conducting Oxides.* MRS Bulletin, 2000. **25**.

5. Conwell, E. and W.F. Weisskoff, *Theory of Impurity Scattering in Semiconductors*, Physical Review, 1950. **77**: p. 388.

6. Gessert, T.A., Y. Yoshida, C.C. Fesenmaier, and T.J. Coutts, *Sputtered* In_2O_3 *and ITO Thin Films Containing Zirconium.* Journal of Applied Physics, 2009. **105**(8): p. 6.

7. van der Pauw, L.J., *A Method of Measuring Specific Resistivity and Hall Effect of Discs of Arbitrary Shape.* Philips Research Reports, 1958. **13**: p. 1–9.

8. Moulder, J.F., W.F. Stickle, P.E. Sobol, and K.D. Bomben, *PHI Handbook of Photoelectron Spectroscopy*. 1992: Perkin-Elmer Corp.

9. Ashcroft, N.W. and N.D. Mermin, *Solid State Physics*. 1976: Thomson Learning, Inc.

10. Zhang, Y., *Electronegativities of Elements in Valence States and Their Applications*, Inorganic Chemistry, 1982. **21**: p. 3889.

11. Wen, S.J., G. Campet, J. Portier, G. Couturier, and J.B. Goodenough, *Correlations Between the Electronic Properties of Doped Indium Oxide Ceramics and the Nature of the Doping Element*, Materials Science and Engineering, 1992. **B14**: p. 115.

12. Wen, S.J. and G. Campet, *The Textural Effect of Cu Doping and the Electronic Effect of Ti, Zr, and Ge Dopings upon the Physical Properties of Sn-Doped Indium Oxide*, Active and Passive Electronic Components, 1993. **15**: p. 79.

13. Nakao, S., N. Yamada, T. Hitosugi, H. Yasushi, T. Shimada, and T. Hasegawa, *High Mobility Exceeding 80* cm^2/Vs *in Polycrystalline Ta-Doped* SnO_2 *Thin Films on Glass Using Anatase* TiO_2 *Seed Layers.* Applied Physics Express, 2010. **3**: p. 031102.

14. Delahoy, A.E. and S.Y. Guo, *Transparent and Semitransparent Conducting Film Deposition by Reactive-Environment, Hollow Cathode Sputtering.* Journal of Vacuum Science & Technology A, 2005. **23**(4): p. 1215-1220.

15. Campet, G., S.D. Han, S.J. Wen, J.P. Manaud, J. Portier, Y. Xu, and J. Salardenne, *The Electronic Effect of* Ti^{4+}, Zr^{4+} *and* Ge^{4+} *Dopings Upon the Physical-Properties of* In_2O_3 *and Sn-Doped* In_2O_3 *Ceramics - Application to New Highly-Transparent Conductive Electrodes.* Materials Science and Engineering B-Solid State Materials for Advanced Technology, 1993. **19**(3): p. 285-289.

CHAPTER VII

CONCLUSIONS AND FUTURE OUTLOOK

The current study has contributed to the understanding of transparent conducting oxides in the following ways. The results demonstrate that alloying SnO_2 with a high permittivity oxide, ZrO_2, whose cation (Zr^{4+}) is isovalent to the host TCO cation (Sn^{4+}) extends the optical transmittance bandwidth, especially in the near infrared. Importantly, we have demonstrated that such an increase occurs for TCO films with identical electrical properties and physical thickness. Such films have similar electron (charge carrier) concentrations and carrier mobility, as determined by Hall measurements.

This demonstration may be considered a *proof of concept* of the main hypothesis of this study: increasing permittivity of a TCO material extends the plasma wavelength further into the NIR. The result is that transmittance is improved in both the NIR and visible wavelength regions. Further, when applied to PV devices, the implications are improved *Jsc*, important for device technologies which absorb in the NIR. This may be especially important for tandem cells, which incorporate stacks of absorber layers with different bandgaps in order to extend the bandwidth for collection of solar energy.

Significant attention has been given to optical characterization of the tin oxide-based TCOs in this study. Spectroscopic ellipsometry has been used in conjunction with spectrophotometry and Hall measurements to analyze in depth the effect of dopant and alloy concentration on the optoelectronic properties of this TCO material. The SE model has been shown to accurately and reproducibly extract thickness and surface roughness values, both of which have been corroborated by separate, physical measurements (profilometry and AFM, respectively). Further, the SE data have indicated that the incorporation of ZrO_2 into the SnO_2 host TCO increases the permittivity of the host TCO. In addition, when compared to Hall measurements, extraction of the optical mobility from SE data has elucidated the dominant carrier scattering mechanisms. It was found that for FTO (no Zr addition), the scattering is a combination of ionized impurities and scattering within the grains. For ~ 1-5 at.% Zr addition the ionized impurity scattering is dominant.

Considering these results, and assuming validation of our hypothesis, we apply this knowledge to some studies which were published concurrently with this study (CdO:Ti, SnO_2:Ta, IO/ITO:Zr) [1-5]. While the idea of increasing permittivity in TCOs has gone unreported, we assess that this concept is valid in light of work by other authors, in which addition of materials with high permittivity (though not reported as such) have improved the optical or electronic properties. Further Campet et al have explained the increase in mobility (and decrease in absorptance) for their doped IO and ITO ceramics using Zhang's Lewis acid strength [6]. Surprisingly, though their findings should be considered significant, Campet's work has not been highly cited nor much attention paid to the plausibility of the Lewis acid strength concept, especially with regard to TCOs. We have shown that permittivity and Lewis acid strength are qualitatively similar constructs of a material property for transition metal cations. The confinement to transition metals is of importance in that these tend to have lower values of electronegativy, which Zhang has mentioned as being important for high L values. Further these cations who have high polarizing power (high Z/r^2) and low electronegativity induce two effects: there is little or no overlap of the *d* conduction band of the host and that of the dopant; the high permittivity has the additional benefit of screening the scattering centers of the *O-2p* valence band, which has the effect of increasing the scattering time, τ, or equivalently the electron mobility.

Recent work on Ti-doped CdO, Ta-doped SnO_2 and Zr-doped ITO and IO have demonstrated either improved optical properties, far superior carrier mobility or both, when compared to the host TCO material or the TCO doped with conventional materials. As has been discussed in depth, ZrO_2 is a high permittivity material with kappa ~ 20-25. TiO_2 and Ta_2O_3 are also considered high-κ oxides with values in the range of 30-80 and 25-30, respectively. While the authors of the former two works make no mention of permittivity or Lewis acid strength, we may reconcile their results in light of the hypothesis demonstrated in the current work as well as by Gessert [5].

The key results are the demonstration of the benefits of high permittivity additions on both the optical and electrical properties. This is achieved with an aliovalent dopant, which has not been reported. The same thing could perhaps be demonstrated by adding, for instance, scandium or yttrium to indium oxide. In adddition, such additions to ZnO could be made which would have the effect of increasing permittivity as well as donor concentration. The idea is similar to that of using Ta as both a dopant and as a material that would increase permittivity, such that both carrier concentration and mobility could be increased. We have also considered the extremely high permittivity of the rare earth oxides as potential dopant candidates. Such ideas may serve to guide future research for advanced TCOs.

References

1. Nakao, S., N. Yamada, T. Hitosugi, H. Yasushi, T. Shimada, and T. Hasegawa, *High Mobility Exceeding 80 cm*^{2}*/Vs in Polycrystalline Ta-Doped* SnO_2 *Thin Films on Glass Using Anatase* TiO_2 *Seed Layers.* Applied Physics Express, 2010. **3**: p. 031102.

2. Zhang, B., X.P. Dong, X.F. Xu, P. Zhao, and J.S. Wu, *Characteristics of Zirconium-Doped Indium Tin Oxide Thin Films Deposited by Magnetron Sputtering.* Solar Energy Materials and Solar Cells, 2008. **92**(10): p. 1224-1229.

3. Saha, B., R. Thapa, and K.K. Chattopadhyay, *Bandgap Widening in Highly Conducting CdO Thin Film by Ti Incorporation through Radio Frequency Magnetron Sputtering Technique.* Solid State Communications, 2008. **145**(1-2): p. 33-37.

4. Gessert, T.A. and T.J. Coutts, *Transparent Conducting Oxides and Production Thereof*, U.S. Patent, Editor. 2007, NREL: U.S.A.

5. Gessert, T.A., Y. Yoshida, C.C. Fesenmaier, and T.J. Coutts, *Sputtered* In_2O_3 *and ITO Thin Films Containing Zirconium.* Journal of Applied Physics, 2009. **105**(8): p. 6.

6. Campet, G., S.D. Han, S.J. Wen, J.P. Manaud, J. Portier, Y. Xu, and J. Salardenne, *The Electronic Effect of* Ti^{4+}, Zr^{4+} *and* Ge^{4+} *Dopings Upon the Physical-Properties of* In_2O_3 *and Sn-Doped* In_2O_3 *Ceramics - Application to New Highly-Transparent Conductive Electrodes.* Materials Science and Engineering B-Solid State Materials for Advanced Technology, 1993. **19**(3): p. 285-289.